Fall 2007

Ring current -atmosphere interactions model with stormtime magnetic field

Alexander Emilov Vapirev
University of New Hampshire, Durham

Recommended Citation

Vapirev, Alexander Emilov, "Ring current -atmosphere interactions model with stormtime magnetic field" (2007). *Doctoral Dissertations*. 406.
https://scholars.unh.edu/dissertation/406

RING CURRENT - ATMOSPHERE INTERACTIONS MODEL WITH STORMTIME MAGNETIC FIELD

BY

ALEXANDER EMILOV VAPIREV

M.S., Sofia University, Sofia, Bulgaria, 1999

DISSERTATION

Submitted to the University of New Hampshire
in partial fulfillment of
the requirements for the degree of

Doctor of Philosophy

in

Physics

September 2007

This dissertation has been examined and approved.

V. Jordan

Dissertation Director, Vania K. Jordanova, Adjunct Research Associate Professor of Physics

Roy B. Torbert

Roy Torbert, Professor of Physics

Joachim Raeder, Associate Professor of Physics

Lynn Kistler

Lynn Kistler, Associate Professor of Physics

Jochen Heisenberg

Jochen Heisenberg, Professor of Physics

7/30/2007

Date

DEDICATION

To my parents

"An expert is a man who has made all the mistakes

which can be made in a very narrow field."

- Niels Bohr

ACKNOWLEDGMENTS

I thank my academic adviser Prof. Vania Jordanova for giving me the opportunity to work with her. I thank her for her guidance throughout my research and studies. It has been a privilege to work with her.

I thank the members of my dissertation committee for their time and patience and their useful suggestions and helpful comments.

I want to thank all my teachers and colleagues from the Bulgarian Academy of Sciences and the University of Sofia and especially those at the department of Nuclear Energy and Nuclear Technologies and the department of Quantum Electronics and Laser Technologies.

I want to thank the academic program coordinators Katie Makem and Kathy Giberson for their help on so many occasions.

I want to thank all my colleagues at UNH and especially Douglas Larson, Burçin Dönmez and Georgi Nenchev for all the help and conversations. I also want to thank Sorin Zaharia (LANL) and Yoshizumi Miyoshi (Nagoya University) for the useful discussions and support on numerous occasions.

I want to express my sincere gratitude to Nikolay Tsyganenko (GSFC) and Reiner Friedel (LANL) for their help.

I thank my parents, my brother, my sister and all my friends for their love and support through all these years.

CONTENTS

LIST OF TABLES

LIST OF FIGURES

ABSTRACT

RING CURRENT - ATMOSPHERE INTERACTIONS MODEL WITH STORMTIME MAGNETIC FIELD

by

ALEXANDER EMILOV VAPIREV
University of New Hampshire, September, 2007

An improved version of the ring current-atmosphere interactions kinetic model (RAM) is presented in this thesis. The recent stormtime empirical model T04s and the IGRF model are used to represent the Earth's external and internal magnetic fields respectively. Particle drifts, losses due to charge exchange with geocoronal hydrogen and atmospheric losses are included in the model as they are considered the main mechanisms of ring current development and its following decay. A numerical technique for bounce-averaging along the field lines is introduced and results for the calculated bounce-averaged hydrogen densities and magnetic gradient-curvature drift velocities (general case) for the moderate storm of April 21-25, 2001, are presented. A comparison in the calculations between T04s and a dipole field shows that the bounce-averaged hydrogen density for T04s differs with $\sim$ 5% from that for a dipole field for quiet time and it may become 30% smaller for disturbed conditions on the nightside for $L > 4$. The gradient-curvature velocities for T04s at large L-shells are $\sim$ 20% higher on the nightside and 20% lower on the dayside than those for a dipole field for quiet time. For disturbed conditions they are respectively $\sim$ 200% higher and 20% lower than the dipole values. The contribution of the cross-B term to the magnetic drift is $\sim$ 5%. Results for the time evolution of the trapped equatorial flux for H^+, He^+, and O^+ ions for various particle energies and pitch angles obtained by the new model with a non-dipole field (RAM-ND) are presented. The new computations for the April 2001 storm using a Volland-Stern convection model show a slight continued increase in the flux and the total ring current energy for the three ion species even after the storm main phase. A higher increase in the flux is observed towards the dusk side for the RAM-ND model compared to RAM due the difference in the charge exchange rates and the azimuthal drifts for the two different geomagnetic field configurations. Both models give similar values for the low energy ion fluxes. The high energy component of the ion flux for large pitch angles for RAM-ND has more strongly expressed dominance during the storm recovery phase. The increase in the O^+ flux after the storm minimum Dst given by RAM-ND, indicates a continuous several hour activity of the various ionospheric sources during stormtime, leading to the accumulation of energetic O^+. The contribution of He^+ to the total ring current is about 4%. The total ring current energy using RAM-ND is reduced by $\sim 30\%$ compared to RAM. The results obtained by the RAM-ND model confirm recent calculations by other models and they are consistent with previous satellite measurements. The energy spectra of the calculated spin averaged ion flux is compared with Polar/CAMMICE-MICS data few hours before the Dst minimum. The flux profile dependence on the L-shell value is studied at the midnight-dusk and at the prenoon side. Both RAM-ND and RAM fluxes predict the measurements beyond 3 R_E reasonably well with the RAM-ND model performing slightly better than RAM in the mid-energy range. At lower L-shells the measured low energy flux does not have a well expressed minimum, while the modeled fluxes for both models have deep and broad minima. The dip in the modeled flux profiles at all L-shells is shifted towards higher energies compared to the dip in the data. The minima shift for RAM-ND is smaller than the minima shift for RAM in most of the cases. An approximate calculation of the perturbation in the Dst due to the change in the total stormtime ring current energy content is presented. The depression in the Dst for RAM-ND is about two times smaller than the change predicted by RAM due to the smaller total energy for RAM-ND.

CHAPTER 1

INTRODUCTION

Conditions on the sun, in the solar wind and Earth's space environment often can influence the performance and reliability of spacecrafts and ground-based systems. This is referred to as Space Weather (Figure 1-1, after Lanzerotti [2003]). Magnetic storms, a major part of space weather, develop when the coupling of the solar wind to the magnetosphere becomes strong and prolonged and the geomagnetic activity becomes intense. The thresholds and driving parameters, namely the duration ΔT of the main phase of the event, the southward Interplanetary Magnetic Field (IMF) B_z component, and the stormtime index *Dst*, could then be as follows [Gonzalez et al., 1994]:

Storm strength	*Dst* [nT]	B_z [nT]	ΔT [h]
Great	$<$ -100	$<$ -10	$>$ 3
Intense	-100	-10	3
Moderate	-50	-5	2
Small (typical substorm)	-30	-3	1

Table 1.1: Storm classification according to the duration ΔT of the main phase of the event, the southward Interplanetary Magnetic Field (IMF) B_z component, and the stormtime index *Dst*.

The largest storms are often related to Coronal Mass Ejections (CME) from the Sun [e.g., Gosling et al., 1991]. In these cases, the related enhancements of solar wind velocity accompanied by southward IMF direction result into interplanetary shocks (IPS) (see Figure 1-2).

The enhancement of the ring current is an essential element of all geomagnetic storms.

It consists [e.g., Frank, 1967] of geomagnetically trapped 10-200 keV ions (mainly H^+, He^+, and O^+) and electrons that drift azimuthally around the Earth at radial distances of about $2-7$ R_E (Earth radii), overlapping the radiation belt region. The drift is a combined curvature and gradient drift which is eastward for electrons and westward for ions, i.e., the direction of the current is westward (Figure 1-3).

According to the classical substorm injection hypothesis, the ring current is enhanced via energization and injections of plasma sheet particles from the tail towards the inner magnetosphere during substorms, which are typical for storm times. Depending on the solar wind driving, the plasma sheet can become superdense (up to 10 cm^{-3}) [Borovsky et al., 1997], heated (temperatures of >10 keV in the near Earth region, rather than $5-8$ keV), and enriched in ionospheric ions [Young et al., 1982; Moore and Delcourt, 1995; Fu et al., 2001]. The energy density in the plasma sheet, in general, is higher during magnetic storms than quiet times [e.g., Nose et al., 2001], but it is also highly variable, modulating the relative geoeffectiveness of comparable southward IMF intervals even within a single magnetic storm [Jordanova et al., 1998, 2003a; Liemohn et al., 2001a; Kozyra et al., 2002]. Unusual populations are sometimes seen, such as plasma with characteristics resembling low latitude boundary layer (LLBL) plasma moving along open drift paths into the inner magnetosphere near midnight [Kozyra et al., 1998]. The storm time enhancement of the plasma sheet ion population contributes significantly to the ring current buildup [Jordanova et al., 1998].

Since ions in the energy range 10-200 keV are responsible for the majority of the ring current energy content (and thus *Dst* variation), most of the ring current forms through convective transport from the inner plasma sheet. A strong correlation between geosynchronous plasma sheet density at midnight and minimum *Dst* [Jordanova et al., 1998, 2003a; Thomsen et al., 1998] supports this viewpoint. Further, Nose et al. [2001] infer that the plasma sheet is the dominant source for the ring current based on the similarity in composition of the inner plasma sheet and outer ring current regions.

The convection within the magnetosphere is driven by interaction with the solar wind. During periods of southward interplanetary magnetic field (IMF), reconnection on the dayside sweeps magnetic flux to the magnetotail, creating a pressure gradient that drives plasma back toward the sun (Figure 1-4). This convection strength has been correlated to the solar wind motional electric field (E_y) and the electric potential difference across the high latitude ionosphere [e.g., Reiff et al., 1981]. Several studies have correlated E_y with the decrease in Dst^* [Burton et al., 1975; Akasofu, 1981], and later OBrien and McPherron [2000] demonstrated that additional correlation exists between E_y and Dst^* recovery. This is consistent with the fact that ion outflow through the dayside magnetopause has been shown by kinetic ring current models [Takahashi et al., 1990; Ebihara and Ejiri, 1998; Liemohn et al., 1999; Jordanova et al., 2003a] to be a major ring current loss process during the main phase of intense magnetic storms. The time scale for ion loss due to these drifts is proportional to the convection electric field and thus to the interplanetary dawn-to-dusk electric field.

Jordanova et al. [1998] showed that the most important loss process due to collisions is charge exchange with exospheric hydrogen, resulting in high energy neutral atoms (ENA) and low energy protons. Their conclusions agree with Monte Carlo simulations of a great geomagnetic storm by Noël [1997]. A direct measurement confirming the difference in character between globally-averaged main and recovery phase ring current losses during a major magnetic storm was provided using ENA observations by the Polar spacecraft [Jorgensen et al., 2001]. The globally averaged loss rates during the late recovery phase were consistent with charge exchange as the loss mechanism; however, during the main phase, these losses (through ENA observations) were well in excess of charge exchange losses.

Given a relatively long main phase, plasma sheet ions moving on open drift paths into the inner magnetosphere are not captured on closed drift paths but move through to the dayside magnetopause and are lost. During such events, the ring current is highly asymmetric [e.g., Takahashi et al., 1990; Jordanova et al., 1999] with up to 90% of the energy flowing along open drift paths in the main phase [Liemohn et al., 2001a; Kozyra et al., 2002]. In situ measurements are consistent with this asymmetry [e.g., Frank, 1970; de Michelis et al., 1997a; Grafe, 1999]. One of the first great acheivements of energetic neutral atom (ENA) imaging was the experimental confirmation of this asymmetry [Roelof, 1987; Henderson et al., 1997; Pollock et al., 2001; Mitchell et al., 2001; Reeves and Spence, 2001]. In fact, the images in Mitchell et al. [2001] capture the conversion of open to closed drift paths (asymmetric to symmetric ring current) during a step-like transition to northward IMF B_z in the main phase of a large magnetic storm. Energetic (tens of keV) O^+ has been observed in front of the bow shock (seen out to $200R_E$ upstream) during storm events [Christon et al., 2000; Posner et al., 2002], indicating that the ring current is flowing out the dayside magnetopause at these times. The upper atmosphere also provides evidence for a partial ring current during storms, with [Craven et al., 1982] showing that stable auroral red (SAR) arcs are primarily limited to the dusk-to-midnight sector. In their review of SAR arcs, Kozyra et al. [1997] concluded that the Coulomb interaction between the thermal electrons and the ring current is responsible for the magnetospheric heat flux that produces SAR arcs. Numerical simulations, [Jordanova et al., 1999; Liemohn et al., 2000] showed that the local time asymmetry of the partial ring current matches the SAR arc observations.

The objective of this thesis is to model the behaviour of the ring current with the existing global ring current-atmosphere interactions model (RAM) [Jordanova et al., 1997, 2003a] coupled with a non-dipole magnetospheric field model. The first version of the RAM code uses a magnetic dipole to represent the Earth's magnetospheric field. Although the RAM model has been quite successful in modeling the ring current environment for a variety of geomagnetic storms, approximating of the Earth's field with a magnetic dipole could yeald inaccurate results for the behaviour of the ring current during large storms. For large geomagnetic disturbances, the field lines are strongly deformed and significantly differ from a magnetic dipole. In the present study we use the recent storm-time T04s empirical magnetic field formulation, which describes well the magnetospheric configuration for both quiet and disturbed conditions [Tsyganenko, 2002a,b; Tsyganenko et al., 2003; Tsyganenko and Sitnov, 2005].

The physical processes involved in the development and the decay of the ring current are described in Chapter 2. In Chapter 3 we describe the theoretical approach of the kinetic model (RAM) developed by Jordanova [1995] and the changes which have been made in order to incorporate a non-dipole geomagnetic field model into it, considering losses only due to charge exchange. The details of the numerical techniques are discussed in Chapter 4. The time evolution of the ring current H^+, He^+ and O^+ distribution functions for moderate and large geomagnetic storms, are presented in Chapter 5. A summary of the results obtained with the present version of the RAM model updated for non-dipole magnetic field (RAM-ND) and suggestions for future work are given in Chapter 6.

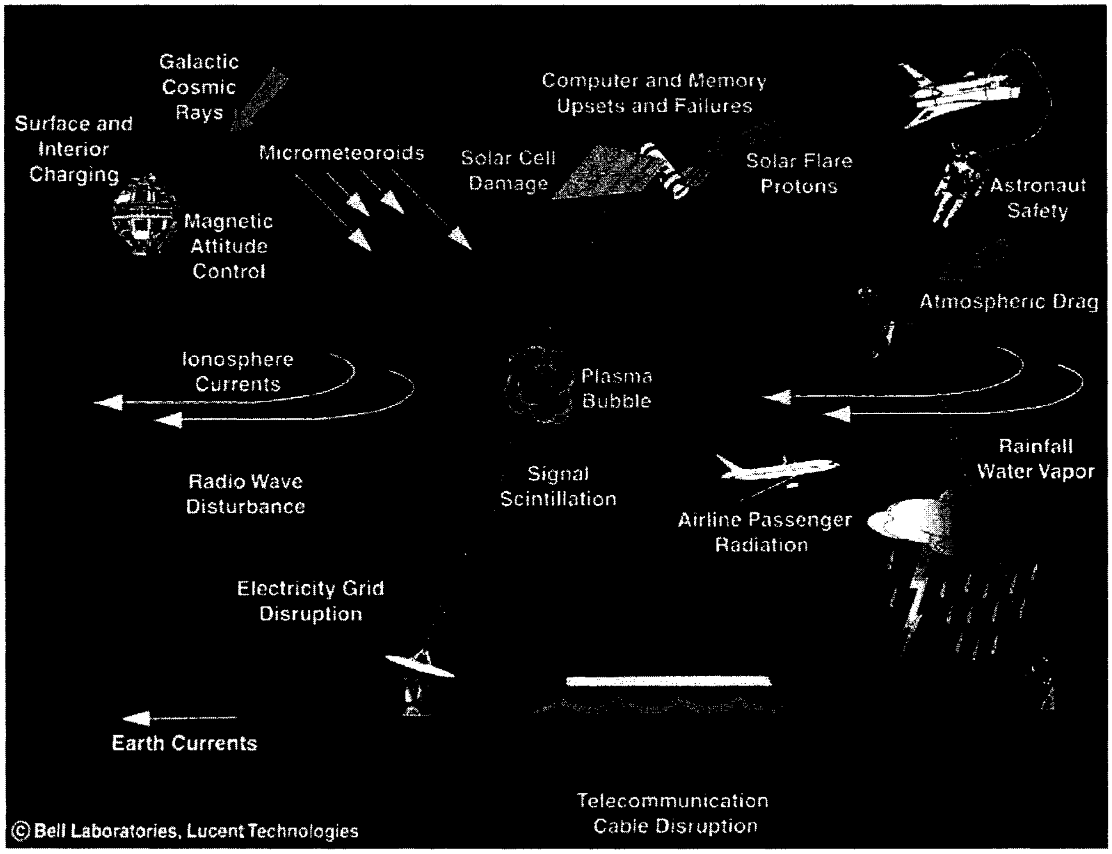

© Bell Laboratories, Lucent Technologies

Figure 1-1: Schematic representation of the impact of Earth's magnetosphere and atmosphere on telecommunication and navigation systems and electrical power grids.

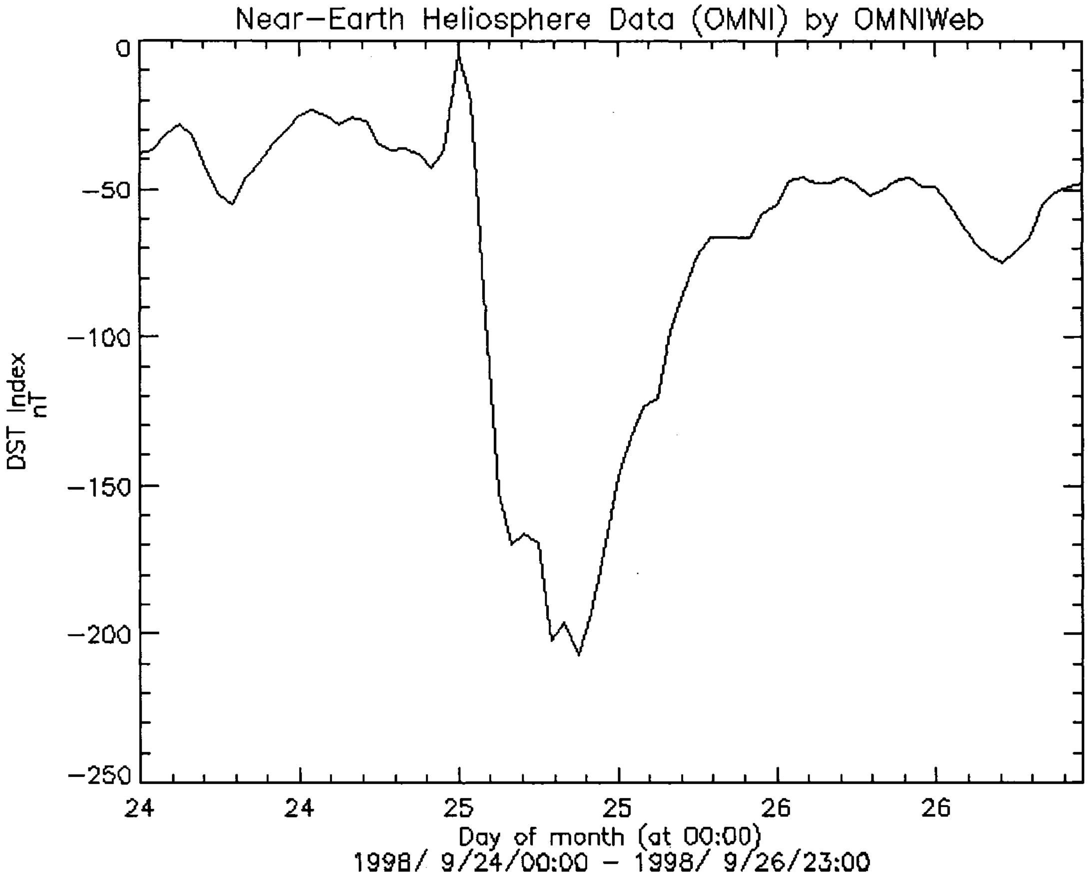

Figure 1-2: *Dst* index for the geomagnetic storm of 24-26 September, 1998. The sudden storm commencement peak is right before the main phase of the storm.

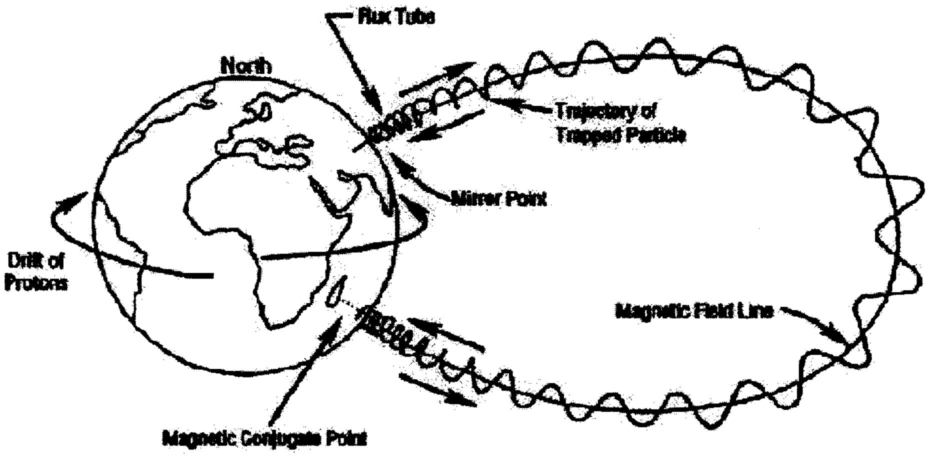

Figure 1-3: Trapped particles

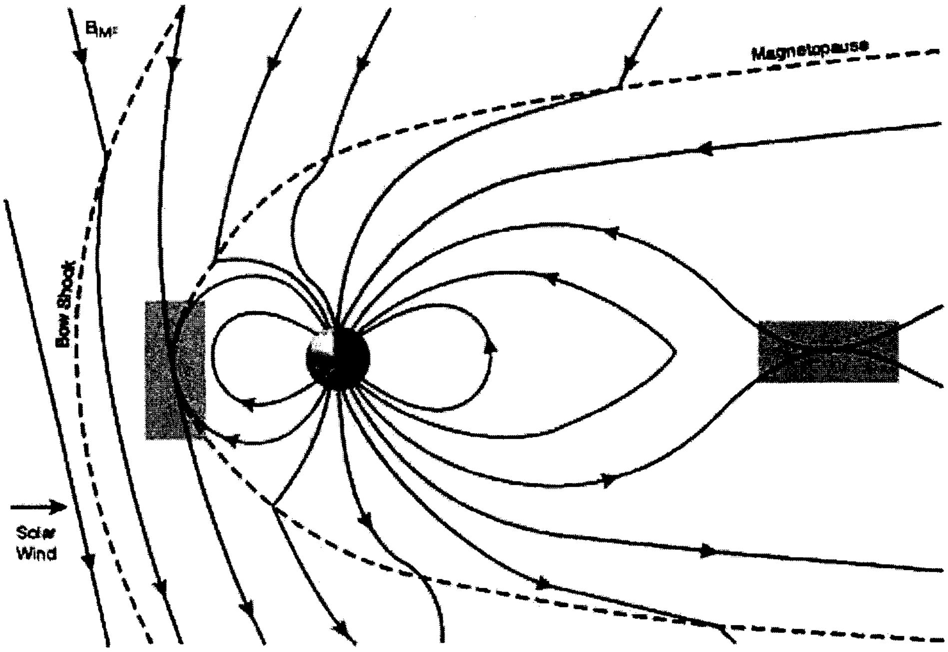

Figure 1-4: Southward IMF reconnecting on the dayside with the Earth's magnetic field.

CHAPTER 2

ORIGIN AND DEVELOPMENT OF THE TERRESTRIAL RING CURRENT

2.1 General Structure of the Ring Current

The basic idea about the structure and the shape of the ring current is that of a toroidal-shaped inhomogeneous electric current that flows westward around the Earth at geocentric distances between ~ 2 R$_E$ and ~ 9 R$_E$ (Figure 2-1). The ring current consist of geomagnetically trapped charged particles, gyrating around the magnetic field lines because of the Lorentz force and also experiencing drift motions due to the gradient and curvature of the magnetic field [e.g., Roederer, 1970]. The collective motion is an azimuthal drift for the trapped particles: electrons move eastward and most ions (with energies above a relatively low threshold [e.g., de Michelis and Orsini, 1997b] move westward. This charge transport results in a ring current. Figure (2-2) shows the basic motions of charged particles in the presence of a magnetic field: the gradient drift motion, the curvature drift motion and the gyration [e.g., Roederer, 1970].

The elementary currents j_∇, j_C, j_G resulting from these motions can be expressed in terms of the particle pressure components, namely $P_\perp$ and $P_\parallel$, perpendicular and parallel to the magnetic field [Parker, 1957]. The current due to particle drift driven by the magnetic field gradient is:

$$\mathbf{j}_\nabla = P_\perp \frac{\mathbf{B} \times \nabla B}{B^3} \tag{2.1}$$

The current due to particle drift driven by the magnetic field curvature is given as:

$$\mathbf{j}_C = \frac{P_\parallel}{B^4} \mathbf{B} \times (\mathbf{B} \cdot \nabla)\mathbf{B} \tag{2.2}$$

and the current due to gyro-motion within the particle distribution is:

$$\mathbf{j}_G = \frac{\mathbf{B}}{B^2} \times \left[\nabla P_\perp - \frac{P_\perp}{B} \nabla B - \frac{P_\perp}{B^2} (\mathbf{B} \cdot \nabla)\mathbf{B} \right] \tag{2.3}$$

The three terms on the right side of Equation (2.3) represent currents due to the particle pressure gradient, the magnetic field gradient, and the magnetic field line curvature, respectively. The drift and gyration terms driven by the magnetic field gradient are equal and opposite (Equations 2.1 and 2.3), and thus the total current does not depend on gradients of the magnetic field:

$$\mathbf{j} = \mathbf{j}_\nabla + \mathbf{j}_C + \mathbf{j}_G = \frac{\mathbf{B}}{B^2} \times \left[\nabla P_\perp + \frac{P_\parallel - P_\perp}{B^2} (\mathbf{B} \cdot \nabla)\mathbf{B} \right] \tag{2.4}$$

In the case of an isotropic distribution ($P_\parallel = P_\perp$), the magnetic field gradient plays no role in the current buildup and the total current depends only on the pressure gradient.

The quiet time ring current population is distributed over distances with the L parameter ranging from ~ 2 to ~ 9 and with an average current density of $\sim 1 - 4$ nA/m^2 [e.g., Lui and Hamilton, 1992; de Michelis and Orsini, 1997b]. The storm time ring current density increases over its whole radial extent and may exceed values of ~ 7 nA/m^2 [e.g., Lui et al., 1987].

Dessler and Parker [1959] and later Sckopke [1966] showed theoretically that the disturbance $\triangle B$ of the equatorial surface geomagnetic field during magnetic storms is proportional to the energy of the ring current particles (the Dressler-Parker-Sckopke relation):

$$\frac{\triangle B}{B_0} = \frac{2E}{3E_m} \tag{2.5}$$

Here $B_0 =\sim 30000$ nT is the average surface geomagnetic field intensity at the magnetic equator, E is the total energy of the ring current particles and $E_m = B_0^2 R_E^3/3 \backsimeq 10^{19}$ J, is the energy of the Earth's dipole field above the Earth's surface [Carovillano and Siscoe, 1973].

The generalized Dressler-Parker-Sckopke relation considers terms from internal and boundary sources:

$$\frac{B_D}{B_0} = \frac{2E + M - \oint \mathbf{R} \cdot \mathbf{n} d\sigma}{3E_m} \tag{2.6}$$

where B_D is the decrease in field due to the combined magnetic field from all sources and $M = \int B_D^2/2\mu_0 dv$ is a volume integral and represents the total magnetic energy inside the magnetosphere. The unit vector $\mathbf{n}$ is the normal pointing outward, and $\mathbf{R}$ is given as:

$$\mathbf{R} = \left(p + \frac{B^2}{2\mu_0}\right)\mathbf{r} + \rho(\mathbf{V} \cdot \mathbf{r})\mathbf{V} - \frac{(\mathbf{B} \cdot \mathbf{r})\mathbf{B}}{\mu_0} \tag{2.7}$$

Here p is the thermal pressure, $\mathbf{r}$ is the radius vector from the center of the Earth, ρ is the mass density of the solar wind in the plasma mantle, $\mathbf{V}$ is the flow velocity of the mantle plasma, and $\mathbf{B}$ is the total magnetic field vector. The pressure in (7) is assumed to be isotropic.

The general location and the main driving mechanisms of the ring current have been established through observations and theoretical work. The existence of the ring current was confirmed by spacecraft measurements and it was shown that this current system is a permanent element of the Earth's magnetosphere. Frank [1967] showed that the ring current is dominated by ions (mostly protons) with energies of ~50 keV. In the 1970s the development of better space mass-spectrometer instruments made it possible to distinguish between the different ion species [Shelley et al., 1972]. The detailed composition and energy of the ring current, however, were not clarified until the Active Magnetospheric Particle Tracer Explorer (AMPTE) mission of the late 1980s (Section 2.3.1).

2.2 Measurements

During the past few decades there have been numerous experimental ring current related studies based on ground and space measurements. Two of the most successful spacecraft missions, in regard to ring current measurements, were the AMPTE and CRRES satellites.

The Charge Composition Explorer (CCE), one of the three AMPTE spacecraft, carried on board the charge-energy-mass (CHEM) spectrometer. CHEM was an advanced composition spectrometer which was used to identify missing elemental and charge composition in the range of a few keV to a few hundred keV through a combination of measurement techniques [Gloeckler et al., 1985]. Statistical studies of the ion population in the inner magnetosphere [Daglis et al., 1993] and case studies [Krimigis et al., 1985; Hamilton et al., 1988] were used to resolve the relative contribution of the various ion species to the quiet time and storm time ring current.

Figure (2-3) [Daglis et al., 1993] shows the accumulated percentage of the ion energy density at geosynchronous orbit (the outer ring current) as a function of the ion energy. The data shown are for geomagnetically quiet times (left panel) and for geomagnetically disturbed times (right panel). The curves represent averaged data over two and a half years of measurements by the CHEM instrument onboard AMPTE/CCE. Plotted are curves for the total energy density as well as the energy density of the four main ring current ion species (H^+, O^+, He^{++}, He^+). An important fact is that the most part of the total measured ion energy density is within the energy range of about 10 keV to 100 keV. Also, the H^+ is the dominant ion species, while the contribution due to O^+ ions increases from about 6% to 21% during storm times. The data was averaged over all local times and over all types of events (i.e. storms and substorms) with auroral electrojet (AE) indices AE $<$ 30 nT (quiet times) and AE $>$ 700 nT (active times). This averaging smoothens out the very active events (i.e. intense storms). Previous studies indicated that about 5% of the current energy density resides at energies $>$ 300 keV [Williams, 1987].

The data from the CHEM instrument onboard the AMPTE/CCE mission, showed that during geomagnetically quiet times, the ring current is dominated by H^+ ions with a negligible contribution of some heavier ions. AMPTE operated during solar minimum and the February 1986 intense magnetic storm was the only one to be observed [Hamilton et al., 1988]. During this storm period the O^+ population increased and became the dominant ion species around the peak of the storm. Hamilton et al. [1988] estimated that the contribution of O^+ ions reached 47% of the total energy density for distances with $L = 3 - 5$ (the inner ring current), compared with 36% for the H^+. For $L = 5 - 7$ (the outer ring current), the peak of the O^+ contribution was found to be around 31%, and the contribution of H^+ ions was about 51% around the storm maximum.

The second spacecraft mission for conducting in situ ring current observations was the Combined Release and Radiation Effects Satellite (CRRES), which operated during 1990 – 1991, i.e., around solar maximum. CRRES caried on board the Magnetospheric Ion Composition Spectrometer (MICS) [Wilken et al., 1992] which was also capable of gathering information about the composition of the ring current ions in the energy range between a few tens of keV to a few hundred keV. The CRRES/MICS observations of a number of moderate and large geomagnetic storms showed that the ring current properties observed by CCE/CHEM during the February 1986 storm [Hamilton et al., 1988] are very similar.

Later Daglis [1997] showed that for larger storms (as given by the *Dst* index) the O^+ contribution to the ring current is bigger than the H^+ contribution. Also, Daglis [1997] showed that the magnitude of the *Dst* index and the O^+ contribution to the ring current increase concurrently. This feature was observed in all moderate to large storms during 1991, and it was also noticed in the February 1986 storm [Hamilton et al., 1988].

The time profiles of both O^+ andH^+ ion contribution to the total ring current energy density (L = 5-6) are shown in Figure (2-4) together with the corresponding *Dst* index for the storm period of June $4-5$, 1991 [Daglis et al., 1999b]. In Figure (2-4) one can see that the protons are the dominant species (about 80%) during the quiet prestorm period, and that the O^+ ions contributed only around 10% of the measured ion energy density. After the beginning of the storm, the O^+ contribution increased and stayed above 30% for more than 24 hours. Such levels of O^+ are considered to be exceptionally high [Daglis et al., 1993]. The localized and sporadic character of ionospheric outflow [e.g., Strangeway and Johnson, 1983] usually is considered to be the reason for the short-lived energetic O^+ enhancements [Daglis and Axford, 1996]. This fact combined with the relatively short charge exchange lifetime of energetic O^+ [Smith et al., 1981] would suggest that such a long-lived enhanced level of O^+ population indicates a continuous ionospheric feeding of the inner plasma sheet during the storm main phase.

During the great storm in March 1991, the population of the O^+ ions rose dramatically (Figure 2-5). The maximum of the main phase of the storm was clearly dominated by O^+, with a contribution of more than 65% of the total energy density for $L = 5-7$, and it exceeded 80% for $L = 5-6$ [Daglis et al., 1999a]. In an earlier study, Daglis [1997] noted the concurrent increase of the O^+ contribution and the decreasing *Dst* index. The storm had a sudden commencement at 03:41 UT on March 24, after which the O^+ contribution went from 10% up to 40%. At the same time the *Dst* index dropped to around -100 nT.

The *Dst* recovery period followed together with a decrease in the O^+ abundance. Both *Dst* and O^+ reached their peaks during the main phase of the storm. Hamilton et al. [1988] observed a similar pattern during the great storm of February 1986. Figure (2-5) again shows that for intense geomagnetic activity the O^+ contribution reaches very high levels ($> 40\%$) which last for an extended time period of more than 30 hours.

In 1991, CRRES also observed five medium to intense storms. For all of them the ionospheric contribution to the ring current energy density due to energetic O^+ ions was $20-65\%$. About 30% of H^+ ion population in the storm time outer ring originates from the ionosphere [Gloeckler and Hamilton, 1987]. This shows clearly that, although the energy source of storms is unambiguously of solar origin, the majority of the storm time ring current particles are of terrestrial origin. Therefore follows the conclusion that the major source of the ring current, during quiet times, is the solar wind through the plasma sheet region, while the storm time ring current becomes increasingly of terrestrial origin with the development of the geomagnetic activity. The O^+ causes the rapid final enhancement of the ring current at the storm maximum, which could be the cause of the second storm maximum during intense storms with a two-step development [Kamide et al., 1998a]. Noël [1997] suggests that the O^+ also induces an equally rapid initial decay of the ring current, which could possibly be the reason for the two-step recovery of intense storms. The last two points are further discussed in Section 3.3.

To summarize, the solar wind and the terrestrial ionosphere are the main sources of ring current particles. The ring current is dominated by protons during geomagnetically quiet times (Table 2.1). The other substantial contribution to the ring current comes only from the O^+ ion population, which increases with the intensifying of the geomagnetic activity. Eventually the O^+ becomes dominant during intense storms [Daglis, 1997]. Typical values of the contribution of the O^+ to the ring current energy density are around 6% during quiet times and can exceed 50% for great storms. Most of the ring current O^+ ions originate in the high-latitude ionosphere of the Earth, while the origin of the ring current H^+ could be from multiple sources. Gloeckler and Hamilton [1987] concluded that around 35% of protons in the outer ring current, and 75% of protons in the inner ring current are of ionospheric origin during quiet times. For the storm time ring current, Gloeckler and Hamilton [1987] estimated that the corresponding ratio is about 30% to about 65%. Solar wind He^{++} ions is estimated to contribute less than 4% of the ring current during small to medium storms (Table 2.1).

2.3 Sources of Ring Current Particles

All trapped particles in the inner magnetosphere contribute to the ring current. The most substantial contribution to the density of the current is however only due to ions with energies ranging from about 10 keV to a few hundreds of keV [Williams, 1987]. Electrons contribute little to the ring current because of their negligible energy density [Baumjohann, 1993]. The magnetospheric plasma sheet and the terrestrial ionosphere are the biggest sources of ring current particles. The particle population in the plasma sheet is supplied by the ionosphere and the solar wind which defines the solar wind and the terrestrial ionosphere as the main sources of ring current particles.

The ionosphere and the solar wind are both sources of magnetospheric H^+ ions and this makes it difficult to determine the dominant source. The magnetospheric O^+ on the other hand mostly originates in the ionosphere. Charge exchange processes (Section 2.5) in the inner magnetosphere make the matter even more complicated because through these processes oxygen ions with higher charge state (of solar wind origin) are being transformed into lower charge state oxygen (typical for the ionosphere), and solar wind He^{++} is being transformed into He^+ (which is provided also by the ionosphere). However, only a negligible percentage of magnetospheric O^+ ions originates through charge exchange from solar wind oxygen ions with high charge states (O^{6+}) and therefore O^+ ions are considered signature ions of ionospheric outflow associated with magnetosphere-ionosphere coupling.

The initial energy of ionospheric ions is of the order of several eV to several tens of eV, which is low compared with the higher initial energy of solar wind ions (order of several keV). Shelley et al. [1972] using the data from the first mass-spectrometer (satellite 1971-089A on polar orbit) discovered energetic heavy ions with mass-to-charge ratio M/q=16. These were thought to be O^+ ions originating in the Earth's ionosphere. Later, a new generation of ion composition instruments made it possible to obtain additional information about ion charge state [Gloeckler and Hsieh, 1979]. Observations by the missions GEOS 1 and 2, Prognoz 7, and SCATHA confirmed the existence of O^+ in the magnetosphere, and the significant contribution of the ionospheric source during magnetic storms [Balsiger et al., 1980; Kaye et al., 1981]. O^+ ions are abundant in the ionosphere but they are not found in the solar wind and that is why they have since been used as an evidence and as a measure of the contribution of the ionosphere to the magnetospheric ion population.

The plasmasphere has also been discussed to be a direct source of ring current ions [Balsiger et al., 1980] based on the high O^{++}/O^+ and high He^+/He^{++} ratios in the range of a few keV, which are not observed in either the solar wind or the ionosphere. However, since O^{++} and He^+ are found only in small numbers in the ring current, the plasmasphere is considered to be a minor source (compared to the ionosphere and the solar wind).

Williams [1983] estimated that around 90% of the ring current is contained within the $15 - 250$ keV energy range (with peak around $50 - 100$ keV) and he also estimated that the average energy of the ring current is about several tens of keV. The estimates were confirmed later by the AMPTE mission [Williams, 1987], which was the first mission to adequately measure the composition of the main part of the ring current.

Table (2.1) [Daglis et al., 1999b] summarizes the ion composition data for three different geomagnetic conditions: quiet time, small-to-medium storms and intense storm. The data is based on composition measurements by the AMPTE/CCE and the CRRES missions [Gloeckler and Hamilton, 1987; Hamilton et al., 1988; Daglis et al., 1993; Daglis, 1997]. The values are calculated using observations at L $\approx$ 5, which is near the maximum of the ring current density [Lui et al., 1987; de Michelis and Orsini, 1997b].

Ion Source and Species	**Quiet Time**	**Small-Medium Storms**	**Intense Storms**
Total energy density, keV cm^{-3}	$\sim$10	$\geq$15	$\geq$100
Solar wind H^+ , %	$\geq$60	$\sim$50	$\leq$20
Ionospheric H^+ , %	$\geq$30	$\sim$20	$\leq$10
Ionospheric O^+ , %	$\leq$5	$\sim$30	$\geq$60
Solar wind He^{++} , %	$\sim$2	$\leq$5	$\geq$10
Solar wind He^+ , %	<1	<1	<1
Ionospheric He^+ , %	<1	<1	<1
Solar wind, total, %	$\sim$65	$\sim$50	$\sim$30
Ionosphere, total, %	$\sim$35	$\sim$50	$\sim$70

Table 2.1: Sources of ring current Ions, according to composition measurements by the AMPTE and CRRES missions: Contribution of main ion species to total ion energy density at L $\approx$ 5 (after Daglis et al., 1999b).

2.3.1 The Solar Wind

The solar wind provides a flow of $\sim 10^{29}$ ions/sec incident on the magnetosphere. About $0.1 - 1.0\%$ of the incident particles penetrate into the magnetosphere wich results in an effective solar wind source strength of about $10^{26} - 10^{27}$ ions/sec. Using measurements from the Geotail mission Nishida [1994] confirmed the importance of the solar wind source for energetic ions in the magnetotail region, especially for distances greater than 30 R_E [Christon et al., 1996]. Terasawa et al. [1997] using measurements from the Wind and Geotail spacecraft showed that for extended periods of northward interplanetary magnetic field (geomagnetically quiet times) the magnetotail at distances larger than 15 R_E is dominated by solar wind particles entering through the side regions of the magnetosphere. Christon et al. [1994] showed that the solar wind source strength increases toward higher altitudes using the radial profiles of ion charge states in the near-Earth plasma sheet.

It is still not well understood how and where exactly the solar wind particles enter the magnetosphere, despite of our knowledge about the general structure of the solar wind source geometry and some successful models [e.g., Pilipp and Morfill, 1978]. The transport and acceleration processes acting on these particles, before they reach the inner magnetosphere and contribute to the ring current, are also not well described. Evidence for the complexity of the particle transport in the megnetosphere is the fact that ions with ionospheric and solar wind origin have been observed up to distances of about 210 R_E on the nightside [Hirahara et al., 1996].

Speiser [1965a,b] was the first to consider the acceleration of ions from the magnetotail toward the inner magnetosphere. He showed the effects of the $\mathbf{E} \times \mathbf{B}$ drift of the ions through the magnetotail when the neutral sheet is given as a region with a small and finite normal component B_n of the magnetic field. Speiser showed that charged particles are accelerated and that some of them are ejected from the neutral sheet along the magnetic field lines. Some more recent studies [e.g., Ashour-Abdalla et al., 1993; Øieroset et al., 2000; Li et al., 2005] used comprehensive data analysis and modeling to study the particle sources using the nonlinear aspects of particle trajectories in the magnetotail region.

2.3.2 The Ionosphere

The contribution of the ionosphere as a source of magnetospheric particles is of about the same order of magnitude as the solar wind source [Moore and Delcourt, 1995]. The ionospheric outflow consist of different particle species [e.g., Horwitz, 1982]. The two most important ionospheric outflow regions are the dayside cleft and the auroral region. The high-altitude polar ion flow is considered a significant source of oxygen ions [e.g., Horwitz et al., 1992]. The midlatitude ionosphere can also be a significant source of thermal oxygen during magnetic storms [Yeh and Foster, 1990].

A number of observational studies have indicated the importance of both the auroral acceleration region and cleft ion fountain as magnetospheric ion sources [Hultqvist et al., 1988; Lu et al., 1992]. Different models have estimated the transport and energization processes of ionospheric ions from the cleft region [e.g., Cladis and Francis, 1992] as well as from the auroral region [e.g., Shapiro et al., 1995]. Comprehensive statistical works have established the extent of ion outflow from each region [Yau et al., 1985]. Daglis and Axford [1996] concluded that the different regions of the ionosphere would dominate the ion outflow for different magnetospheric conditions and/or different levels of the solar windmagnetosphere coupling. Since both major ionospheric ion species O^+ and H^+ experience charge exchange with the exospheric neutral hydrogen [e.g., Orsini et al., 1994], the ionospheric outflow at high altitudes is the reason for an intense flux of neutral O and H in the high-latitude magnetosphere [Moore, 1984]. Therefore global neutral atom imaging could be used for resolving the ion source issue at high latitudes [Hesse et al., 1993].

Since the ionospheric ions have relatively low energies (around 1 eV), it is thought that a variety of successive acceleration mechanisms act on the ionospheric ions to raise the particle energy up to tens of keV. Upward accelerated ions from the ionosphere in the auroral regions (ion beams and conics with energies of $0.1 - 10$ keV) were detected through satellite observations [e.g., Peterson et al., 1988]. Thelin et al. [1990] used the data obtained by the Swedish satellite Viking to discuss the transverse and parallel ion acceleration both in the auroral regions and in the cleft region. There are several examples from the Viking data showing elevated ion conics with accelerations up to the 40 keV upper limit of the ion spectrometer [Lundin and Eliasson, 1991]. The existence of very localized regions of intense lower hybrid waves (100 – 300 mV/m) and transversely accelerated ions with energies 10 – 100 eV (sufficient for ejection into the magnetosphere), were detected by rocket experiments [Kintner et al., 1992]. Observations at low altitudes by the Swedish-German satellite Freja confirmed the relationship of the transverse energization of ionospheric ions with large depletion holes in the ionosphere [Lundin et al., 1994]. Strangeway et al. [2005] used FAST satellite data, restricted to dayside magnetic local times, to determine the controlling parameters for ionospheric outflows. They assumed two major ion outflow sources: the ion heating through dissipation of downward Poynting flux and the electron heating through soft electron precipitation. Strangeway et al. [2005] showed that a correlation exists between the ion outflows and the two considered processes at altitudes of about 4000 km, but they were not able to determine which process is dominant. Due of the strong correlation, both processes could be used to scale the ion outflows at different altitudes.

2.3.3 Compositional Changes

In general, the population of O^+ ions in the inner magnetosphere depletes relatively quickly [Daglis and Axford, 1996]. During geomagnetic storms, however, the various ionospheric sources are active for several hours and this results in an increase of the concentration of O^+ ions in the ring current during the main phase of the storm (*Dst* minimum). The compositional changes contributing to the O^+ population are substantial during all storms and become most prominent during intense storms [Daglis, 1997]. This intense ionospheric ion outflow into the magnetosphere is thought to be the cause of the rapid second enhancement of the ring current and the corresponding decrease in the *Dst* index, observed during the main phase of intense storms with a two-step development [Kamide et al., 1998a]. Also, the abundance of O^+ ions in the ring current leads to important differences from a proton loaded ring current regarding wave-particle interactions and decay through charge exchange.

Wave-particle interactions can also be a significant factor for the loss of ring current ions. Electromagnetic ion cyclotron (EMIC) waves can cause atmospheric losses due to rapid scattering during geomagnetic storms [Cornwall et al., 1970]. The propagation characteristics of EMIC waves and the resulting rates of ion population growth strongly depend on the relative ion abundance [Kozyra et al., 1984] at different phases of a storm. During great geomagnetic storms, it is possible that the concentration of the injected O^+ in the ring current may exceed the concentration of H^+ and the growth of EMIC waves may be limited to frequencies below the O^+ gyrofrequency [Thorne and Horne, 1997]. The modulation of EMIC instability by O^+ injection then should also change the fast loss process due to these waves for the ring current H^+ ions during the main phase of a storm.

The long-term decay rate of the ring current is also influenced by the growth of O^+ population, since the charge exchange lifetime of ring current O^+ is much shorter than the one of H^+ for energies $\geq$40 keV [Smith et al., 1981]. This implies that for an O^+ dominated ring current the initial decay rate will be higher. Such a fast initial ring current decay, due the large amount of O^+ during the main phase of the storm, has been observed in the storm of February 1986 [Hamilton et al., 1988] and in the four intense storms observed by CRRES in 1991 [Daglis, 1997]. A two-stage recovery of intense storms was reported in 1963 [Akasofu et al., 1963]. Akasofu et al. [1963] suggested the existence of two ring currents around the Earth, the one located closer to the Earth decaying faster. This is thought to account for the rapid initial decay of the ring current and a decrease of the decay rate with time during the recovery phase (*Dst* recovery) of intense storms. However, there are observations [Hamilton et al., 1988; Daglis, 1997] which strongly imply that the two-phase recovery of intense magnetic storms could be due to the presence of two ion components with distinctly different charge exchange lifetimes rather than to the existence of spatially separated multiple ring currents.

Smith et al. [1981] studied charge exchange losses in the ring current depending on energy and ion composition, comparing the charge exchange lifetimes of the main ring current ion species (H^+ and O^+). Most of the storm time ring current energy is contained in the range of 50-100 keV, and for these energies the O^+ charge exchange lifetime can be 10 times shorter than the one of H^+. This difference increases for higher energies. For example, at L=5 and a mirror latitude of 14°, the charge exchange lifetime of a 100 keV O^+ ion is ~46 hours; for the same energy the lifetime of H^+ ions is ~470 hours. These timescales become considerably shorter for smaller L (inner ring current) due to the increase of the density of the geocorona. At L=3.5 the corresponding 100 keV O^+ and H^+ charge exchange lifetimes are 11 and 110 hours. In the lower energy range, however, O^+ has a longer lifetime than H^+. At L=5 and energy 10 keV, O^+ and H^+ lifetimes are about 56 hours and 17 hours respectively, and at L=3.5 the corresponding lifetimes are 28 and 5.5 hours. Such a difference in the charge exchange lifetimes for an O^+ dominated ring current will result in a rapid initial decay just after the storm maximum due to the rapid loss of high-energy O^+. Also, this difference will lead to a lower decay rate during the recovery phase due to the relatively long lifetimes of low-energy O^+. This analysis implies how crucial the ion composition is for the dynamic evolution of the ring current. Variations in the relative concentration of the two main ion species H^+ and O^+ could define the decay rate of the storm time ring current [Tinsley and Akasofu, 1982] and is taken into account in the present comprehensive modeling study. Charge exchange processes, including charge exchange with He^+ and He^{++}, are discussed further in Section 2.5.

2.4 Ionospheric outflow

Substorms are the most common type of geomagnetic disturbance in the Earths magnetosphere. The ring current is formed primarily through injection and convection of plasma sheet particles from the tail towards the inner magnetosphere during geomagnetically active periods [e.g., Jordanova et al., 1998]. Injection of the particles is driven by strong duskward electric fields, while the convection within the magnetosphere is driven by interaction of the magnetosphere with the solar wind. There is still an open discussion regarding the processes which take part into the formation of the storm time ring current. It is not exactly clear whether the injection of particles results mainly from potential electric fields associated with periods of strong magnetospheric convection, or mainly from induction electric fields associated with the occurrence of magnetospheric substorms [Kamide et al., 1998b].

Kamide [1992] suggested that a magnetic storm develops as a result of a steady southward interplanetary magnetic field. Magnetic reconnection between the interplanetary magnetic field and the geomagnetic field [Dungey, 1961] is responsible for the energy transfer mechanism from the solar wind to the magnetosphere for both storms and substorms. Dungey [1961] suggested that if the IMF were antiparallel to the geomagnetic field at the dayside magnetopause, the two fields would merge together, namely the magnetospheric and the IMF lines should reconnect with each other which would result into a magnetic flux and energy transport from the dayside to the nightside magnetosphere. This means that reconnection will mostly happen when the IMF is southward, since the geomagnetic field goes northward. It has been confirmed that steady and prolonged southward IMF is a necessary condition for intense storms [Gonzalez et al., 1994], although here is still debate whether it is also a sufficient condition.

Ionospheric outflow, strongly associated with substorms is the major source of compositional ring current charges. Increase in the population of O^+ ions, the main signature of ionospheric outflow, have been observed by spacecraft in the inner magnetosphere during both growth and expansion phases of substorms [Strangeway and Johnson, 1983; Möbius et al., 1987; Daglis et al., 1996]. Observations by ground-based radars and polar-orbiting spacecraft in the upper ionosphere, confirmed the association of strong ionospheric outflow (mostly O^+ ions) with substorm expansion [e.g., Wahlund et al., 1992].

The magnetic field configuration becomes stretched on the night side during substorm growth phase and then it relaxes during the onset to a more dipole-like configuration [McPherron, 1972], due to disruption or reduction of the near-Earth cross-tail current [Kaufmann, 1987]. The dipolarization of the magnetic field is associated with strong induced electric fields [Moore et al., 1981]. Such electric fields effectively accelerate the ionospheric outflowing O^+ ions [Delcourt et al., 1991], but they are less efficient for the energization of H^+ ions [Fok et al., 1996]. The reason for the accelerated O^+ ions is related to the violation of the first adiabatic invariant and to its dependence on particle mass [Aggson and Heppner, 1977]. This assumption is supported by the energy spectra observed during substorms [Kistler et al., 1990].

The second and third adiabatic invariants for H^+ are violated due to the strong induced electric fields [Aggson and Heppner, 1977] observed in the inner magnetosphere, and which are responsible for the violation of all three adiabatic invariants for heavier ions. O^+ ions with initial energies of 100 eV can reach energies bigger than 100 keV, depending on the initial latitude, while H^+ ions with the same initial energies are limited to final energies of less than 20 keV [Delcourt et al., 1990]. The outflowing ionospheric O^+ ions then can reach very high energies and become the dominant ion species. This could happen during intense storms, which are always accompanied by frequent, intense substorms [Kamide, 1992] and thus large induced electric fields.

The ionospheric outflow of particles into the magnetosphere is most effective during a series of substorms [Daglis and Axford, 1996]. Intense ionospheric O^+ outflows, associated with successive intense substorms, which are always observed during large storms, may thus facilitate successive inward flow injection of ions. The result would be the trapping of more energetic ions, thus enhancing the ring current.

2.5 Charge Exchange Losses

The main collisional mechanism of ring current decay is charge exchange of the ring current ions with the geocorona [e.g., Jordanova et al., 1998]. The geocorona consists of relatively cold (~1000 K) neutral atoms (mostly hydrogen) which resonantly scatter solar Lyman radiation [Chamberlain, 1963]. The geocoronal density decreases quickly with the radial distance [Rairden et al., 1986], but at distances between 2 and 9 R_E collisions between ions and geocoronal hydrogen are frequent enough to account for significant losses of ring current ions.

The idea that charge exchange between H^+ and atmospheric hydrogen could effectively decrease the population of geomagnetically trapped energetic H^+ was proposed 40 years ago [Stuart, 1959]. This could lead to an effective decay of the ring current via charge exchange between energetic ring curren particles and exospheric hydrogen [Dessler and Parker, 1959]. Energetic ions may acquire an electron from the neutral hydrogen atoms and thus become neutralized.

2.5.1 Charge Exchange Processes

As mentioned before, the main loss mechanism of ring current ions through charge exhange is due to interactions with cold exospheric hydrogen. Since the geocorona is mostly a cold hydrogen gas, the most important charge exchange processes are:

$$H^+ + H \rightarrow H + H^+$$

$$O^+ + H \rightarrow O + H^+$$

$$He^{++} + H \rightarrow He^+ + H^+$$

$$He^+ + H \rightarrow He + H^+$$

Ions with small equatorial pitch angles reach relatively low altitudes and experience additional charge exchange processes with oxygen atoms in the upper atmosphere:

$$H^+ + O \rightarrow H + O^+$$

$$O^+ + O \rightarrow O + O^+$$

$$He^{++} + O \rightarrow He^+ + O^+$$

$$He^+ + O \rightarrow He + O^+$$

The charge exchange lifetime of energetic particles depends on the neutral hydrogen and oxygen densities, the charge exchange cross section for the different ion species and the equatorial pitch angle. The dependence of the neutral exospheric hydrogen density on the radial distance was calculated by Rairden et al. [1986]. He used observations of geocoronal emission of scattered solar Lyman alpha radiation from the ultraviolet photometer on Dynamics Explorer 1 over the time period 1981 – 1985. The data were fit to a spherically symmetric isothermal (1024 K) Chamberlain model [Chamberlain, 1963], in which the hydrogen density versus altitude is given as a function of the temperature.

Laboratory experiments have provided data about the cross sections for some of the charge exchange processes between ions and neutral [de Michelis and Orsini, 1997b], but cross sections of several geophysically interesting ions are still unknown [Spjeldvik and Fritz, 1978]. Charge exchange cross sections depend on the energy and the mass of the particles. That is why there are significant differences in the charge exchange lifetimes of the various ring current ion species [Smith et al., 1981]. Charge exchange lifetimes also strongly depend on the radial distance as the neutral hydrogen density falls off quickly with altitude [Rairden et al., 1986]. This is the reason for the faster decay of the inner part of the ring current. The mean charge exchange decay lifetime of any energetic ion in the equatorial plane with geocoronal hydrogen is:

$$\tau_e = 1/[n(r_0)\sigma v] \tag{2.8}$$

where $n(r_0)$ is the neutral hydrogen density in the equatorial plane, r_0 is distance from the Earth, σ is the charge exchange cross section of the ion species (energy and mass dependent), and v is the velocity of the ions [Smith and Bewtra, 1978].

Charge exchange losses are most important for H^+ and O^+ ions with energies of up to a few hundred keV [Sheldon and Hamilton, 1993]. The charge exchange cross sections become smaller at higher energies where wave-particle interactions are significant, especially for hot protons. Higher charge state ions (e.g., He^{++}, O^{++}) would experience multiple charge exchange with geocoronal atoms before they become neutral and escape the geomagnetic trapping region. Several recent ring current models have included the effects of charge exchange [e.g., Jordanova et al., 1994; Fok et al., 1995], considering all pitch angles (pitch angle particle distribution) and using a bounce-averaged kinetic equation, thus reducing the problem from three to two dimensions. Other ring current models [e.g., Kistler et al., 1989; Chen et al., 1994] were restricted only to equatorially mirroring particles.

2.5.2 Energetic Neutral Atoms

Charge exchange between singly charged energetic ions and the cold neutral hydrogen of the geocorona results in energetic neutral atoms (ENA) (Figure 2-6). An ENA is not bound by the magnetic field and after it is created, it leaves the place of origin along a straight trajectory with a velocity of the energetic ion. Therefore the geocorona provides the possibility of ENA remote imaging, which gives an additional information about the ion populations in the inner magnetosphere [Roelof, 1987].

The EPIC ion spectrometer, onboard the Geotail satellite, measured ENA at a distance of about 14 R_E on the dayside during the storm of October 29 – 30, 1994 [Lui et al., 1996]. The detected particles were considered to be ENA because the direction of the flux was not influenced by the magnetic field. The observations provided information about the evolution of ENA fluxes and their energy spectra of hydrogen, helium, and oxygen separately. ENA fluxes and the recovery rate of the *Dst* index were roughly steady, consistent with the estimated charge exchange losses for the storm time ring current. For energies higher than 200 keV, the intensity of energetic oxygen was the highest, consistent with the relatively short charge-exchange lifetime of energetic O^+. ENA images from the Polar spacecraft were presented for two storms in August and October 1996 [Henderson et al., 1997], showing the expected enhancement of ENA resulting from the particle buildup of the storm-time ring current. Low-altitude ENA measurements can provide information in addition to high-altitude observations, although the differentiation between ENA and energetic particles at those altitudes (above 500 km) could be problematic. One of the advantages of low-altitude ENA imaging is that the emissions are stronger because of the denser exosphere, and hence the higher charge exchange rates.

2.6 Coulomb Collisions

Ring current particles experience collisions with plasmaspheric particles. An energetic charged particle will interact with the electric field of a thermal ion or electron. Due to Debye shielding, there is an upper limit to the distance at which the particles interact. Such collisions result in energy transfer from the fast particle to the slow ion or electron, and in angular deflection of both particles. The angular scattering is important for electrons and low-energy ($<$ 10 eV) ions and is usually negligible for high-energy ions [Wentworth, 1963; Jordanova et al., 1996a].

Coulomb lifetimes for ring current ions were calculated by Fok et al. [1991] including heavy ions in both the ring current and the thermal plasma, the latter having a Maxwellian distribution. Fok et al. [1991] found that Coulomb decay lifetimes become comparable with the charge exchange lifetimes at low energies (tens of keV for ions). Their results suggested that ring current losses due to Coulomb collisions became important for the decay of the low-energy ion population, and might explain the discrepancy noted by Kistler et al. [1989] between modeled ring current distributions and the ring current fluxes measured by AMPTE/CCE during magnetically active conditions.

Coulomb collisions between ring current ions and thermal plasma result in heating of the thermal ions and electrons. The energy gained by the thermal particles at high altitudes, is transported along the magnetic field lines towards Earth, thus increasing the ion and electron temperatures in the upper ionosphere [Rees and Roble, 1975]. This results in increased plasma scale heights and minor ion density enhancements in the outer plasmasphere, which in turn results in the production of stable auroral red (SAR) arcs via relaxation of O^+ ions [e.g., Cole, 1965]. Further, Kozyra et al. [1987] studied SAR arcs focusing on the energy transfer between ring current ions and thermal plasma. They concluded that the energy transfer was highest when collisions occured between particles with equal velocities, and pointed out the possibility that O^+ has a dominant role of for energy transfer at low energies (about 10 to 100 keV).

Jordanova et al. [1996a] computed the total precipitating flux in particles/(cm^2s) at 1000km altitude, 1 hour and 12 hours from the beginning of the recovery phase of a moderate storm for three different ion species (H^+, He^+, and O^+), for three energy ranges: (a) $0.015 - 0.3$ keV; (b) $0.3 - 20$ keV; (c) $20 - 300$ keV (Figures 2-7 and 2-8 respectively). They found that the precipitation is enhanced in the early stages of the recovery phase (Figure 2-7) in the midnight region, due predominantly to convective drifts that move small pitch angle particles from high to low altitudes, where the are precipitated. Later in the storm recovery phase (Figure 2-8), the convection decreases and charge exchange and Coulomb drag losses remove a significant part of the low-energy proton and of the high-energy heavy ion populations. Thus, the high-energy part (> 10 keV) of the ring current at $L=2-4$ is dominated by protons and low-energy part (< 10 keV) is dominated by heavy ions. These results were in agreement with CHEM-AMPTE/CCE experiment [Gloeckler and Hamilton, 1987]. Jordanova et al. [1996a] concluded that Coulomb scattering significantly enhances the low-energy ion precipitating fluxes inside the plasmasphere.

2.7 Wave – Particle Interactions

The role of wave-particle interactions in the evolution of the ring current is still an unresolved problem. Pitch angle diffusion by plasma waves also contributes to ion loss in the ring current, especially during the main phase of a storm [e.g., Jordanova et al., 1996b, 2001a,b; Fok et al., 1996]. Intense plasma waves also provide an efficient process for energy transfer between different components of the plasma. Waves are particularly important as a heating mechanism for thermal heavy ions [e.g., Anderson and Fuselier, 1994; Horne and Thorne, 1997], and they can also transfer energy from ring current H^+ to O^+ during magnetic storms [Thorne and Horne, 1994, 1997].

The most widely studied interactions involve electromagnetic ion cyclotron (EMIC) waves. The scattering times of ions into the loss cone during resonant interactions with EMIC waves can be fast [Lyons and Thorne, 1972]. Typical ring decay times during the recovery phase are about 5 to 10 hours and are believed to result from charge exchange or Coulomb collisions. The ring decay timescales during the main phase of intense-to-great geomagnetic storms can reach values as low as $0.5 - 1.0$ hours, which is far too fast to be a result from charge exchange or Coulomb collision processes. That is why it is believed that additional loss mechanisms exist due to interactions of ring current ions with plasma waves.

Observations by the AMPTE/CCE spacecraft indicate that EMIC waves occur most frequently in the outer magnetosphere beyond 7 R_E and that the wave spectral properties depend on the magnetic local time [Anderson et al., 1992]. Events occurring between MLT 03 to 09 have an average occurrence frequency of $3-4\%$. They have essentially linear polarization at all latitudes and are generally confined to frequencies higher than the He^+ gyrofrequency. Typical normalized wave frequency may reach values up to $\sim 2.5-3.0$. Events between MLT 10 to 18 occur more often $(10-20\%)$ and the waves are generally distributed in two distinct frequency bands separated by a noticeable spectral gap near the He^+ gyrofrequency. The waves mostly have left polarization near the equator and linear polarization at higher latitudes. Anderson et al. [1992] suggested that plasma sheet ions, following open drift paths from nightside to dayside, develop sufficient temperature anisotropy and are the main cause of EMIC wave generation at $L>7$. A more recent study by Erlandson and Ukhorskiy [2001] addresses the occurrence of low-L $(3.5<L<5)$ EMIC waves during magnetic storms. Using about 10 years of data acquired by the Dynamic Explorer 1 (DE 1) satellite they show that EMIC waves in the equatorial magnetosphere occur 5 times more often during magnetic storms than during quiet times. The strongest waves (tens or hundreds of Hz) are observed at frequencies below the He^+ gyrofrequency.

During geomagnetic storms the energy sources for wave excitation (energetic protons with thermal anisotropy) are greatly enhanced, and the optimum region for EMIC wave growth occurs at lower L-shells along the duskside plasmapause [e.g., Jordanova et al., 1997]. Such waves can interact strongly with the ring current ion population. The H^+ ions, which are unstable to the amplification of ion cyclotron waves, are produced in the inner magnetosphere through betatron acceleration of ions moving along adiabatic drift paths [Cornwall et al., 1970]. The increased charge exchange rate for ring current ions with small pitch angles [Cornwall, 1977] increases the loss cone and thus increases the anisotropy of the drifting ion distributions making them even more unstable to the generation of plasma waves.

Jordanova et al. [1997] were the first to include the effects of waveparticle diffusion [Jordanova et al., 1996b] into a global simulation of ring current dynamics during a magnetic storm. The distribution function of energetic protons, obtained with the RAM code (which includes the effects of particle drifts, charge exchange and Coulomb scattering), was shown to be unstable to the generation of EMIC waves. Peak convective wave growth was confined to the dusk sector near the plasmapause. H^+ precipitation over the zone of significant wave growth was found to account for only $1-2\%$ of the total ring current energy for the time duration of this particular storm. Figure (2-9, after Jordanova et al. [1997]) shows the proton ring current characteristics as a function of radial distance in the equatorial plane and magnetic local time, 0.5, 3, and 6 hours after the beginning of the recovery phase of a moderate storm. The top panel shows the proton density (cm^{-3}), in the middle is the normalized parallel energy and at the bottom panel is the anisotropy of the energetic proton component. Figure (2-10, after Jordanova et al. [1997]) shows respectively plots of the wave gain Γ as a function of the radial distance and MLT for the same time intervals as in Figure (2-9): (top) in a proton ring current plasma; (middle) in a multi-component ring current plasma consisting of H^+, He^+, and O^+ ions with no wave-particle interactions included; (bottom) same as the middle panel but processes of wave-particle interactions are considered. The authors considered the wave growth of only He^+ wave branch below the helium gyrofrequency. Their study shows that in the accounted frequency interval, wave growth occurs only due to energetic (> 100 keV) protons. It was found that the frequency at which maximum wave growth is observed increases with time. The regions with wave gain $\Gamma > 1$ were located initially on the duskside (Figure 2-10a) between L=4 and L=5.5, and moved inward between L=3 and L=4 as time progressed (Figure 2-10b and 2-10c). The initial unstable region comprising values of $\Gamma > 1$ (Figure 2-10a), occurred for normalized frequency of 0.12, and coincided with the region of maximum normalized parallel energy

(Figure 2-9 middle panel). This finding confirmed the suggestion by Cornwall et al. [1970], that the main region of wave generation should be just inside the plasmapause due to the enchanced cold plasma density. In addition, Jordanova et al. [1997] found that both He^+ and O^+ ring current ion populations damp the waves from the He^+ wave branch (decreasing the magnitude of the wave amplification) and therefore multi-component plasma has to be considered to obtain realistic predictions of wave instability in the inner magnetosphere.

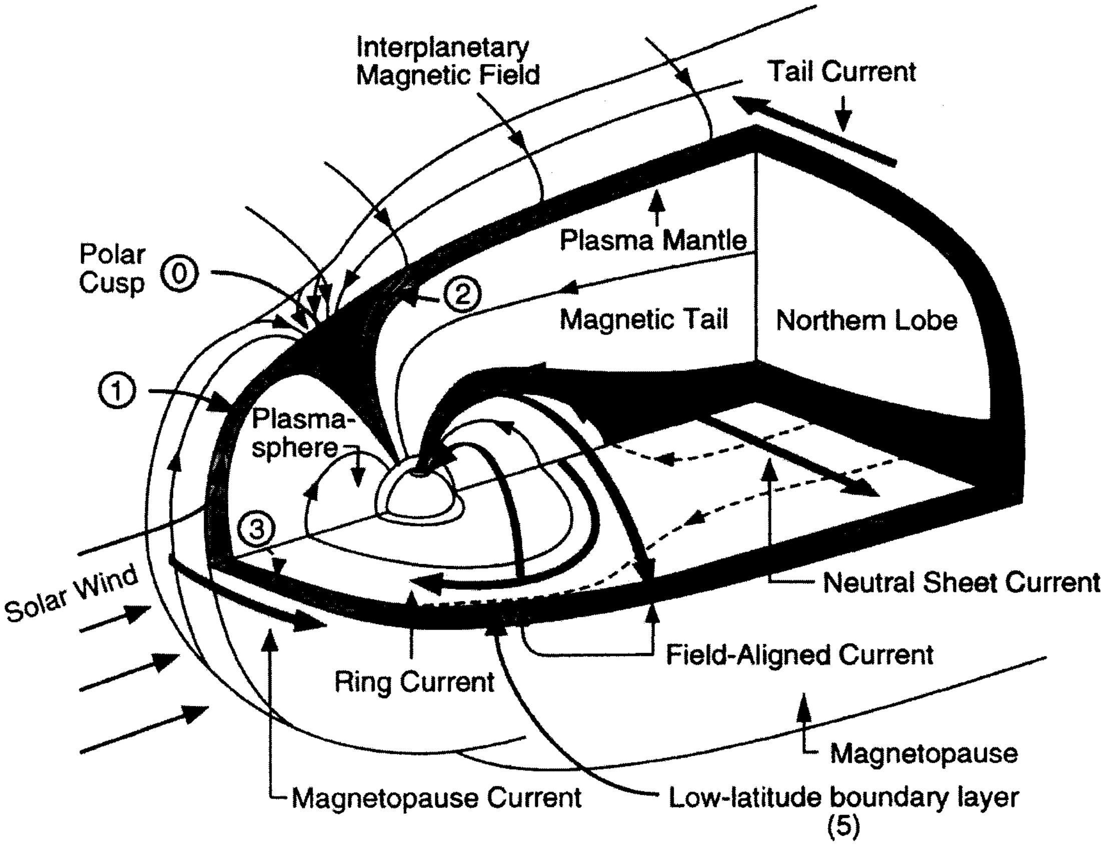

Figure 2-1: A schematic representation of the Earth's magentosphere. The ring current flows westward around the Earth at geocentric distances between ~ 2 R_E and ~ 9 R_E.

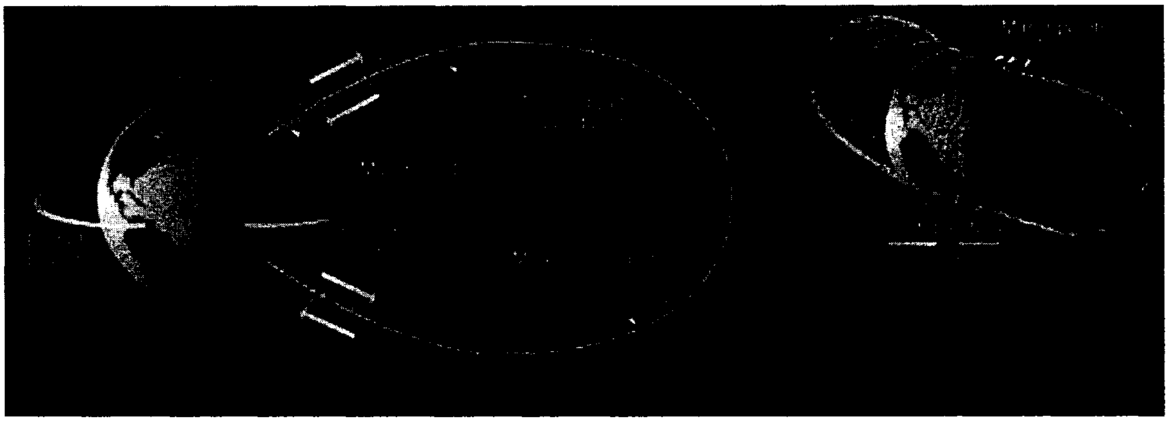

Figure 2-2: Schematic representation of the trapped particles in the Earth's magnetic field. The particles gyrate around magnetic field lines and move along the line until they reach the mirror points. The whole structure rotates and forms a toroidal shaped current.

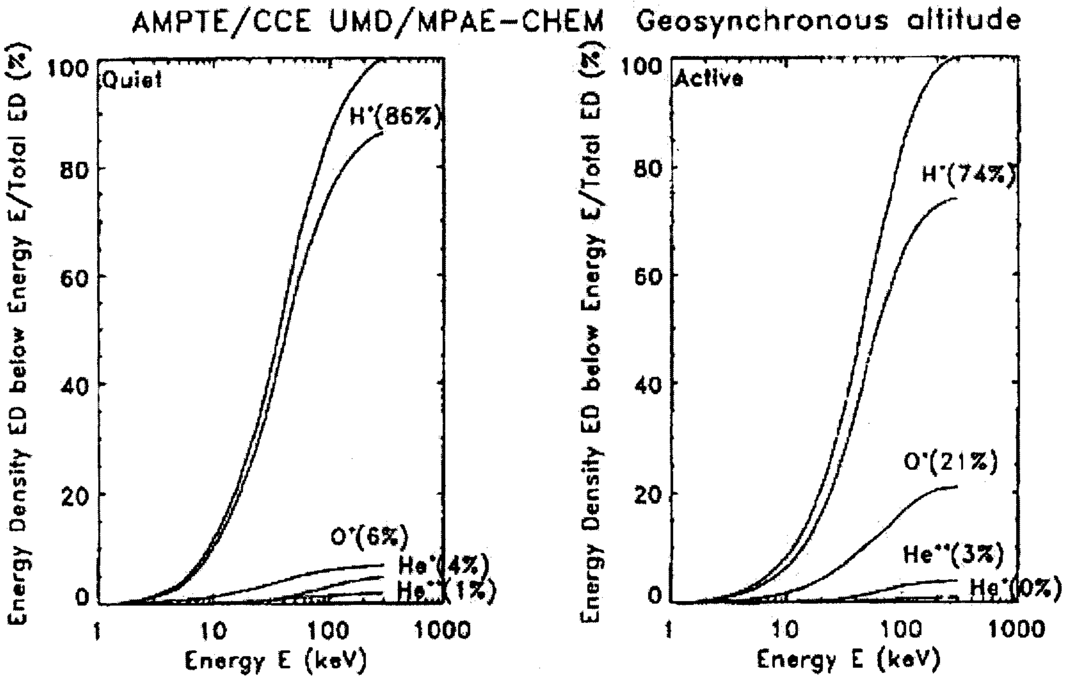

Figure 2-3: Accumulated percentage of the ion energy density at geosynchronous altitude (i.e., outer ring current) as a function of energy, (left) at geomagnetically quiet times and (right) at active times (after Daglis et al., 1993). Plotted are curves for the total energy density as well as for the energy density of the four main ion species H^+, O^+, He^{++}, and He^+.

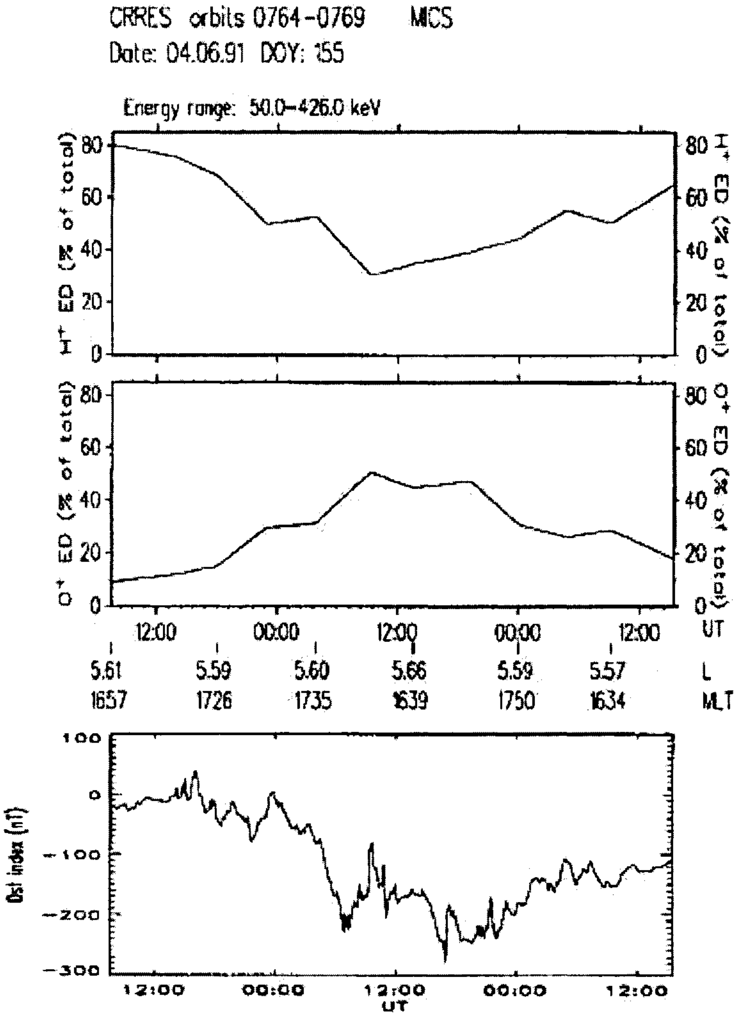

Figure 2-4: Time profiles of (top) the H^+ and O^+ contributions to the total ion energy density in the ring current at L = 5 − 6, and (bottom) the 5-min *Dst* index during the intense storm of June 5, 1991 (after Daglis et al., 1999b).

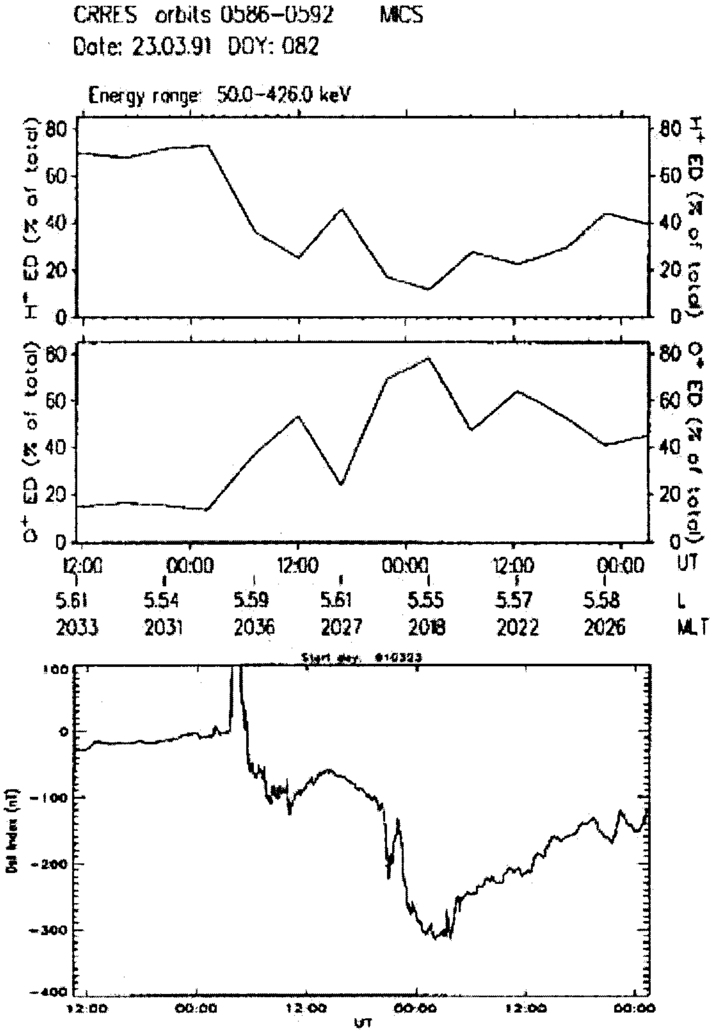

Figure 2-5: The great magnetic storm of March 24, 1991: time profiles of (top) the H^+ and O^+ contributions to the total ion energy density in the ring current region at L = 5 − 6 (as measured by CRRES/MICS), and (bottom) the 5-min *Dst* index. The main features to be observed are the dominance of O^+ during storm maximum and the concurrent decrease in the *Dst* and the increase of the O^+ contribution to the total ion energy density (after Daglis et al., 1999a).

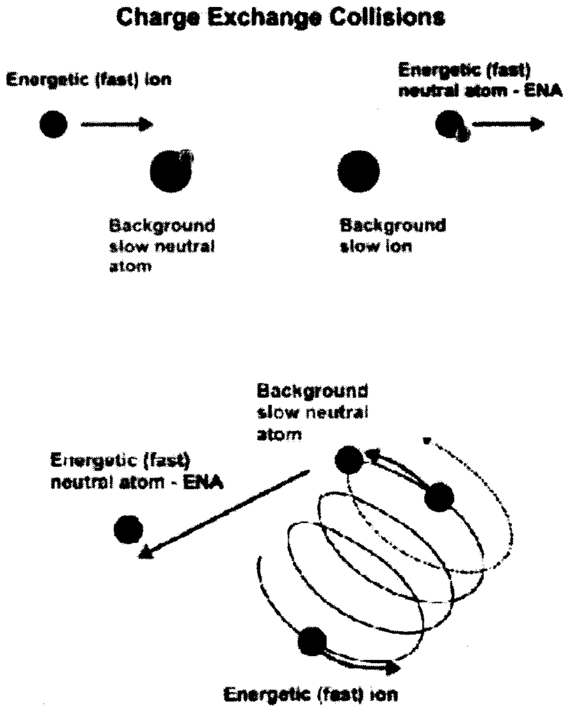

Figure 2-6: Schematic representation of the charge exchange processes.

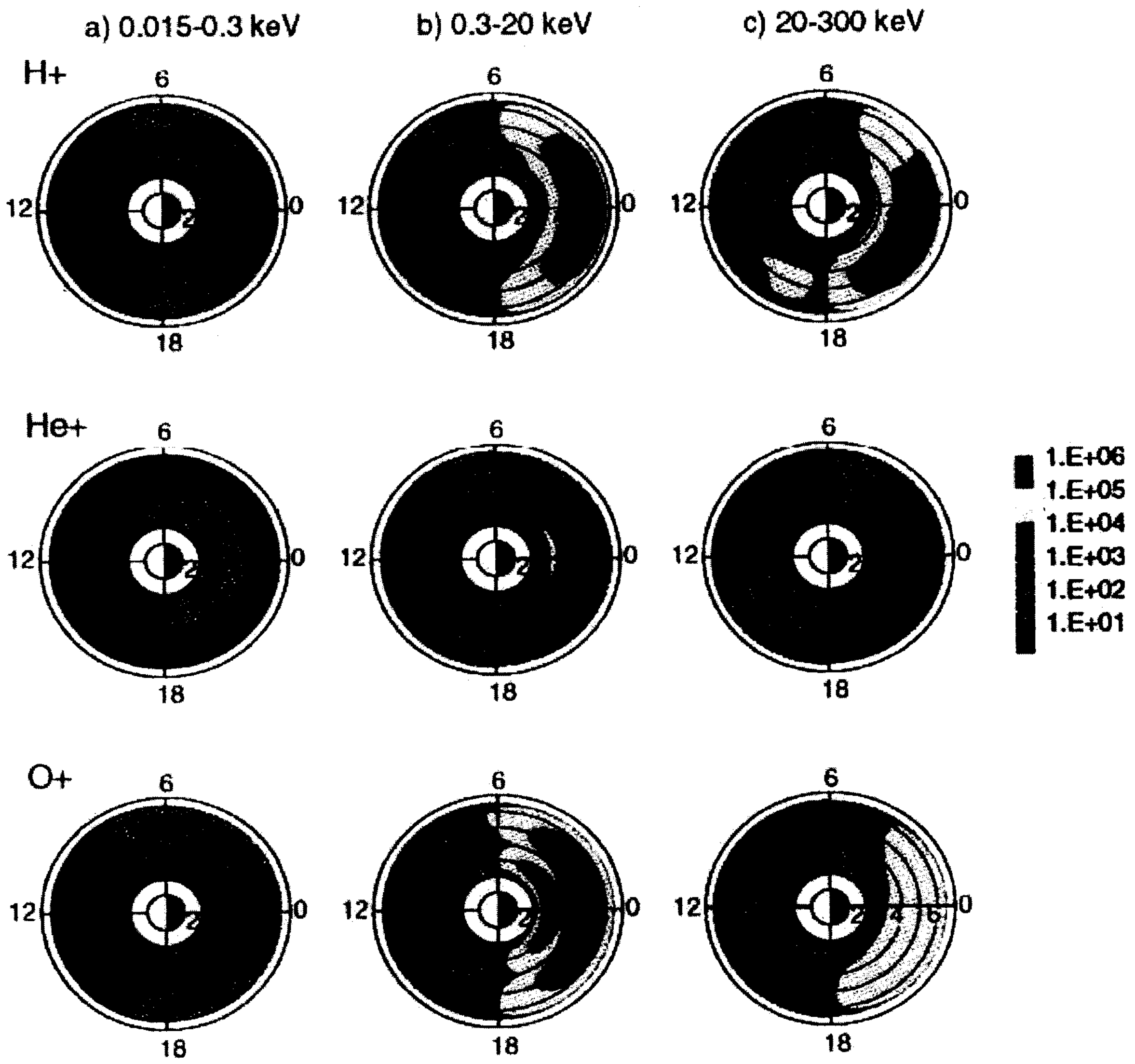

Figure 2-7: Total precipitating flux in particles/(cm^{2}s) at 1000km altitude, 1 hour from the beginning of the recovery phase of the storm for H$^+$ (upper panel), He$^+$ (middle panel), and O$^+$ (lower panel) ring current ions, for three energy ranges: (a) 0.015 – 0.3 keV; (b) 0.3 – 20 keV; (c) 20 – 300 keV (after Jordanova et al., 1996a).

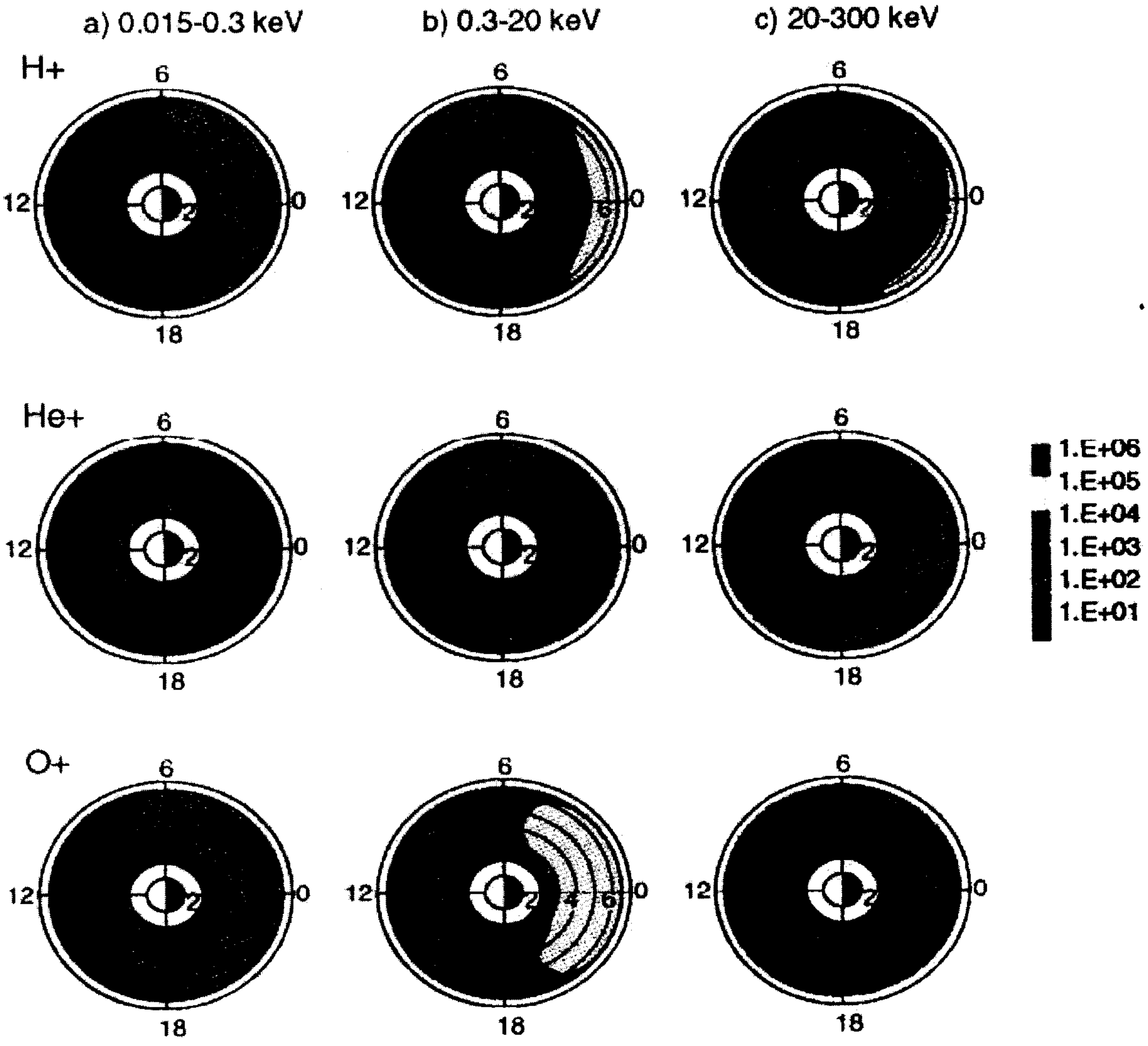

Figure 2-8: Total precipitating flux in particles/(cm^{2}s) at 1000km altitude, 12 hours from the beginning of the recovery phase of the storm for H$^+$ (upper panel), He$^+$ (middle panel), and O$^+$ (lower panel) ring current ions, for three energy ranges: (a) 0.015 – 0.3 keV; (b) 0.3 – 20 keV; (c) 20 – 300 keV (after Jordanova et al., 1996a).

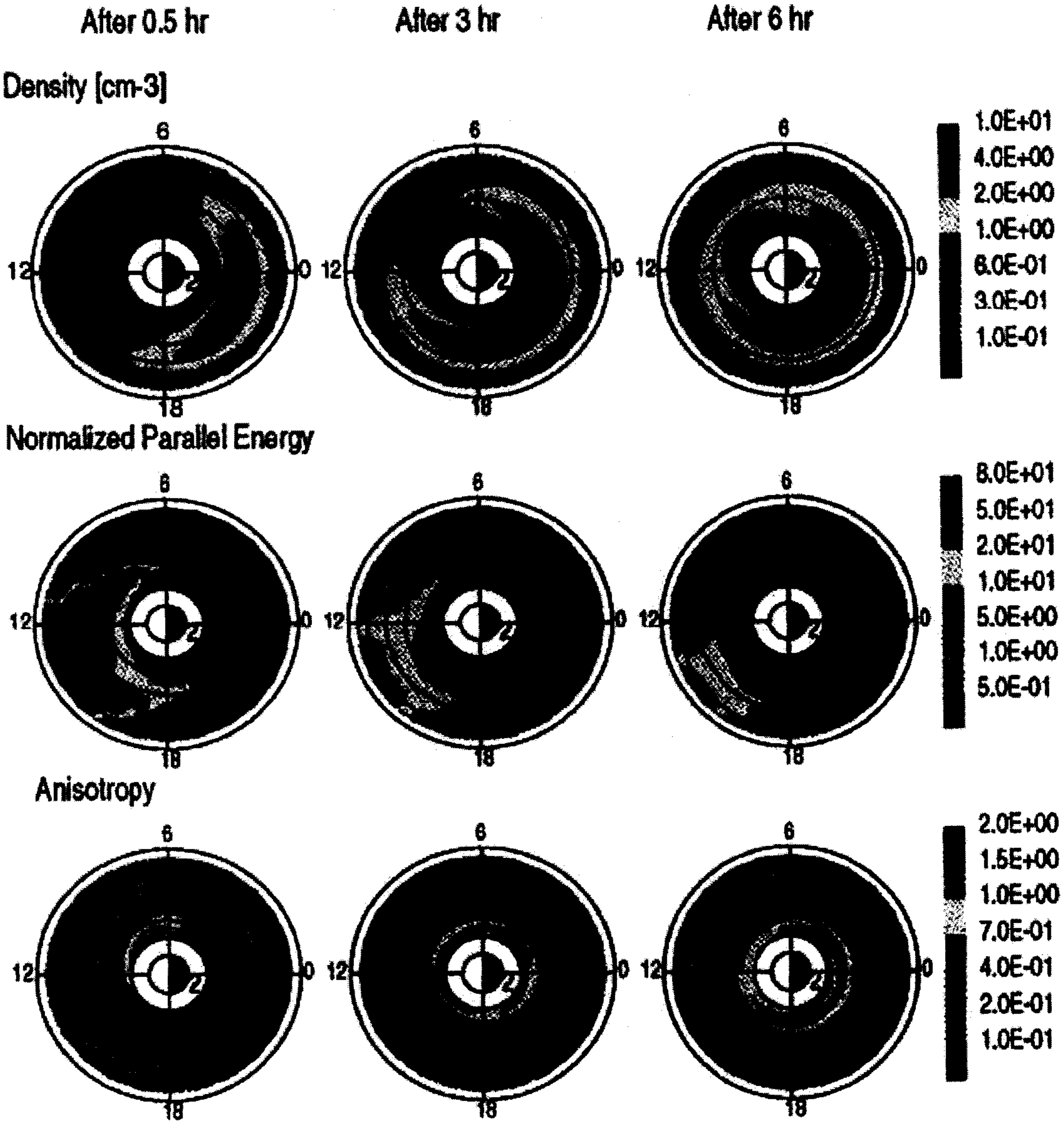

Figure 2-9: Proton ring current characteristics as a function of radial distance in the equatorial plane and magnetic local time, 0.5, 3, and 6 hours after the beginning of the recovery phase: (top) density (cm^{-3}); (middle) normalized parallel energy; (bottom) anisotropy (after Jordanova et al., 1997).

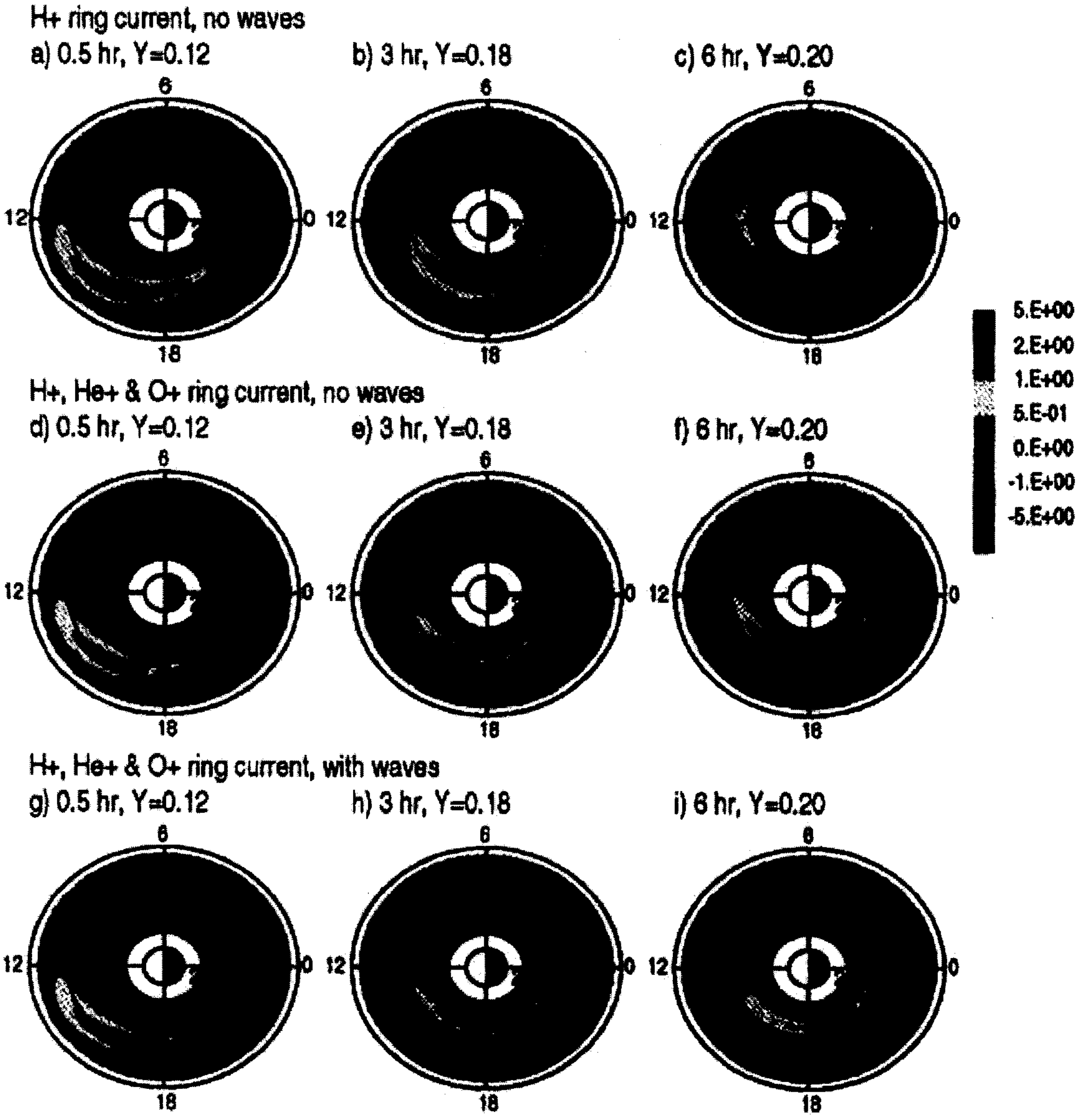

Figure 2-10: Amplification Γ of EMIC waves from the He^+ wave branch as a function of radial distance and magnetic local time, 0.5, 3, and 6 hours after the beginning of the recovery phase: (top) in a proton ring current plasma; (middle and bottom) in a ring current plasma consisting of H^+, He^+, and O^+ ions. The processes of wave-particle interactions are included only in the calculation presented in the lower panel (after Jordanova et al., 1997).

CHAPTER 3

THEORETICAL APPROACH

We study the time evolution of the ring current ion population during various magnetospheric conditions using the bounce-averaged kinetic equation. We have included particle drifts, losses due to charge exchange with geocoronal hydrogen, and atmospheric losses. Wave-particle interactions and Coulomb collisions [Jordanova et al., 1997] are not considered in this work. The ring current particle population is considered to be H^+, He^+, and O^+ ions. The storm time magnetospheric empirical model T04s has been use to represent the Earth's magnetic field. The magnetospheric electric field is represented by the time-dependent Volland-Stern model. Particles with nonequatorial pitch angles are considered. The physics behind the RAM model has been described in great detail in previous studies [Jordanova, 1995; Jordanova et al., 1996a, 1997].

3.1 Kinetic Equation

Energetic charged particles in the Earth's magnetic field undergo gyration around the magnetic filed line, bouncing between the magnetic mirror points, and drifting along a closed surface made up of the magnetic field lines around the Earth. The gyro- and the bounce-motion happen on much shorter time scales than the drift of the particles. That is why it is convenient to average the first two periodic motions over a bounce period in order to simplify the kinetic equation. Then we follow the intersection point of the field line (along which the particle is bouncing) with the equatorial plane. We have assumed that the equatorial plane is orthogonal to all the magnetic field lines at the respective points of intersection. This is not always true for a general magnetospheric field, but for the T04s model it is a good approximation.

We introduce the following variables [Jordanova et al., 1994]: R_0 is the radial distance in the equatorial plane; φ is the geomagnetic east longitude; E is the kinetic energy of the guiding center; $\mu_0 = \cos\alpha_0$, where α_0 is the equatorial pitch angle. Then the bounce-averaged phase space distribution function $Q(R_0, \varphi, E, \mu_0, t)$ is such that QdV represents the mean number of particles for which the coordinates of the guiding center lie in a magnetic flux tube with equatorial area $R_0 dR_0 d\varphi$, and with kinetic energy and cosine of equatorial pitch angle between E and $E + dE$ and μ_0 and $\mu_0 + d\mu_0$ at time t. Then the unit volume element in (R_0, φ, E, μ_0) space is [Jordanova, 1995; Jordanova et al., 1996a]:

$$dV = 8\pi\sqrt{2m_t^3}R_0^2\mu_0\sqrt{E}h(\mu_0)dR_0d\varphi dEd\mu_0 \tag{3.1}$$

where:

$$h(\mu_0) = \frac{1}{2R_0}\int_{s'}^{s''}\frac{ds}{\sqrt{1-\dfrac{B(s)}{B_m}}} \tag{3.2}$$

Here $B(s)$ is the field along the field line s, and s' and s'' are respectively the magnetic mirror points. We assume that the time variations of the magnetospheric fields are slow compared to the particle bounce period and the changes of the distribution function happen on much slower time scale than the gyro- and bounce periods, which is valid for $R_0 < 10$ R$_E$. The phase space distribution function Q is related to the velocity space distribution $F(\vec{r}, \vec{v}, t)$ by $Q = F/m_t^3$, where m_t is the mass of the particle.

The bounce-averaged kinetic equation is [Jordanova, 1995; Jordanova et al., 1996a]:

$$\frac{\partial Q}{\partial t} + \frac{1}{R_0^2}\frac{\partial}{\partial R_0}\left(R_0^2\left\langle\frac{dR_0}{dt}\right\rangle Q\right) + \frac{\partial}{\partial \varphi}\left(\left\langle\frac{d\varphi}{dt}\right\rangle Q\right) + \frac{1}{\sqrt{E}}\frac{\partial}{\partial E}\left(\sqrt{E}\left\langle\frac{dE}{dt}\right\rangle Q\right) + \frac{1}{h(\mu_0)\mu_0}\frac{\partial}{\partial \mu_0}\left(h(\mu_0)\mu_0\left\langle\frac{d\mu_0}{dt}\right\rangle Q\right) = \left\langle\frac{\delta Q}{\delta t}\right\rangle_{loss} \tag{3.3}$$

where:

$$\left\langle\frac{\delta Q}{\delta t}\right\rangle_{loss} = \left\langle\frac{\delta Q}{\delta t}\right\rangle_{ce} + \left\langle\frac{\delta Q}{\delta t}\right\rangle_{atm} \tag{3.4}$$

The first term on RHS considers charge exchange losses and the second term atmospheric losses. The derivation of Equation (3.3) is given in Jordanova [1995]. Bounce-averaging for any quantity χ is defined as:

$$\langle\chi\rangle = \frac{1}{S_b}\int_{s'}^{s''} \chi \frac{ds}{\sqrt{1-\dfrac{B(s)}{B_m}}} \tag{3.5}$$

where S_b is half-bounce path length and is given by:

$$S_b = \int_{s'}^{s''} \frac{ds}{\sqrt{1-\dfrac{B(s)}{B_m}}} \tag{3.6}$$

3.2 Drifts of Ring Current Particles

For typical ring current particle energies ($1-200$ keV) both the $\vec{E}\times\vec{B}$ and the magnetic gradient-curvature drifts are of comparable importance and are considered in the present study. The magnetospheric electric field in the RAM model is calculated as the gradient of the Volland-Stern potential model [Volland, 1973; Stern, 1975], where the time dependence is included through the assumed Kp history. This semiempirical model consists of: a convection field $U_{conv} = AR_0^{\gamma}\sin\varphi$, where φ is the magnetic local time (MLT) in degrees with midnight at 0°; and a corotation field $U_{cor} = -C/R_0$, where $C = 1.44\times10^{-2}\ \mathrm{R}_E^2\mathrm{Vm}^{-1}$.

For the value of the parameter A as a function of Kp, we use the expression determined empirically for $\gamma = 2$ by Maynard and Chen [1975]:

$$A = \frac{7.05 \times 10^{-3}}{(1 - 0.159Kp + 0.0093Kp^2)^3} \frac{\mathrm{mV/m}}{\mathrm{R}_E} \tag{3.7}$$

The contribution of the inductive electric field of a time-dependent ring current is estimated to be much smaller than the Volland-Stern field [e.g., Murphy et al., 1975] and therefore it is neglected in the model.

3.2.1 Radial and Azimuthal Drifts

The instant magnetic gradient-curvature drift velocity of the guiding center at point S can be written as [Rossi and Olbert, 1970]:

$$\mathbf{V}_S = \frac{mV^2}{2qB} \left\{ \sin^2\alpha \frac{\mathbf{B} \times \nabla B}{B^2} + 2\cos^2\alpha \frac{\mathbf{B} \times [(\mathbf{B} \cdot \nabla)\,\mathbf{B}]}{B^3} \right\} \tag{3.8}$$

where V is the thermal particle velocity, and α is the pitch angle at the given point. Using the identity derived in Appendix A:

$$\frac{\mathbf{B}}{B^2} \times [(\mathbf{B} \cdot \nabla)\,\mathbf{B}] = \frac{\mathbf{B} \times \nabla B}{B} + (\nabla \times \mathbf{B})_\perp \tag{3.9}$$

in Equation (3.8) and using that $\sin^2\alpha = B/B_m$, we obtain for the magnetic gradient-curvature drift [Shukhtina, 1993]:

$$\mathbf{V}_S = \frac{mV^2}{qB^2} \left\{ \left(1 - \frac{1}{2}\frac{B}{B_m}\right) \frac{\mathbf{B} \times \nabla B}{B} + \left(1 - \frac{B}{B_m}\right) (\nabla \times \mathbf{B})_\perp \right\} \tag{3.10}$$

where:

$$\mathbf{V}_B = \frac{mV^2}{qB^2} \left(1 - \frac{1}{2}\frac{B}{B_m}\right) \frac{(\mathbf{B} \times \nabla B)}{B} \tag{3.11}$$

is the transverse gradient-curvature drift velocity, and:

$$\mathbf{V}_R = \frac{mV^2}{qB^2}\left(1 - \frac{B}{B_m}\right)(\nabla \times \mathbf{B})_\perp \tag{3.12}$$

corresponds to the drift due to cross-B electric currents [Rossi and Olbert, 1970].

The magnetic field of Earth in the general case is:

$$\mathbf{B}_0 = \left(B_{0\hat{r}}, B_{0\hat{\theta}}, B_{0\hat{\varphi}}\right) \tag{3.13}$$

and in this study is represented by the T04s model [Tsyganenko et al., 2003; Tsyganenko and Sitnov, 2005] which is described more in detail in Section (3.6). The index "0" refers to the equatorial plane.

According to Roederer [1970], only the equatorial electric field:

$$\mathbf{E}_0 = \left[-\left(\frac{C}{R_0^2} + \gamma A R_0^{\gamma-1}\sin\varphi\right), 0, -AR_0^{\gamma-1}\cos\varphi\right] \tag{3.14}$$

contributes to the bounce-averaged drift velocity of the guiding center:

$$\langle \mathbf{V}_D \rangle = \frac{\mathbf{E}_0 \times \mathbf{B}_0}{B_0^2} \tag{3.15}$$

Then the radial drift becomes:

$$\left\langle \frac{dR_0}{dt} \right\rangle = \langle V_D \rangle_{\hat{r}} = AR_0^{\gamma-1}\cos\varphi \frac{B_{0\theta}}{B_0^2} \tag{3.16}$$

Similarly, the azimuthal drift is:

$$\left\langle \frac{d\varphi}{dt} \right\rangle = \frac{\langle V_D \rangle_{\hat{\varphi}} + \langle V_S \rangle_{\hat{\varphi}}}{R_0} = -\left(\frac{C}{R_0^2} + \gamma A R_0^{\gamma-1}\sin\varphi\right)\frac{B_{0\theta}}{B_0^2}\frac{1}{R_0} + \frac{\langle V_S \rangle_{\hat{\varphi}}}{R_0} \tag{3.17}$$

where $\langle V_S \rangle_{\hat{\varphi}}$ is the $\hat{\varphi}$ component of the bounce-averaged value:

$$\langle \mathbf{V}_S \rangle = \frac{1}{S_b} \int_{s'}^{s''} V_S \frac{ds}{\sqrt{1 - \dfrac{B(s)}{B_m}}} = \langle \mathbf{V}_B \rangle + \langle \mathbf{V}_R \rangle \tag{3.18}$$

Here V_S is the magnetic gradient-curvature drift velocity given by Equation (3.10) [Shukhtina, 1993].

3.2.2 μ_0 – Drift

The bounce-averaged rate of change of the cosine of the particle's equatorial pitch angle is derived from the conservation of the first (M) and the second (J) adiabatic invariants. We use the following relationship between M and J [e.g. McIlwain, 1966]:

$$\frac{M}{J^2} = \frac{\left[\dfrac{P^2 \sin^2 \alpha}{2m_0 B}\right]}{[2R_0 P I^2]} = \frac{\sin^2 \alpha_0}{8m_0 R_0^2 B_0 I^2} = \frac{(1 - \mu_0^2)}{8m_0 R_0^2 B_0 I^2} = const \tag{3.19}$$

where we use that:

$$\frac{\sin^2 \alpha}{B} = \frac{\sin^2 \alpha_0}{B_0} \tag{3.20}$$

and:

$$\sin^2 \alpha_0 = y^2 \implies \mu_0^2 = \cos^2 \alpha_0 = 1 - y^2 \tag{3.21}$$

Differentiating with respect of time yields:

$$\frac{d}{dt}\left(\frac{M}{J^2}\right) = 0 \tag{3.22}$$

and using the relation [Ejiri, 1978]:

$$\frac{d}{dy}[I(y)] = \frac{I(y)}{y} - \frac{2h(y)}{y} \tag{3.23}$$

after some algebra: finally for the μ_0-drift we get:

$$\left\langle\frac{d\mu_0}{dt}\right\rangle = \frac{(1-\mu_0^2)}{4R_0\mu_0}\frac{I(\mu_0)}{h(\mu_0)}\left\langle\frac{dR_0}{dt}\right\rangle \tag{3.24}$$

where:

$$I(\mu_0) = \frac{1}{R_0}\int_{s'}^{s''}\sqrt{1-\frac{B(s)}{B_m}}ds \tag{3.25}$$

3.2.3 Energy Drift

The magnetic moment of a particle in a magnetic field is:

$$\mu = \frac{mV_\perp}{2B} \tag{3.26}$$

Using Equation (3.21) we obtain:

$$\mu = \frac{mV_\perp}{2B} = \frac{mV^2\sin^2\alpha}{2B} = \frac{mV^2\sin^2\alpha_0}{2B_0} = \frac{Ey^2}{B_0} \tag{3.27}$$

From the preservation of the first adiabatic invariant we have:

$$\left\langle\frac{dE}{dt}\right\rangle = -\frac{3E}{R_0}\left[1-\frac{I(\mu_0)}{6h(\mu_0)}\right]\left\langle\frac{dR_0}{dt}\right\rangle \tag{3.28}$$

3.3 Charge Exchange Losses

The particles in the ring current (2 – 9 R$_E$) experience collisions with geocoronal hydrogen. Single charge exchange between H$^+$ and atmospheric hydrogen most effectively decreases the population of geomagnetically trapped particles [Stuart, 1959; Dessler and Parker, 1959, e.g.]. The result is the generation of high energy neutral atoms and low energy protons. For such a process the loss rate can be written as:

$$\left\langle \frac{\partial Q}{\partial t} \right\rangle = -\sigma_t \sqrt{\frac{2E}{m_t}} \left\langle n_H \right\rangle Q \tag{3.29}$$

Here σ_t is the charge exchange cross section of the ion species t colliding with the neutral hydrogen with number density n_H. Multiple charge exchange processes become important at energies above ~100 keV [Spjeldvik and Fritz, 1978] and are neglected in this study.

Rairden et al. [1986] used the geocoronal measurements (emissions of scattered solar Lyman α radiation) from Dynamics Explorer 1 (DE 1) combined with the Chamberlain model [Chamberlain, 1963] and numerical solutions of the radiative transfer equations to develop a hydrogen density model at high altitudes (Figure 3-1). Rairden et al. [1986] found that the hydrogen profiles vary little with the changes in the solar wind, which was confirmed by later studies [Hodges, 1994; Østgaard et al., 2003, e.g.]. The model has been widely used in the analysis of ring current and ENA generation rates [Kistler et al., 1989; Jordanova et al., 1994, 1997; Fok et al., 1995].

To obtain the bounce-averaged densities at every point along a magnetic field line, first we interpolate the exospheric hydrogen density [Rairden et al., 1986] using the function:

$$N_H = 10.0^Y \tag{3.30}$$

where

$$Y = a_0 + a_1 X + a_2 X^2 + a_3 X^3 + a_4 X^4 \tag{3.31}$$

Here X is the distance from Earth and the coefficients a are:

$$a_0 = 13.326, a_1 = -3.6908, a_2 = 1.1362, a_3 = -0.16984, a_4 = 0.009552.$$

The above formula is valid for L-shells from 1.5 to 6.5 and its fit to the Chamberlain model data is given in Figure (3-2). Then we bounce-average the hydrogen densities using the following formula [Schulz and Blake, 1990]:

$$\langle H_{Dens} \rangle = \frac{1}{4R_0 h(\mu_0)} \oint \frac{N_H(s)}{\sqrt{1 - \frac{B(s)}{B_m}}} ds \tag{3.32}$$

In the present study we consider that the ring current consists of H^+, He^+, and O^+ ions. The measurements for the charge exchange cross sections σ_t, extending to low ion energies, are obtained from the Oak Ridge National Laboratory (ORNL). Phaneuf et al. [1987] provide data for the charge exchange cross sections of O^+ ions colliding with neutral hydrogen gas, while Barnet [1990] - for those of H^+ and He^+ ions. These measurements together with the corresponding polynomial fits used in this study are shown in Figure (3-3, after Fok et al. [1993])

3.4 Atmospheric Losses

Ring current particles with smaller pitch angles mirror closer to Earth and thus encountering denser atmosphere. Some particles reach very low altitudes where the atmospheric density is large enough that the scattering of these particles is highly probable. A particle mirroring at such a low altitude is very likely to be "absorbed" by the atmosphere and hence lost from the radiation belts. This altitude, at which absorption occurs, determines the loss cone boundary, and in the RAM model it is assumed to be 200km.

The absorption of ring current particles in the atmosphere, due to emptying of the loss cone (twice per bounce period τ_b) is taken into account by introducing the loss term [Lyons, 1973]:

$$\left\langle \left(\frac{\partial Q}{\partial t} \right)_{atm} \right\rangle = -\frac{Q}{\tau_{atm}}, \text{ where } \tau_{atm} = \begin{cases} \tau_B/2 & \text{, inside the loss cone} \\ \infty & \text{, outside the loss cone} \end{cases} \tag{3.33}$$

where:

$$\tau_B = \frac{2}{v} \int_{s'}^{s''} \frac{ds}{\sqrt{1 - \frac{B(s)}{B_m}}} = \frac{4R_0}{v} h(\mu_0) \tag{3.34}$$

The spatial variations of the distribution function Q within the loss cone due to atmospheric collisions at low altitudes are neglected.

3.5 Ring Current Characteristics and Aeronomical Effects

This section describes the calculation of different characteristics and aeronomical effects of ring current decay in RAM-ND. The ring current parameters are obtained by taking the moments of the distribution function Q.

The total number of ring current particles and the total ring current energy are respectively [Jordanova, 1995]:

$$N_{tot} = \int Q dV = 8\pi \sqrt{2m_t^3} \int_{R_1}^{R_2} dR_0 \int_0^{2\pi} d\varphi \int_{E_1}^{E_2} dE \int_0^{\mu_{oc}} d\mu_0 R_0^2 \mu_0 \sqrt{E} h(\mu_0) Q \tag{3.35}$$

$$E_{tot} = \int E Q dV = 8\pi \sqrt{2m_t^3} \int_{R_1}^{R_2} dR_0 \int_0^{2\pi} d\varphi \int_{E_1}^{E_2} dE \int_0^{\mu_{oc}} d\mu_0 R_0^2 \mu_0 E^{3/2} h(\mu_0) Q \tag{3.36}$$

Here R_1,R_2,E_1,E_2 are the lower and upper radial and energy boundaries and μ_{oc} is the cosine of the equatorial pitch angle, corresponding to the upper edge of the atmospheric loss cone.

The quantitative relationship between the energy density contained in the ring current and the resulting perturbation in the magnetic field at the surface of the Earth is given by the

Dressler-Parker-Sckopke (DPS) relation (Equation 2.5), which for a dipole approximation can be rewritten in standart units in the following form:

$$\Delta B[\text{nT}] = (3.98 \times 10^{-30}) E_{tot}[\text{keV}] \tag{3.37}$$

The above change in the Earth's magnetic field is the *Dst* index due to the development in the stormtime ring current.

The number density and the energy density of a ring current specie t at a given point in the equatorial plane are respectively:

$$n_t(R_0, \varphi) = 4\pi \int dp_{\|} dp_{\perp} Q p_{\perp} = 4\pi \sqrt{2m_t^3} \int_{E_1}^{E_2} dE \int_0^{\mu_{oc}} d\mu_0 \sqrt{E} Q \tag{3.38}$$

$$E_t(R_0, \varphi) = 4\pi \int dp_{\|} dp_{\perp} E Q p_{\perp} = 4\pi \sqrt{2m_t^3} \int_{E_1}^{E_2} dE \int_0^{\mu_{oc}} d\mu_0 E^{3/2} Q \tag{3.39}$$

The relation between the phase space distribution function Q and the magnitude of the equatorial directional flux j_0, defined as the number of particles of specie t with unit energy and unit solid angle, crossing unit equatorial area perpendicular to their direction of incidence per unit time is:

$$j_0 = 2 m_t E Q \tag{3.40}$$

3.6 Tsyganenko Magnetospheric Field Model

In our study we use T04s magnetospheric field model [Tsyganenko et al., 2003; Tsyganenko and Sitnov, 2005] as a replacement for the dipole field which has been used to approximate the Earth's magnetic field in the previous version of RAM model. The T04s model is based on a set of data, containing only events with $Dst \leq -65$ nT, representing strongly disturbed configurations of the near geomagnetic field ($R < 15$ R$_E$) and their evolution during the storm cycle. In all cases, only those storms were selected for which concurrent solar wind and IMF data were available for the entire duration of the event. Interplanetary medium data were provided by Wind, ACE, IMP 8 and Geotail. The inner magnetospheric field is computed using the T01 model [Tsyganenko, 2002a,b], with a duskside partial ring current with variable amplitude and scale size, an essential part of the storm-time current system. The T04s model describes well the magnetospheric configuration for both quiet and disturbed conditions [Tsyganenko and Sitnov, 2005].

Following the general approach presented in detail in previous versions of the Tsyganenko model [Tsyganenko, 2002a,b], the external model field in T04s is approximated by a linear combination of seven vectors: (1) the Chapman-Ferraro field B_{CF}, confining the Earths internal field within the magnetopause, (2) the tail field B_T, (3) the field B_{SRC} of a symmetrical ring current, (4) the field of a partial ring current B_{PRC}, (5) – (6) the fields of the Region 1 and 2 Birkeland current systems, and (7) a penetrated component of the IMF given by an "interconnection" term $B_{int} = \varepsilon B_{\perp}^{IMF}$. The T04s model uses as input parameters Solar Wind Ram Pressure (P), Dst index, IMF B_y, IMF B_z, and six variables W1-W6 which are calculated according to the IMF B_z, alpha-to-proton ratio, solar wind proton density, and solar wind velocity values [Tsyganenko and Sitnov, 2005].

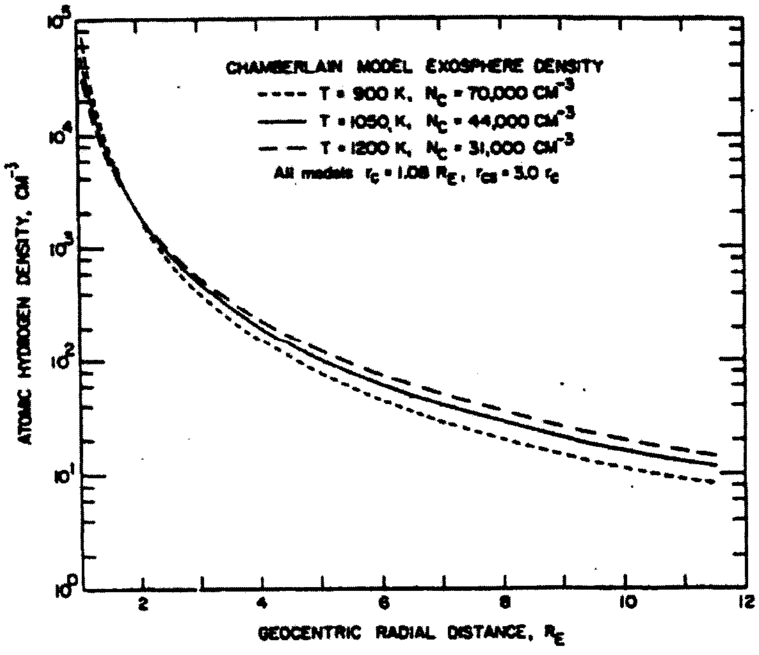

Figure 3-1: Exospheric hydrogen density versus radial distance for different Chamberlain model fits. The solid line is the model that provides best fit the the DE 1 geocoronal observations (after Rairden et al., 1986).

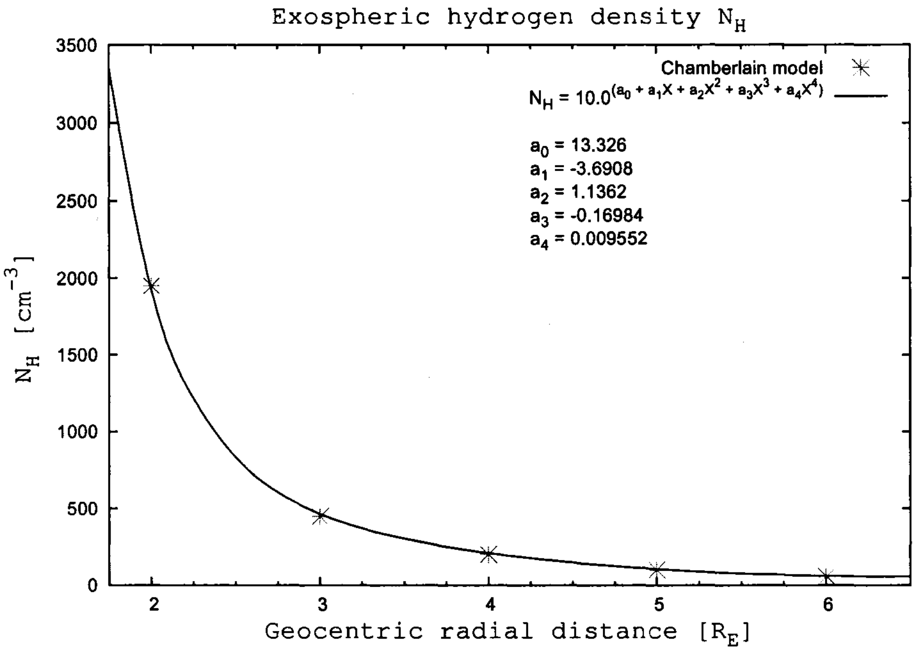

Figure 3-2: Analytical fit of the function in Equation (3.30) (solid line) to the Chamberlain model data (stars).

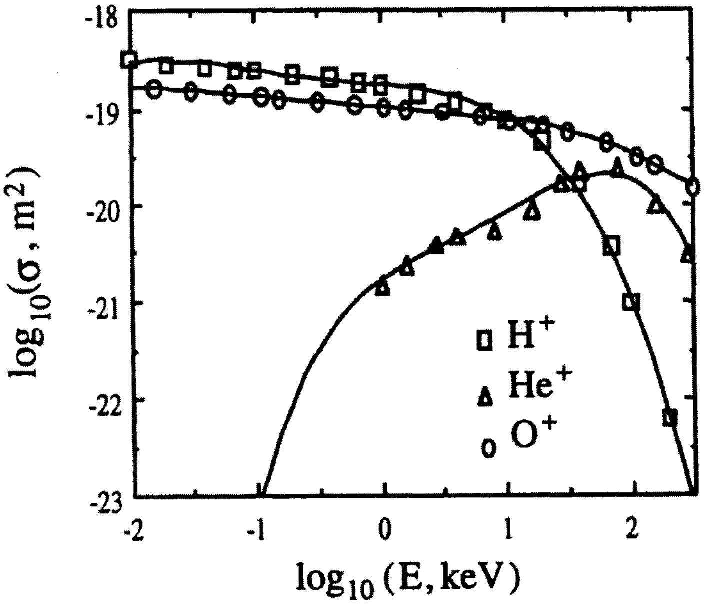

Figure 3-3: Charge exchange cross sections of H^+, He^+, and O^+ reported by Oak Ridge National Laboratory (Phaneuf et al., 1987; Barnett, 1990). Solid lines are polynomial fits (after Fok et al., 1993).

CHAPTER 4

THE NUMERICAL MODEL

4.1 The Numerical Scheme of RAM

The bounce-averaged kinetic equation (3.3) is solved with a time-splitting numerical scheme, i.e. the finite difference algorithm is split into a sequence of one-dimensional simple equations, and the solution is advanced at each time step by a single operator. The order of the solution operators is reversed in the next time step to achieve second order accuracy in time. A flux-limiter high-resolution scheme is used to solve the first order advective terms. An exact solution exists for the charge exchange and the atmospheric loss terms. The complete details of the model are given in Jordanova [1995].

4.1.1 Time splitting

The splitting operators for the bounce-averaged equation (3.3) are given in Jordanova [1995]. The time-splitting numerical scheme of Yanenko [1971] is the method used to solve Equation (3.3) in multi-dimensions. The idea is to reduce the multi-dimensional scheme to one-dimensional methods, applied alternately for each dimension.

Suppose we have an equation of the form:

$$\frac{\partial u}{\partial t} = Lu \tag{4.1}$$

where the operator L is a sum of several additive operators:

$$L = L^1 + L^2 + ... + L^n \tag{4.2}$$

Then an approximate solution is found by solving a system of simple one-dimensional equations:

$$\left| \begin{array}{l} \dfrac{\partial u}{\partial t} = L^1 u \\ \dots \\ \dfrac{\partial u}{\partial t} = L^n u \end{array} \right. \tag{4.3}$$

where the solution of each equation is used as an initial condition for the next one. Further, second order accuracy for each of the one-dimensional schemes can be achieved using the Strang time splitting method [Strang, 1968]: each one-dimensional solution is advanced over the first half time step and then reversed in order to complete the time step.

4.1.2 High – Resolution Schemes

In the RAM model, the finite volume method is used to solve the first order terms in equation (3.3) as described in Jordanova [1995]. In the finite volume method, volume integrals in a partial differential equation that contain a divergence term are converted to surface integrals. These terms are then evaluated as fluxes at the surfaces of each finite volume. The values of the conserved variables are located within the volume element, and not at nodes or surfaces. Further, the fluxes are computed using either first order upwind scheme, or a second order Lax-Wendroff numerical scheme, depending on the smoothness of the solution. These methods have been described in great detail elsewhere [Flannery et al., 1992; Jordanova, 1995; Chung, 2002].

4.2 Bounce – Averaging along a Field Line

The analytic expressions for the integrals in equations (3.2) and (3.25) can be explicitly written for a dipole magnetic field [e.g., Ejiri, 1978]. Explicit solutions in the case of a dipole field can also be derived for the bounce-averaged gradient-curvature particle drift velocity [e.g., Roederer, 1970] and the bounce-averaged exospheric hydrogen density [e.g., Schulz and Blake, 1990]. For a realistic model of the magnetospheric field, the particle drift paths, velocities, and respective bounce-averaged quantities must be computed numerically.

Starting in the SM equatorial plane, first we trace the lines southward and then northward until we reach the ionosphere. Then we interpolate the magnetic field between each pair of tracing points (s_1, s_2) using simple linear polynomials (Figure 4-1). If s_1 and s_2 denote distances from the beginning of the magnetic line to the respective two points, then for such a pair of points we can write a system of two linear equations:

$$\left| \begin{array}{l} B(s_1) = a_B s_1 + b_B \\ B(s_2) = a_B s_2 + b_B \end{array} \right. \tag{4.4}$$

where the magnetic field B along the field line is written as a function of the field line length s. Thus, for each pair of points we can find the polynomial coefficients a_B and b_B. If the tracing step is properly chosen, then the linear approximation gives a fast and accurate solution. In our model we use an adaptive tracing step. It becomes smaller close to the ionosphere and the equatorial plane in SM coordinates.

After we find a and b for each pair (s_1, s_2) we can find the exact location of the mirror points defined by the relation for a given equatorial pitch α_0:

$$\sin \alpha_0 = \frac{B_0}{B_m} \tag{4.5}$$

where B_m is the magnetic field at the mirror point. The index 0 refers to the Solar Magnetic (SM) equatorial plane.

Using the above results, we approximate the integrals in equations (3.2) and (3.25):

$$\int_{s_1}^{s_2} \frac{ds}{\sqrt{1-\dfrac{B(s)}{B_m}}} \to \int_{s_1}^{s_2} \frac{ds}{\sqrt{1-\dfrac{a_B s+b_B}{B_m}}} = -\frac{2B_m}{a_B}\left(1-\frac{a_B s+b_B}{B_m}\right)^{\dfrac{1}{2}}\Bigg|_{s_1}^{s_2} \tag{4.6}$$

$$\int_{s_1}^{s_2} \sqrt{1-\frac{B(s)}{B_m}}\,ds \to \int_{s_1}^{s_2} \sqrt{1-\frac{a_B s+b_B}{B_m}}\,ds = -\frac{2B_m}{3a_B}\left(1-\frac{a_B s+b_B}{B_m}\right)^{\dfrac{3}{2}}\Bigg|_{s_1}^{s_2} \tag{4.7}$$

This numerical technique removes the singularity from the denominator in the first integral. Thus, we calculate the integrals for each of the two points located between the two mirror points s' and s'' (including s' and s''). Then we sum the results in order to find the overall value of $h(\mu_0)$ and $I(\mu_0)$ for a given field line and equatorial pitch angle.

We use the same method to compute the bounce-averaged gradient curvature velocity and hydrogen density. We find the respective pairs of linear coefficients (a_n, b_n) and approximate the integrals (which are of the same type) in equations (3.18) and (3.32):

$$\begin{aligned}\int_{s_1}^{s_2} \frac{n(s)}{\sqrt{1-\dfrac{B(s)}{B_m}}}\,ds \to \int_{s_1}^{s_2} \frac{a_n s+b_n}{\sqrt{1-\dfrac{a_B s+b_B}{B_m}}}\,ds = \\ -\frac{2B_m}{3a_B}\left(1-\frac{a_B s+b_B}{B_m}\right)^{\dfrac{1}{2}}(a_n a_B s+2a_n B_m-2a_n b_B+3b_n a_B)\Bigg|_{s_1}^{s_2}\end{aligned} \tag{4.8}$$

Again the singularity in the denominator is removed and then the integration proceeds as described above. All numerical derivatives along a field line are computed as simple first order finite differences.

4.3 Numerical Accuracy Tests of the Bounce – Averaging Technique

The proper calculation of the integrals in equations (3.2) and (3.25) is of major importance for the implementation of a non-dipole magnetic field in RAM. To estimate the accuracy of the numerical technique described above, first we calculate $h(\mu_0)$ and $I(\mu_0)$ as a function of the pitch angle for a dipole field configuration and compare them with their analytic values [Ejiri, 1978]. The results are presented in Figures (4-2) and (4-3) respectively. Both plots show that the numerical calculation overlaps with the analytic curve for the most part except for small pitch angles. The slight difference is due to extrapolation at small pitch angles. The smaller the pitch angle is, the farther from the equatorial plane the particle travels along a field line. The farthest a particle can travel is until it reaches the ionosphere. This travel distance along the field line corresponds to some critical equatorial pitch angle value which defines the loss cone [e.g., Parks, 2004]. Thus, for pitch angle values smaller than the loss cone pitch angle we need to extrapolate in order to find the integrals for $h(\mu_0)$ and $I(\mu_0)$. For this we use 3rd order polynomials. Due to the cosine nature of the analytical curve, these polynomials are not very successful in the region of pitch angles close to 0. The numerical error in this case can reach $\sim 3\%$.

The comparison of the analytical bounce-averaged hydrogen densities and the computed ones (equation 3.32) versus distance from Earth for a dipole field is shown in Figure (4-4). The results are presented for pitch angles 20, 50, and 80 degrees. The numerically calculated $\langle H_{Dens} \rangle$ fits well the analytical function for big pitch angles (50 and 80 degrees), i.e. pitch angles greater than the loss cone, for all radii. For smaller pitch angles there is a slight difference between the calculated $\langle H_{Dens} \rangle$ and the analytical curve at lower L-shells due to extrapolation. The analytical bounce-averaged density behaves in a way similar to an exponential. Here we extrapolate using a second order polynomial. This choice of the extrapolating function is due to some numerical limitations. Closer to Earth the magnetic field lines are shorter in length and the result is smaller number of tracing steps for a field line. Also, there is a limit to how small the tracing step can be because of computational error restrictions. These two factors define the maximum possible number of tracing points over a field line. For strongly distorted stormtime field the number of points describing a line close to Earth can be as little as $\sim 5-10$ points. This is not enough to perform exponential extrapolation. For this particular case 3rd order polynomials are also possible, but their oscillations around the analytical curve are stronger. Another reason for not choosing an exponential extrapolation is that its increase is too rapid and could yield quite erroneouss results. Again the numerical error can reach $\sim 3\%$ for small pitch angles.

Figure (4-5) shows the bounce-averaged magnetic curvature drift velocity versus distance from Earth for pitch angles 20, 50, and 80 degrees. A third order polynomial extrapolation is then applied for small pitch angles. The numerically computed $\langle V_S \rangle$ (equation 3.18) is in a good agreement with the analytical values for a dipole field even for small pitch angles [e.g., Roederer, 1970]. The contribution of $\langle V_R \rangle$ in equation (3.18) is zero in the dipole case because of the symmetry in the field geometry. In order to check the accuracy of our computational method for $\langle V_R \rangle$ we plot the relative difference between $\langle V_S \rangle$ (equation 3.18) and $\langle V_B \rangle$ in Figure (4-6). The highest values are about 0.6% which is much smaller than our numerical error.

4.4 Accuracy Tests for RAM

To test the implementation of the numerical techniques in our non-dipole model RAM-ND we run calculations for a dipole field configuration and compare the results with those from RAM. Here we present tests for the time evolution of the trapped equatorial particle flux, the total energy and total particle number for H^+ ions. The results are for the geomagnetic storm of April 21-25, 2001, which is discussed in greater detail in Chapter 5. Here we present test results for hour 12 (quiet prestorm period, $Dst = -6$, $Kp = 1$) and hour 36 (around the storm peak, $Dst = -64$, $Kp = 5$).

4.4.1 Equatorial Particle Flux

The time evolution of the equatorial particle flux for H^+ ions is shown in Figures (4-7) through (4-12). Each table shows plots for MLT=0, 9, 15 and L=2, 4, 6. The plots are for PA=20, 50, 80 degrees and DOY 2001:111 at 12:00 UT and DOY 2001:112 at 36:00 UT. The calculation starts at hour 10.5 (DOY 2001:111 at 10:30 UT). The plots for hour 12 basically present the initial quiet phase of the storm and the plots at hour 36 are for the peak of the storm.

The results for PA=20, hour 12 are shown in Figure (4-7). The fluxes for L=2 and MLT=0, 9 for RAM and RAM-ND coincide well for the whole energy range. For L=2, MLT=15 RAM-ND gives a little higher flux for energy of about 230 keV. For L=4 the flux for both models are the same except for MLT=0 where there is a little difference for energies > 200 keV. For L=6 RAM-ND gives slightly different fluxes for energies > 200 keV and for MLT=9 there is a difference in the low energy range. The error is much smaller than our numerical error of about 3% in the bounce-averaging technique.

For PA=20, hour 36 RAM-ND and RAM give equal results. There are slight differences for L=2 and MLT=0, 15 for high energies, and also for L=4, 6 and MLT=9 in the $\sim 20-50$ keV energy range.

The calculations for PA=50 degrees are in a good agreement for both models. For hour 12, L=6, MLT=9 the flux differs for low energies and again for energy > 200 keV. The results for hour 36 for the all nine plots show that RAM-ND coincide very well with the RAM calculations.

For PA=80 degrees the agreement for RAM and RAM-ND is very good. The results only differ for hour 12, L=6, MLT=9 for the low energy range and for L=2, 4 and MLT=15 they differ slightly for the high energy range. For hour 36 the difference is only for L=2, MLT=0 for the high energies and for L=4, MLT=9 for energy of $\sim$ 20 keV.

4.4.2 Total Energy and Total Number of Particles

A different way to test the numerical stability of our model is to examine the total ring current energy and the total particle number. The total ring current energy for the April 2001 storm period is plotted in Figure (4-13) for RAM and RAM-ND with a dipole field. The time axis shows hours after 0:0 UT on April 21. The RAM-ND model gives results which are in a good agreement with RAM. The highest difference of about 3% is at hour 40. The situation for both models for the total particle number in Figure (4-14) is simillar. The biggest difference between the particle number calculated by the two models again is around hour 40.

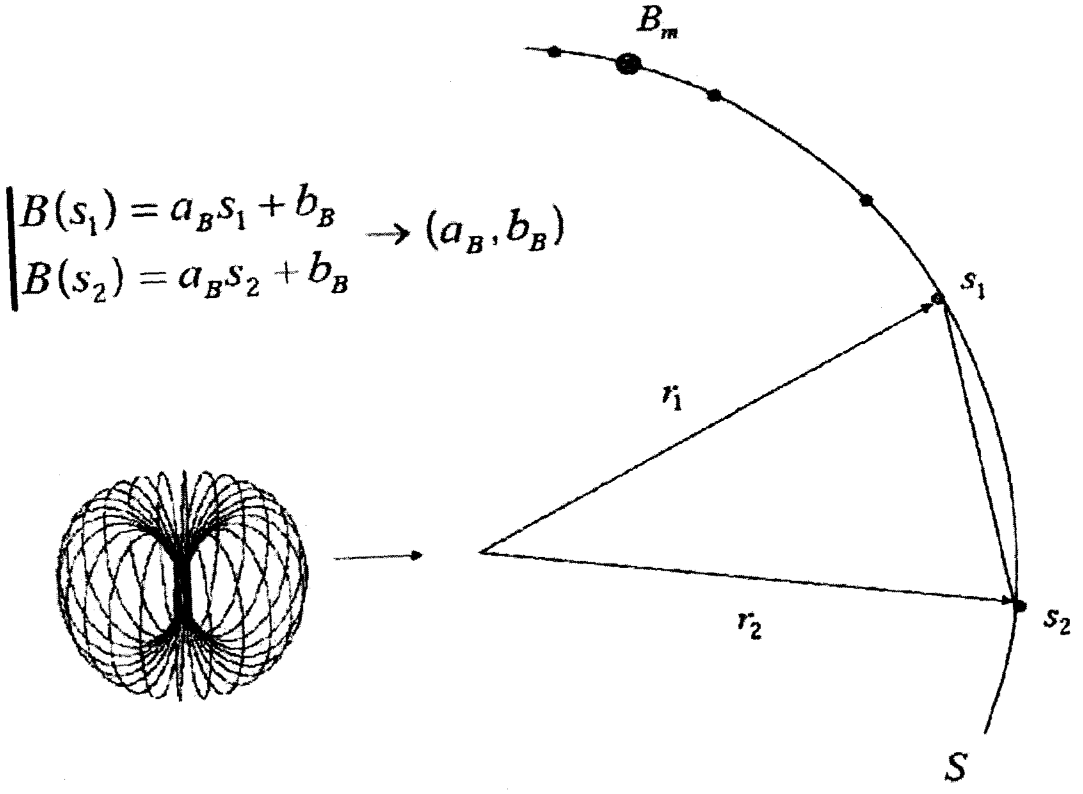

Figure 4-1: This figure shows a representative field line tracing and the individual steps (solid circles). At each tracing step we find the values of the variable $B(s)$. Then we use linear interpolation between each pair of points. We integrate the acquired linear polynomials and sum them to find the total integral value over the field line between the two mirror points s' and s''. The exact position of each mirror point (the position of B_m) is found using the respective linear interpolation polynomial between the corresponding tracing points.

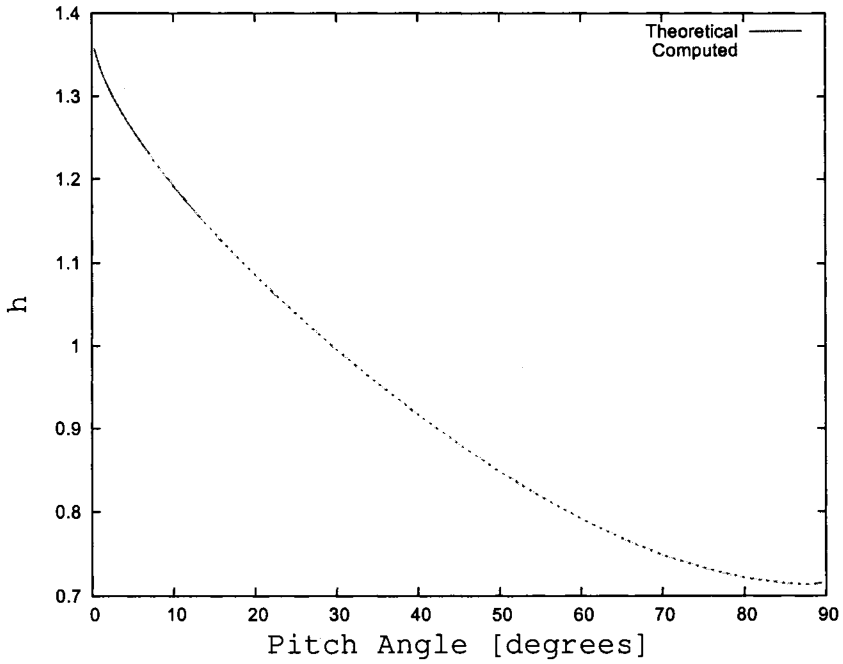

Figure 4-2: Comparison between the theoretical (red) and numerically computed (green) $h(\mu_0)$ as a function of the pitch angle for dipole magnetic field.

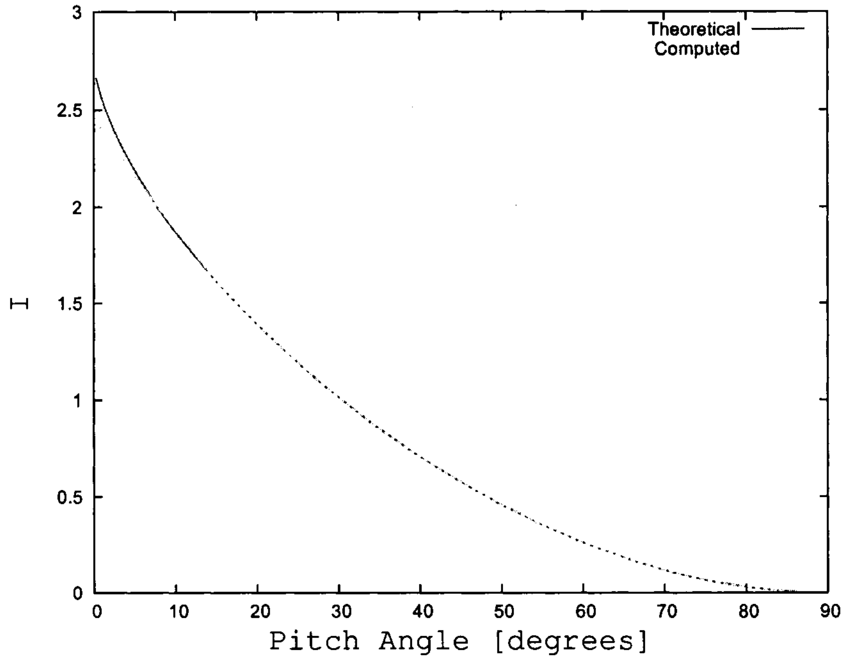

Figure 4-3: Comparison between the theoretical (red) and numerically computed (green) $I(\mu_0)$ as a function of the pitch angle for dipole magnetic field.

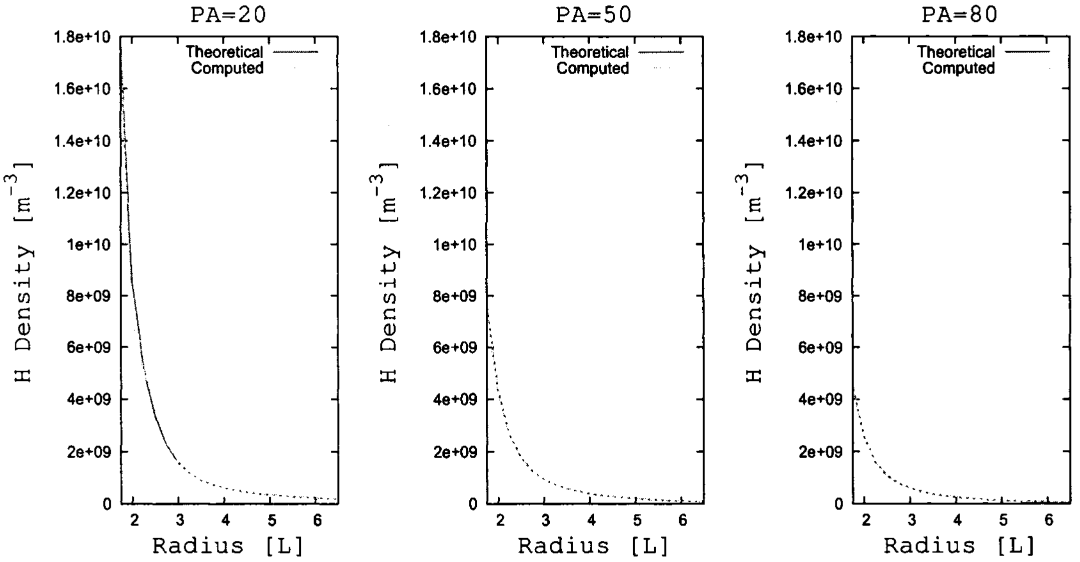

Figure 4-4: Comparison between the theoretical (red) and numerically computed (green) bounce-averaged hydrogen density $\langle H_{Dens} \rangle$ as a function of the distance to Earth for three pitch angle 20 (left), 50 (middle) and 80 (right) degrees for dipole magnetic field.

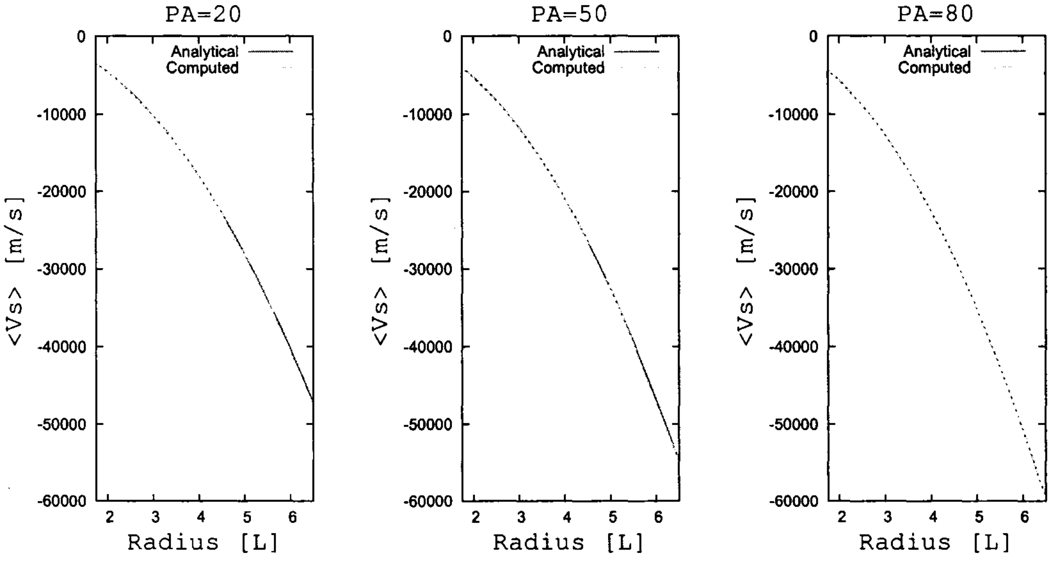

Figure 4-5: Comparison between the theoretical (red) and numerically computed (green) bounce-averaged magnetic curvature drifts velocity $\langle V_S \rangle$ versus distance from Earth for pitch angles 20, 50, and 80 degrees and for energy 100 keV

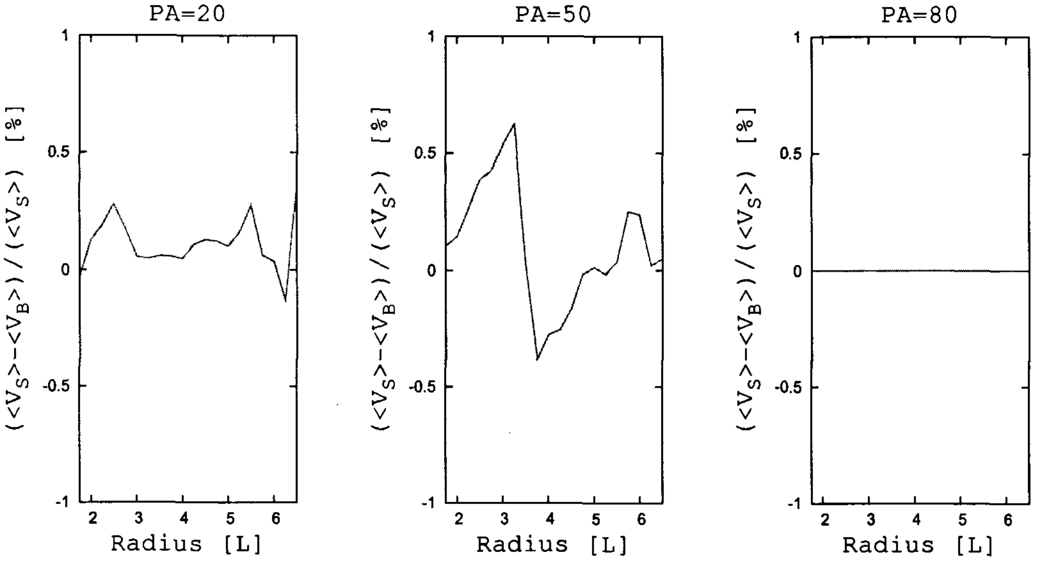

Figure 4-6: Contribution of $\langle V_R \rangle$ in equation (3.18) presented as a relative difference versus distance from Earth for pitch angles 20, 50, and 80 degrees and for energy 100 keV.

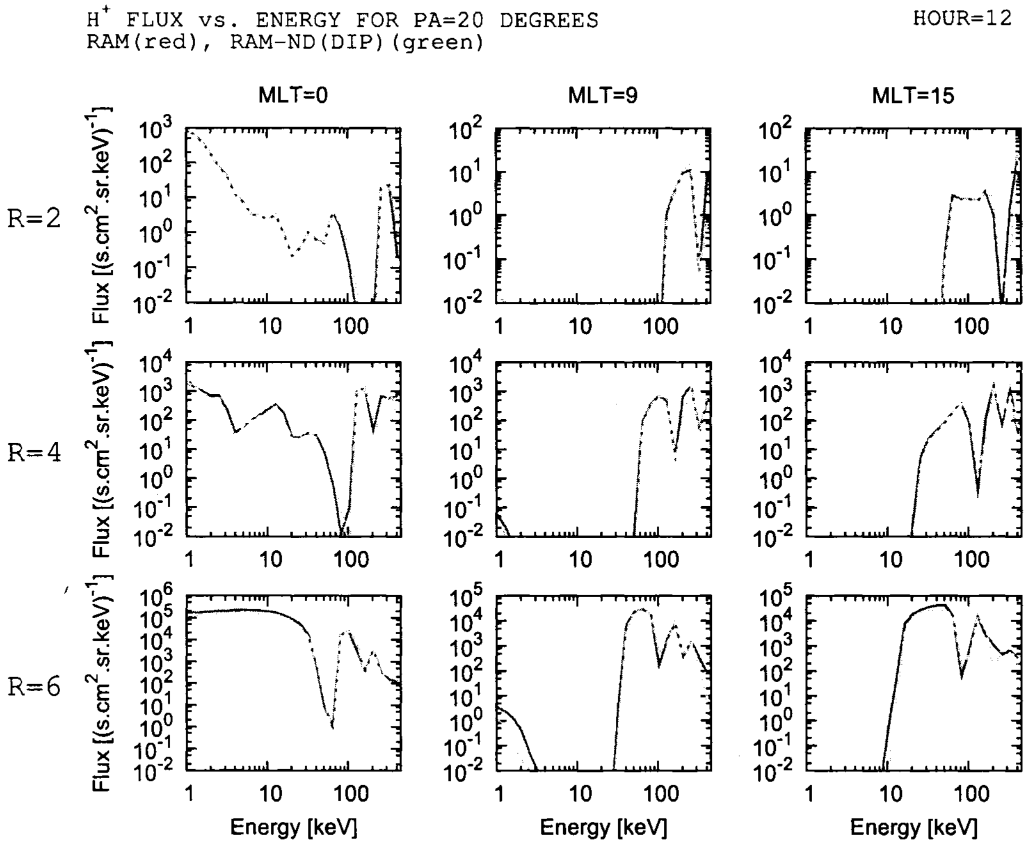

Figure 4-7: Trapped equatorial H$^+$ flux vs. energy for MLT=0, 9, 15, L=2, 4, 6, PA=20°, hour 12 after the beginning of the storm (DOY 2001:111 at 12:00 UT)

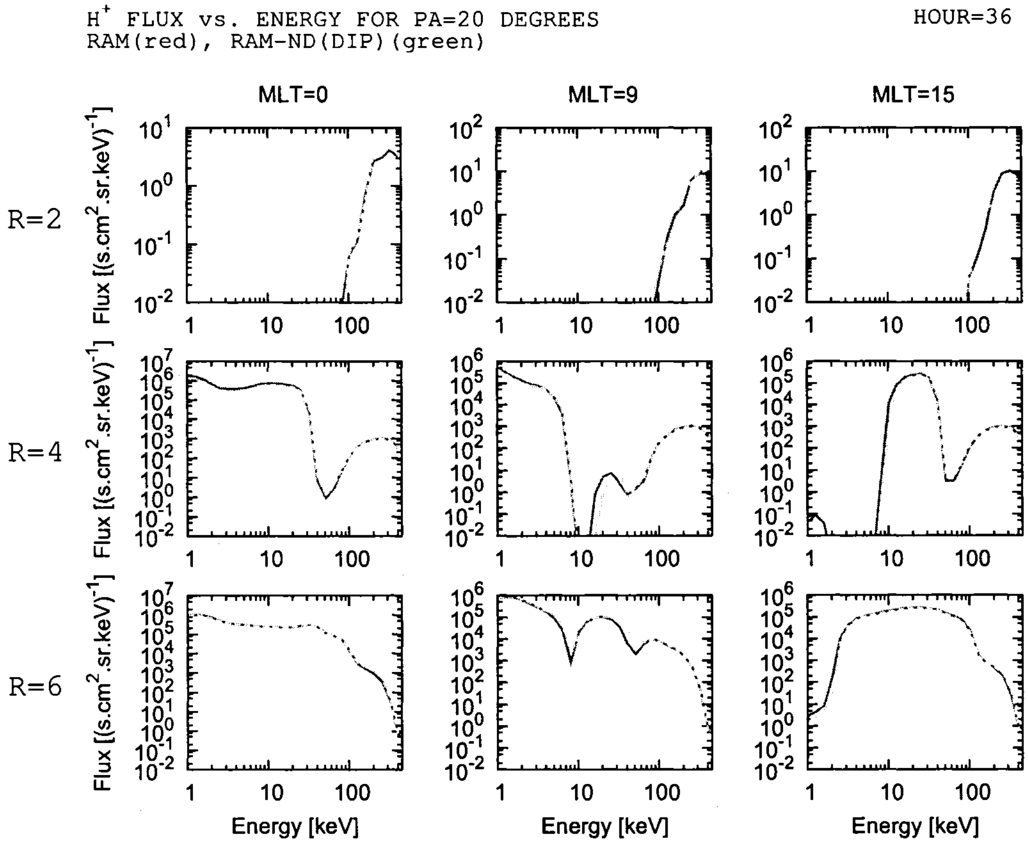

Figure 4-8: Trapped equatorial H$^+$ flux vs. energy for MLT=0, 9, 15, L=2, 4, 6, PA=20°, hour 36 after the beginning of the storm (DOY 2001:112 at 36:00 UT)

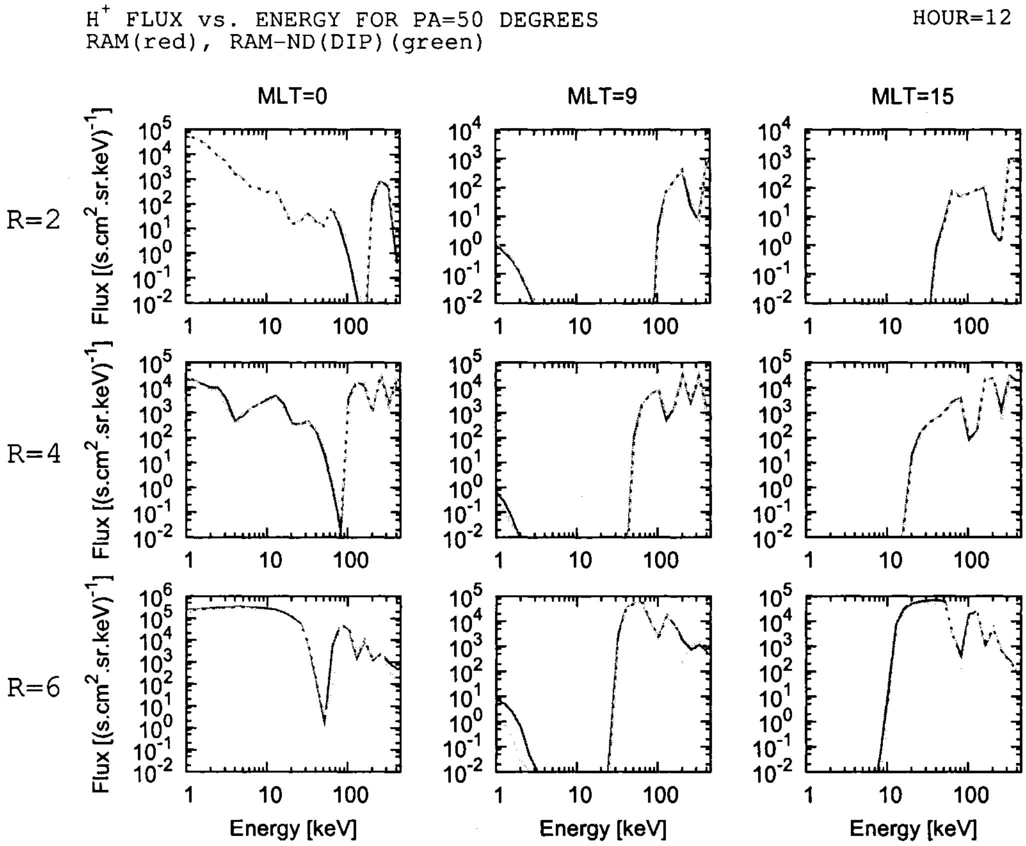

Figure 4-9: Trapped equatorial H^+ flux vs. energy for MLT=0, 9, 15, L=2, 4, 6, PA=50°, hour 12 after the beginning of the storm (DOY 2001:111 at 12:00 UT)

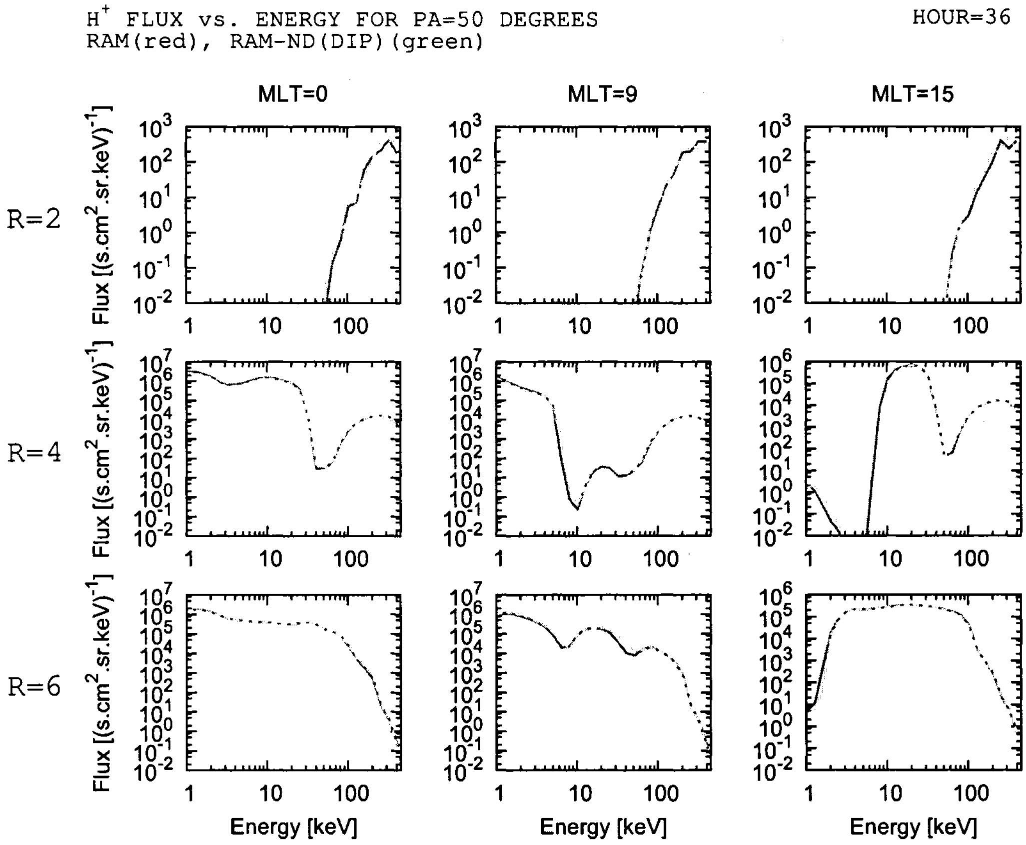

Figure 4-10: Trapped equatorial H^+ flux vs. energy for MLT=0, 9, 15, L=2, 4, 6, PA=50°, hour 36 after the beginning of the storm (DOY 2001:112 at 36:00 UT)

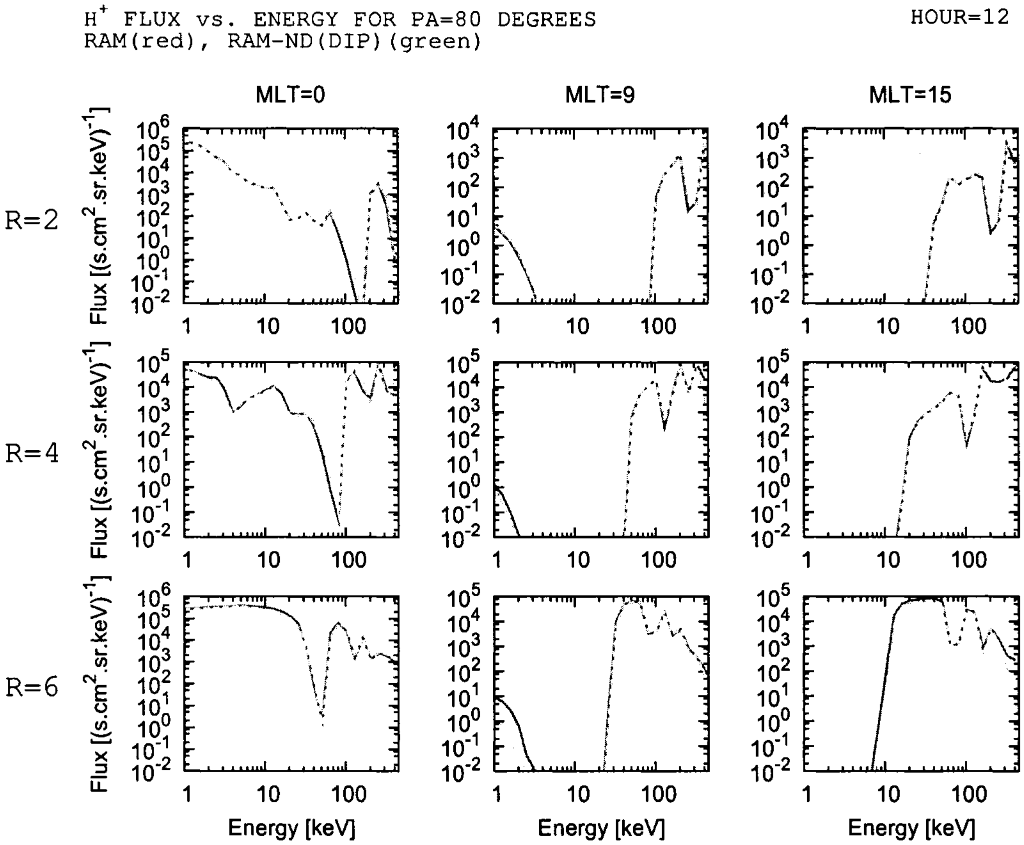

Figure 4-11: Trapped equatorial H^+ flux vs. energy for MLT=0, 9, 15, L=2, 4, 6, PA=80°, hour 12 after the beginning of the storm (DOY 2001:111 at 12:00 UT)

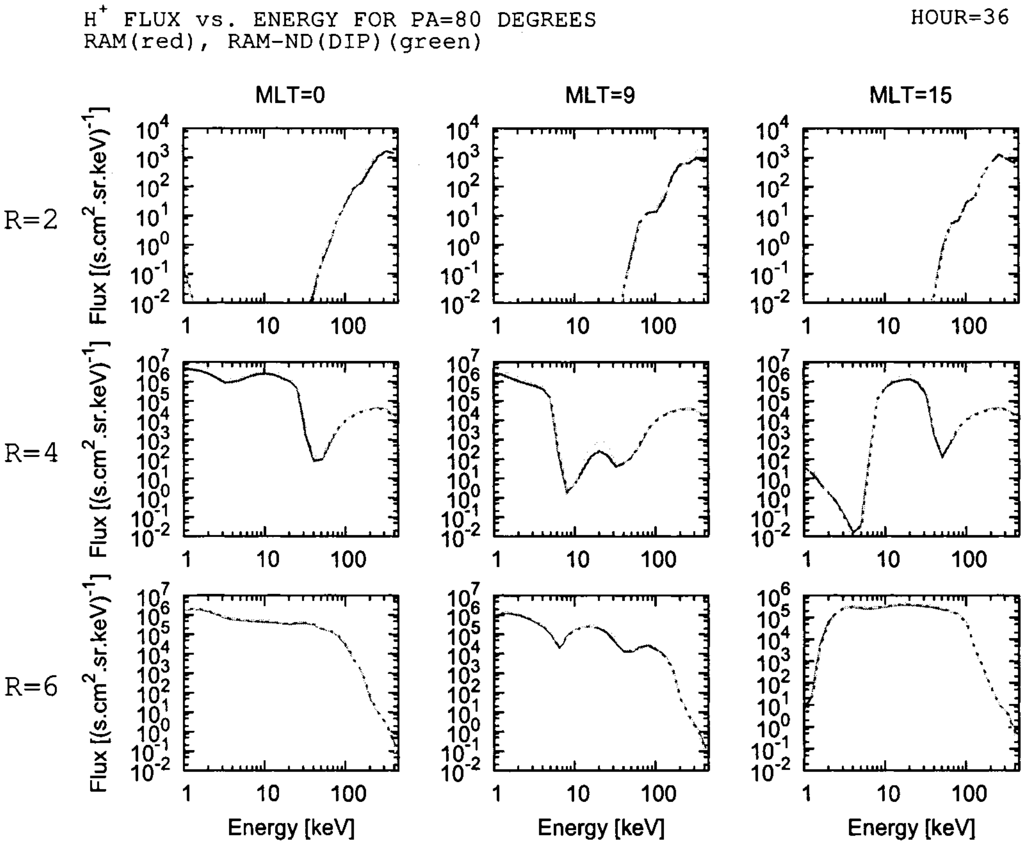

Figure 4-12: Trapped equatorial H$^+$ flux vs. energy for MLT=0, 9, 15, L=2, 4, 6, PA=80°, hour 36 after the beginning of the storm (DOY 2001:112 at 36:00 UT)

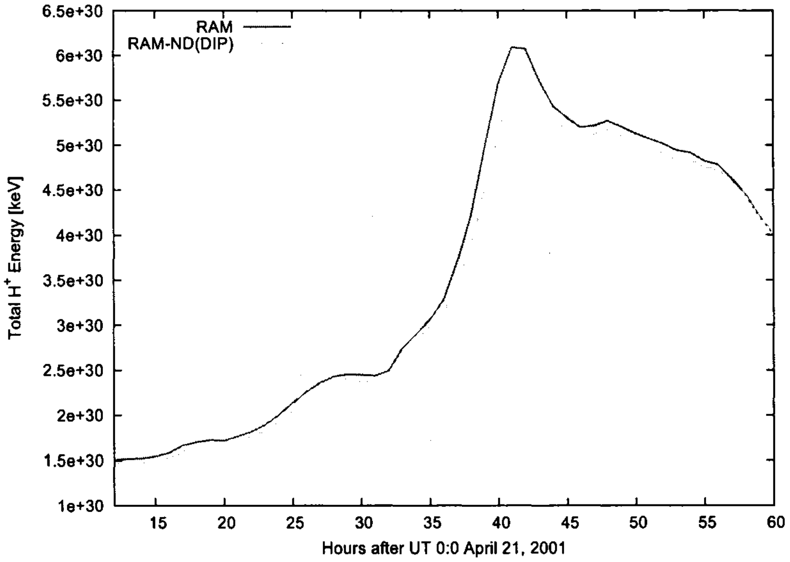

Figure 4-13: Total ring current H$^+$ energy vs. time for RAM (red) and RAM-ND (green) for a dipole field.

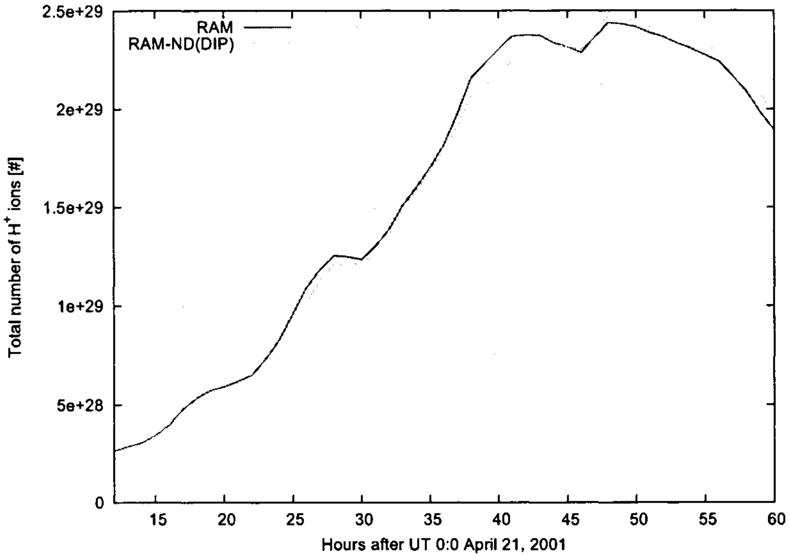

Figure 4-14: Total number of ring current H$^+$ ions vs. time for RAM (red) and RAM-ND (green) for a dipole field.

CHAPTER 5

MODEL RESULTS

In the present study we model the moderate storm of April 21, 2001 which was selected by the Inner Magnetosphere-Storm (IMS) campaign of the Geospace Environment Modeling (GEM) program at the National Science Foundation (NSF). In Section 5.1 we present the initial and boundary conditions for the RAM model [Jordanova et al., 2006] and the input data for the T04s magnetospheric field model. In Section 5.2 we present results for the bounce-averaged exospheric hydrogen densities and magnetic gradient-curvature drift velocities. The time evolution of the trapped equatorial flux is discussed in Section 5.3. In Section 5.4 we compare the modeled spin averaged fluxes with satellite observations. The total ring current energy and the total particle number for different ion species is discussed in Section 5.5. An approximate calculation of the stormtime *Dst* index is presented in Section 5.6.

5.1 Observations

5.1.1 Interplanetary Data

The hourly averaged solar wind plasma and interplanetary magnetic field data for the storm of April 21-23, 2001 obtained by the Advanced Composition Explorer (ACE) [McComas et al., 1998; Smith et al., 1998] are presented in Figure (5-1). A delay in the data of about 60 minutes accounts for the signal propagation towards Earth. An interplanetary shock was observed at hour ~ 16. After the shock the total magnetic field increased in magnitude, the solar wind velocity went up from ~ 350 to ~ 400 km/s, the dynamic pressure increased to about 6.5 nPa, and the proton density increased from ~ 5 to ~ 25 cm^{-3}. The IMF B_z reached a minimum of about -13 nT at hour 35. The magnetic fields were strong and smooth after hour 24 which was an indication of a magnetic cloud. The polar cap potential reached a maximum of about 140 kV at hour ~ 35 [Jordanova et al., 2006]. The magnetic cloud caused a moderate geomagnetic storm with $Dst = -102$ nT and $Kp = 6^+$ at hour ~ 40. The recovery phase lasted for more than ~ 30 hours.

5.1.2 Magnetospheric Data

The energetic particle observations from the Los Alamos National Laboratory (LANL) satellites at geosynchronous orbit provide realistic boundary conditions for the model. The Magnetospheric Plasma Analyzer (MPA) [McComas et al., 1993] (energy range 1eV-40keV), and the Synchronous Orbit Particle Analyzer (SOPA) [Belian et al., 1992] (energies >50 keV) on LANL satellites 080, 084, and 01A measured the ion fluxes during the April 21-23 storm period. These satellites were located at about 90° separation in longitude and provided very good coverage of the time-varying magnetospheric conditions at geosynchronous orbit. Interpolation at the boundaries is used when there is no satellite data available. The heavy ion composition at the nightside boundary is determined as a function of geomagnetic and solar activity according to Young et al. [1982]. The losses through the dayside magnetopause in the model correspond to a free outflow from the dayside boundary [Jordanova, 1995]. The contribution from direct injection of ionospheric ions is not considered in the model.

As initial conditions on the nightside we use the quiet time statistical data set from Sheldon and Hamilton [1993]. The authors studied the transport and loss of ions in the

Earth's quiet time ring current and constructed a data set with full local time coverage from measurements made by the AMPTE/CCE-CHEM instrument in near equatorial orbit at $2-9$ R$_E$; on the dayside (6 to 18 MLT) the initial ring current distributions are assumed zero.

5.1.3 Input data for T04s model

The input data for the T04s model are the dynamic pressure P_{dyn} (SWRP), Dst, IMF B_y, IMF B_z, and the six variables W1-W6. The W1-W6 parameters are prepared before the actual storm simulation (courtesy to N. Tsyganenko, GSFC). The interplanetary data necessary for the calculation are the IMF B_z in GSM coordinates, the alpha-to-proton ratio, the proton density and the solar wind velocity [Tsyganenko and Sitnov, 2005]. The hourly averaged input data are updated at every hour without interpolation at intermediate time steps (a step-like input update).

5.2 Bounce – Averaged Exospheric Hydrogen Density and Magnetic Gradient – Curvature Drift Velocity

To show the change in the bounce-averaged exospheric hydrogen density and bounce-averaged magnetic gradient curvature drift velocity in the time-varying T04s magnetic field we plot them at eight different times during the storm period. Table (5.1) shows the respective input parameters for the T04s model: Solar Wind Ram Pressure (P), the stormtime index Dst, the southward IMF B_y and B_z, and the variables W1-W6.

The relative difference $(B_0^{T04s}-B_0^{Dipole})/B_0^{Dipole}$ in the equatorial magnetic field between T04s and dipole is shown in Figure (5-2). The Sun is on the right hand side in all plots. For quiet time T04s field is smaller than the dipole filed on the midnight side and the difference reaches up to -25%. On the noon side the difference in the magnetic field is close to 0% for

DOY, UT	P [nPa]	Dst [nT]	B_y [nT]	B_z [nT]	**W1**	**W2**	**W3**	**W4**	**W5**	**W6**
111 11:30	1.34	4	-1.30	-1.50	0.16	0.23	0.02	0.10	0.30	0.39
112 00:30	7.14	29	1.80	7.90	0.19	0.25	0.06	0.15	0.18	0.91
112 10:30	2.51	-42	-9.60	-11.10	2.05	2.77	0.46	3.05	2.11	3.39
112 16:30	3.54	-101	0.80	-10.80	2.87	3.75	0.97	4.20	2.38	4.55
112 21:30	2.12	-72	4.60	-8.50	2.36	2.83	1.19	2.81	1.69	3.13
113 03:30	1.97	-69	1.30	-8.70	1.55	1.93	1.19	1.65	1.35	2.28
113 13:30	1.83	-40	6.00	0.20	0.57	0.41	1.12	0.37	0.10	0.43
114 00:30	1.10	-16	6.40	3.10	0.02	0.00	0.80	0.00	0.00	0.00

Table 5.1: Input parameters for the T04s model at eight different times during the April 21-24, 2001 storm: Solar Wind Ram Pressure (P), the stormtime index Dst, the southward IMF B_y and B_z, W1, W2, W3, W4, W5, W6.

the most part in the inner region and it becomes about 10% close to the outer boundary of 6.5 R_E. Close to the inner boundary of 2 R_E at dusk-noon the dipole field is smaller than the T04s field with difference of about 10%. The more disturbed the magnetospheric conditions become, the bigger the difference is between the T04s and dipole. At the peak of the storm (DOY 112 at 15:30 UT) the difference reaches more than -85% on the dusk-midnight side (peak located around 5.5 R_E) and about -30% on the noon-dawn side (peak located around 5.0 R_E). These differences result from the geomagnetic field deformation related to the dynamic current system in the case of the T04s empirical model [e.g. *Tsyganenko and Sitnov*, 2005]. During the recovery phase (DOY 113 at 02:30 UT to DOY 114 at 00:30 UT) the T04s field configuration becomes more "dipolar" and the relative difference gradually decreases.

The relative differences $\left(\langle H_{Dens}\rangle^{T04s} - \langle H_{Dens}\rangle^{Dipole}\right) / \langle H_{Dens}\rangle^{Dipole}$ in the bounce-averaged hydrogen densities $\langle H_{Dens}\rangle$ for equatorial pitch angle 35° are shown in Figure (5-3). The quiet time values (first plot) calculated for the T04s field are smaller on the midnight side with a difference of about -5% at $\sim$ 6 R_E and about 0% at 2 R_E and 5% towards the noon side at 6.5 R_E. For disturbed conditions (DOY 112 at 09:30 UT to DOY

113 at 02:30 UT) there is a sharp transition in the relative difference towards dusk-midnight (around 4 R_E) and the hydrogen densities for the T04s field become smaller with about -30% than those for dipole magnetic field at the peak of the storm (DOY 112 at 15:30 UT). The relative difference stays around the -5% value in the region between 2 R_E and 4 R_E. Towards the end of the recovery phase (DOY 114 at 00:30 UT) the bounce-averaged hydrogen density for T04s does not differ much from the one for a dipole field.

When the magnetosphere is compressed by the solar wind on the noon side the magnetic field lines move closer to Earth. In this case we integrate through a region with higher hydrogen density and $\langle H_{Dens} \rangle$ for the T04s model is bigger than the one for a dipole field. On the midnight side the field lines stretch farther from Earth and the integration happens in a region with less hydrogen and in this case the bounce-averaged density is smaller than the one for a dipole field. These results are important for the calculation of charge exchange losses in the terrestrial ring current [e.g. Sheldon and Hamilton, 1993; Jordanova et al., 1994; Fok et al., 1995, 1996].

Figure (5-4) shows the relative differences in the bounce-averaged magnetic gradient-curvature drift velocities for equatorial pitch angle 35°. The top left panel shows the relative difference between $\langle \mathbf{V}_B \rangle$ in (3.11) for T04s model and for dipole field for quiet time (prestorm) conditions. The energy of the particles is 100 keV. For quiet time the difference varies between 20% on the nightside and -20% on the dayside. For stormtime geomagnetic field configuration (DOY 112 at 09:30 UT to DOY 113 at 02:30 UT) the difference increases and at the storm peak it is respectively between $\sim$ 200% (midnight-dusk) and about -10% to -20% (dawn-noon); differences over 250% are seen in an isolated region at magnetic local times $\sim$ 17 to 21 and L $\sim$ 5.5 to 6.5. Differences between 100% and 200% in the bounce-averaged drifts are mostly located in the region between 4 and 5.5 R_E towards midnight for MLT $\sim$ 15 to 04 where the partial ring current is observed. During the recovery phase the difference decreases gradually and towards the end of the storm (DOY 114 at 00:30 UT) is similar to the one for prestorm conditions (quiet time). We find that the contribution of $\langle \mathbf{V}_R \rangle$ in equation 3.18 is around $\sim$ 5% at places where the bounce-averaged gradient-curvature velocity is highest and less than 5% everywhere else [Vapirev and Jordanova, 2007]. This result shows that the calculation of only $\langle \mathbf{V}_B \rangle$ in equation 3.18 is a good approximation when modeling the magnetic gradient-curvature drifts of charged particles in the inner magnetosphere.

Equation (3.11) shows that when the T04s model field decreases compared to a dipole (Figure 5-2), the gradient-curvature velocity $\mathbf{V}_B$ becomes much bigger than the one in the dipole case. The realistic magnetic field geometry results in higher field gradients especially on the dusk-midnight side (L $>$ 4) where the field lines become significantly stretched and twisted. The high gradients together with the strong magnetic field dependency yield much bigger bounce-averaged magnetic gradient-curvature drifts than the corresponding ones for a dipole field.

5.3 Time Evolution of the Trapped Equatorial Flux

The equatorial H^+ flux as a function of the particle energy at hour 40 for pitch angles 50° and 80° is plotted in Figure (5-5) and Figure (5-6) respectively. The presented results are for RAM (red) and RAM-ND (green) for MLT=0, 9, 15 and L=2, 4, 6. For both pitch angles and L=2 the two models give similar results because close to Earth the magnetic field still resembles a dipole during moderate storms. At L=2 the bounce-averaged hydrogen density has similar values for both T04s and dipole which suggests that the charge exchange loss rate is the same for both models. The difference is at MLT=0 for very low flux values ($\sim 10^{-1}$) where RAM-ND gives a higher flux at energy $\sim$ 35 keV for PA=50° and energy $\sim$ 25 keV for PA=80°.

At L=4, MLT=0, 15 both plots show that the RAM-ND flux has a stagnation dip slightly shifted towards smaller energies. At L=4, MLT=9 for both pitch angles RAM-ND gives higher flux than RAM and for PA=80° the stagnation dip is shifted towards smaller energy. At L=4 the T04s bounce-averaged hydrogen density becomes smaller which suggests that the smaller charge exchange rate would be responsible for a higher flux at MLT=15. The bounce-averaged velocity for T04s, however, is higher with about 50% giving higher azimuthal drifts and shifting the dip towards smaller energy. Low energy particles drift eastward and high energy particles drift westward. Ions with certain energies experience similar in magnitude eastward and westward drifts and this results in a very slow drift velocity. The dip in the energy spectra corresponds to particles which have either not reached the observation point, or have experienced significant losses during their slow drift towards the observation point. Higher azimuthal particle drifts (higher bounce-averaged magnetic gradient-curvature drift velocity) for the T04s model means that the high energy particles move faster in the T04s field and the high energy flux increases faster on the prenoon side which explaines the overall shift of the RAM-ND flux profiles towards smaller energies in comparision with the RAM flux at a certain time (hour 40).

The fluxes for PA=50° and PA=80°, L=6, MLT=0, 9, 15 are similar for both models with slightly smaller values for RAM-ND at higher energies. For PA=80°, L=6, MLT=9 RAM-ND gives higher flux in the range $\sim 10-20$ keV, while the RAM flux has a profound dip in the curve. The shift of the stagnation dip at L=6, MLT=9, PA=50° for RAM-ND is due to the higher azimuthal particle drifts. The azimuthal drift is proportional to the pitch angle - the higher the pitch angle, the higher the drift for a westward moving particles and vice versa for an eastward drift. This explains the additional stagnation dip shift towards lower energies for larger pitch angles, more clearly expressed for RAM-ND than for RAM. The "flattened" flux profile for PA=80° at L=6, MLT=9 is due to the stronger pitch angle dependency of the azimuthal drift for T04s field in combination with smaller bounce-averaged exospheric density (less ion losses) at larger L-shells.

Figure (5-7) and Figure (5-8) show the equatorial He^+ flux as a function of the particle energy for pitch angles 50° and 80° respectively. At L=2, MLT=0, PA=50° the flux for both RAM and RAM-ND models is the same. The RAM-ND fluxes for MLT=9, 15 are slightly higher in the lower energy range than those for RAM. For L=2, PA=80° the RAM-ND flux significantly differs from the RAM flux in the energy range $\sim 5 - 50$ keV for MLT=0, 9 and it is higher at low energies for MLT=15. At L=4 on both plots RAM-ND flux is slightly shifted towards the lower energies for MLT=0, 15 and it has higher values around $\sim 10 - 50$ keV. At L=6, MLT=0, 9, 15 the RAM-ND gives lower flux than RAM for energies > 100 keV. At MLT=9 for PA=80° the RAM-ND flux is higher around $\sim 10 - 20$ keV. At L=2, MLT=0, 9, 15 and MLT=9, L=2, 4, 6 the He^+ ions with low and medium range energies show higher flux for RAM-ND than for RAM. The RAM model provides a reasonably accurate calculation of the trapped equatorial flux for PA=50°, but its dipole field approximation differs significantly (order of $\sim 10^2$) from the RAM-ND flux at L=2 and MLT=9 for PA=80° at energies $\sim 3 - 20$ keV. At large L-shells the RAM-ND flux is smaller for energies > 100 keV than the RAM flux. The pitch angle anisotropy is more expressed for the non-dipole field configuration.

The O^+ equatorial flux for PA=50°, 80° is shown in Figures (5-9) and (5-10) respectively. For MLT=0 the RAM-ND flux follows closely the RAM flux for energies up to ~ 100 keV. At L=2, PA=50° the RAM-ND flux shows that practically no oxygen ions are present at the postnoon side (MLT=15). For PA=80, MLT=9, L=4, 6 the stagnation dip of the RAM-ND flux profile is shifted towards lower energy (~ 6 keV) again due to higher azimuthal drifts for westward moving particles (high energy range). At MLT=9 for both pitch angles the RAM-ND model shows lower flux values at L=2 and at L=4 the low-to-medium range particles dominate over the RAM O^+ flux. At L=4, 6 the stagnation dip again moves towards lower energy because due to the higher drifts for the T04s field more high energy oxygen reaches the prenoon side. The losses at higher energies are bigger for O^+ then those for He^+ because of the bigger charge exchange cross-sections for oxygen ions. This is clearly seen at L=2, 4. At L=6 both RAM and RAM-ND models give similar fluxes with those for RAM-ND being slightly smaller at high energies.

Figures (5-11) and (5-12) show the distribution of the H^+ flux for dipole (RAM) and T04s (RAM-ND) field in the equatorial plane in SM coordinates. First two rows show the flux at 10 keV (PA=50°, 80°) and rows 3 and 4 show the flux at 100 keV (PA=50°, 80°). Each row presents the equatorial flux at three different times: DOY 111 at 22:00 UT (before the storm main phase, Dst=12 nT), DOY 112 at 15:00 UT (storm peak, Dst=-102 nT), and DOY 113 at 2:00 UT (recovery phase, Dst=-74 nT).

For low energy (10 keV) at DOY 111 at 22:00 UT the RAM-ND flux is higher at the midnight-dusk side than the RAM flux. For PA=80° both models calculate similar flux values, while for PA=50° the RAM-ND flux is about 10 times higher and it is more localized between MLT 12 and 4. The second column (DOY 112 at 15:00 UT) shows similar fluxes for PA=50° but the difference between the two models becomes stronger for PA=80° where the RAM flux is more smoothly distributed between MLT 12 and 6, while the RAM-ND flux is slightly lower on the postnoon side close to the outer boundary of 6.5 R_E and higher around L=4 between MLT 17 and 6. The third column (DOY 113 at 2:00 UT) shows overall higher RAM-ND fluxes for both pitch angles with the flux for PA=80° more localized around L=4. Overall the low energy flux for a non-dipole field (RAM-ND) is higher than the one for a dipole (RAM). The higher fluxes in the midnight-dusk region are due to lower bounce-averaged exospheric hydrogen density, hence lower charge exchange rate, and the higher azimuthal drifts (bigger bounce-averaged magnetic gradient-curvature drifts) around midnight-dusk and $\sim 4 - 5.5$ R_E. The RAM-ND models shows that the low energy component of the proton ring current has higher contribution during the storm recovery phase. The RAM model gives stronger pitch angle anisotropy during the main and the recovery phase, while for the RAM-ND flux the low energy component extends over all pitch angles which reduces the anisotropy. The proton distribution in the equatorial plane is highly asymmetric for the whole duration of the storm.

The high energy (100 keV) component of the proton flux at DOY 111 at 22:00 UT is very much equal for both models (the RAM-ND flux is slightly higher) and the distribution is symmetric for all MLTs for both pitch angles. At DOY 112 at 15:00 UT RAM model shows that H^+ are mostly distributed between MLT 12 and 0 with a peak around MLT=17. The pitch angle anisotropy for RAM is not very strong. For PA=50° the RAM-ND model gives lower flux values with the proton distribution narrowly localized around L=6 and MLT 11 and 23. The RAM-ND proton flux distribution for PA=80°, however, has higher values for all MLTs with a peak around 4 R_E on the postnoon side and around 5.5 R_E at dawn. A strong pitch angle anisotropy in the particle distribution is observed when the T04s field is used. Higher azimuthal drift values for the westward moving high energy flux component make the high energy protons move faster and thus the number of particles in the ring current increases. The smaller bounce-averaged hydrogen density for T04s contributes also for the stronger distribution anisotropy. During the recovery phase (DOY 113 at 2:00 UT) for smaller pitch angles the RAM-ND flux is smaller than the RAM flux and it is very much homogeneous for all MLTs, while the RAM model shows a relatively symmetric distribution. The plots for PA=80° show much stronger and symmetric distribution for RAM-ND. The pitch angle anisotropy in the equatorial flux for RAM-ND is very distinctive and shows that for larger pitch angles the high energy protons can be dominant part of the ring current particle population. Because of the bigger azimuthal drifts for higher pitch angles and the lower bounce-averaged hydrogen density the fast moving protons, which also have smaller charge exchange cross-sections, continue to drift with less losses during the recovery phase of the storm. Thus, the high energy population given by the RAM-ND model remains trapped after the storm main phase (*Dst* minimum) while particles convected during main phase slow down (Figure 5-12), a result which has been recently observed by [Ganushkina et al., 2006] and by [Milillo et al., 2006].

The equatorial flux distribution of He^+ ions is shown in Figure (5-13) for RAM and in Figure (5-14) for RAM-ND model. The layout of the dial plots is the same as in the previous two figures.

The low energy component at DOY 111 at 22:00 UT has similar distribution for both models for both pitch angles with the RAM-ND flux being slightly lower for PA=50° around MLT 6 to 9. The RAM-ND flux is also slightly higher on the midnight-postnoon side. As the storm progresses (DOY 112 at 15:00 UT), the ion distribution for RAM develops stronger pitch angle anisotropy with flux peak at around $2.5 - 3$ R_E and MLT=3 for PA=50°, while the RAM-ND distribution has a strongly localized peak around 2.5 R_E between MLT 12 and 6 with similar distributions for both pitch angles. During the recovery phase (DOY 113 at 2:00 UT) RAM-ND shows that the low energy He^+ flux increases for all pitch angles, opposite to the results from RAM whose He^+ population remains almost the same.

For high energies both RAM-ND and RAM give similar He^+ distributions before the development of the storm main phase. The ions are symmetrically distributed beyond 4 R_E. There is a localized peak for very low flux values ($\sim 10^{-2}$) located around 2.5 R_E at midnight for RAM and around the noon-dusk side for RAM-ND. The storm main phase He^+ ion population develops a pitch angle anisotropy for the non-dipole magnetic field. Due to higher azimuthal drifts more westward drifting particles fill the space on the dusk side and reach the prenoon side for large pitch angles [e.g., Fok et al., 1995]. The RAM-

ND distribution for PA=50° shows overall smaller flux for all MLTs than the RAM model. During the recovery phase the again the RAM-ND model shows a more distinctive pitch angle anisotropy for the He^+ flux. The particles are symmetrically distributed for all MLTs while the RAM model give higher fluxes on the dusk side for both pitch angles. The PA=50° plot shows smaller flux for RAM-ND and the PA=80° shows much higher He^+ flux with a peak around 4.5 R_E. The high energy flux computations for particles mirroring close to the equatorial plane (large pitch angles) by the RAM-ND model are consistent with previous ring current observations [Daglis et al., 1993].

The O^+ flux distribution is presented in Figures (5-15) and (5-16) for dipole and non-dipole magnetic field respectively. Again the plot layout is the same as in the previous figures for H^+ and He^+ fluxes.

The low energy component has very similar distributions for both models and pitch angles with the fluxes for RAM-ND being a little higher than those for RAM. The RAM-ND model simulation shows that for both PA=50° and PA=80° the O^+ ion flux steadily intensifies during the storm main and recovery phases all over the equatorial plane.

For the 100 keV energy bin RAM-ND has the same particle distribution at DOY 111 at 22:00 UT as the RAM model. During the storm main phase the RAM-ND O^+ flux develops stronger pitch angle anisotropy. For Pa=50° RAM-ND gives flux which is well localized beyond the ~ 4 R_E boundary with a peak at dusk and which is smaller than the flux calculated by RAM, extending to lower L-shells. The distribution for PA=80° for RAM is almost the same as in the PA=50° case while the RAM-ND calculations show a steady flux for all MLTs due to higher azimuthal drifts. The lower boundary is around the 3.5 R_E and the peak is at MLT=18 around 4.5 R_E. During the recovery phase the energetic O^+ significantly decreases for both models. The RAM-ND flux has a strong pitch angle anisotropy. For smaller pitch angles the flux is localized beyond $\sim 4.5 - 5$ R_E while the RAM model flux extends also for low L-shells. The PA=80° flux distribution shows a steady symmetric flux with peak ~ 4 R$_E$ for RAM-ND while the RAM flux peaks at larger radial distances and has a defined asymmetry towards the postnoon side.

Energetic O^+ enhancements usually have short lifetimes, because of the localized and sporadic character of ionospheric outflow [e.g. Strangeway and Johnson, 1983]. The charge exchange cross-sections for oxygen ions are relatively high (compared to those for hydrogen and helium ions) which results in relatively short lifetimes of energetic O^+. The 100 keV O^+ ions have lifetimes of about 33, 22, and 11 hours at L$\sim$5.0, 4.25, and 3.5 respectively [Smith et al., 1981]. Therefore the prolonged enhancement of O^+ in the RAM-ND simulation is due to the lower charge exchange losses for T04s field during the storm main phase. Moreover, because of the higher bounce-averaged magnetic gradient-curvature drifts (higher azimuthal drift for larger pitch angles at high energies) and smaller exospheric hydrogen density the energetic oxygen ions in the T04s field move faster and experience less collisions with the cold exosphere. Overall, the RAM-ND model calculates an O^+ flux with a maximum around $3-5$ R$_E$ during storm main and recovery phases which has been previously observed by the AMPTE mission [Hamilton et al., 1988], while the RAM model flux distribution represents the satellite measurements at these altitudes with less accuracy especially for the energetic O^+ component where its peak is for L-shells greater than 5 R$_E$. The flux at the outer L-shells $(5-7)$ measured by the AMPTE mission was reported to be much smaller which is consistent with the RAM-ND calculation.

During the flux calculations in our model two assumptions have been made. First, we consider that all particles are adiabatic, namely, there is no violation of the frozen-in condition for the plasma ions due to magnetic mirror instabilities accounting for finite ion Larmor radius (FLR) effects. The particles' behavior can be characterized by the *kappa* parameter, which is given by $\kappa = \sqrt{R_c/\rho_L}$ where R_c is the field line radius of curvature and ρ_L is the Larmor radius [Büchner and Zeleny, 1986]. Particles with $\kappa < 1$ are always nonadiabatic but have quasi-regular dynamics, while particles with $1 < \kappa < 2$ are nonadiabatic and also experience chaotic scattering. Particles with $2 < \kappa < 3$ are in a transition from chaotic to regular adiabatic behavior [Büchner and Zelenyi, 1989]. The gyroradius of the heavy ions (O^+) in the magnetosphere in reality can reach quite large values. The shape of the field lines at *Dst* minimum is presented in Figure (5-17). The field lines are ploted for MLT=9 and MLT=21. The strongest distortion of the magnetic field lines occurs at MLT=21 and there the radius of the line curvature is around 2 R_E. For a 100 keV and a 400 keV O^+ the maximum values of the gyroradius are $\sim$ 3000 km and $\sim$ 6000 km respectively. The corresponding κ values are then $\sim$ 1.45 and $\sim$ 2.05. Non-adiabatically accelerated ions can execute Speiser orbits [Speiser, 1965] and can be ejected along the magnetic field into the plasmasheet boundary layer which can result in magnetospheric convection instabilities in the plasmasheet [e.g., Ashour-Abdalla et al., 1992; Kozlovsky and Lyatsky, 1999]. Since most of the ring current particles are within the 20 – 80 keV energy range, in the present geomagnetic storm simulation with RAM-ND such effects are not included.

The second assumption is that the loss cone for the T04s geomagnetic field does not change with respect to time and MLT and therefore it is considered equal to the loss cone in the dipole field approximation. Figure (5-18) presents the loss cone values for a dipole and T04s field and the difference between the two cases at *Dst* minimum. The first plot shows the loss cone for the dipole approximation, the second plot shows the loss cone in the case of a T04s field, and the third plot presents the loss cone difference $\left(\alpha_{LC}^{T04s} - \alpha_{LC}^{Dipole}\right)$ in degrees between the two fields. The T04s loss cone is larger than the dipole one at MLT=3 with a maximum difference of $\sim 5°$ at the lower boundary and no more than $\sim 1°$ everywhere else. Thus, for a moderate storm simulation the use of a loss cone for the dipole field approximations is assumed.

5.4 Spin Averaged Flux

The energy spectra of the spin averaged ion flux measured by Magnetospheric Ion Composition Spectrometer (MICS), a part of the Charge and Mass Magnetospheric Ion Composition Experiment (CAMMICE) on board the Polar satellite [Wilken et al., 1992] on April 22, 2001 is presented in Figure (5-19). The CAMMICE-MICS instrument is a one-dimensional time-of-flight electrostatic analyzer with post acceleration measuring the ions with an energy/charge of 1 to 220 keV/e with very good angular resolution. The MICS, mounted perpendicular to the spin axis, is able to obtain a two-dimensional distribution at one energy per charge during each 6-second spin period. A complete energy spectrum is obtained in 32 spin periods. The top plot shows the double coincidence response (DCR) H^+ flux, followed by the plots for H^+, He^+, and $O^{<+3}$ ion fluxes respectively (courtesy to R. Friedel, LANL). The data for the selected period is very scarce. There were only eighteen times when measurements were taken between L=2 and L=6.5. Six of these locations were between L=2.28-6.32 and MLT=21.31-21.94 at UT 5:49-6:05, five measurements were taken at L=2-6.19 and MLT=23.06-0.31 at UT 6:24-6:37, and seven measurements were taken at L=6.49-6.5 and MLT=9.56-9.67 at UT 8:29-8:47. To compare the satellite data with the model results, we consider energy spectra within the MLT=21.31-21.94 interval where the depression of the magnetic field is the strongest and the ion fluxes have highest values. Another interesting location is around MLT=9-10 where the magnetic field lines are strongly compressed by the solar wind towards the Earth and there is a minimum in the flux. Because the measurements taken within the MLT=9.56-9.67 interval are actually over the same L-shell, only one energy spectrum is selected for comparison with the model calculations. The model results from both RAM and RAM-ND have been interpolated according to L, MLT and time in order to match the spatial grid locations and the respective times of the measured energy spectra.

Figure (5-20) shows the spin averaged H^+ flux at six different times, L, and MLT. The first five plots present the flux at MLT=21.37-21.94 and UT 05:50-06:01 on April 22, 2001 at L=5.8, 4.53, 3.6, 2.91, 2.56 respectively. Because the five magnetic local times are almost the same and the measurements are within a short (12 minutes) time interval, these five plots actually represent the fluxes as a function of the L-shell. The magnetic latitude (MLAT) in degrees of the spacecraft is presented in each plot. The dip in the spectra moves towards lower energy with the decrease of the L-value. In general, the dip in RAM-ND/RAM flux is at slightly higher energies than the dip in measured data. The flux at L=5.8 for both models follows a similar profile as the data but the modeled values are $\sim 1-2$ orders of magnitude higher than the measurements. At energies $> 20-30$ keV RAM-ND shows lower flux profile than RAM. At L=4.53 the modeled spin averaged fluxes have better agreement with the data up to energies $<$ 100 kev and after that the data profile has lower values. The position of the dip in the spectrum is well predicted by both models at $\sim$ 50 keV. The L=3.6 fluxes have similar shape of the profiles for both data and models but the modeled fluxes are shifted with about $\sim$ 25 keV towards higher energy. The dip in the data is around 15 keV and both models predict a dip at around 40 keV. The modeled fluxes at L=2.91 for both RAM-ND and RAM differ from the data both in shape of the profile and in magnitude. The most significant difference occurs for energies below $\sim$ 20 keV where the data flux remains relatively constant and the models show a strong depression in the profiles with the RAM-ND flux being higher ($\sim 1-3$ orders of magnitude) than the RAM flux. The dip in the data is located at around $\sim$ 15 keV and the calculated fluxes seem to be shifted towards higher energies with $\sim$ 10 keV. Similar is the picture at L=2.56 where the RAM-ND/RAM flux describes the data relatively well within the $\sim 60 - 200$ keV energy range. For energies below ~ 60 keV the data flux is $\sim 5 - 6$ orders of magnitude higher than the predicted one. The bottom plot in Figure (5-20) shows the H^+ flux at L=6.5, MLT=9.57 at 08:30 UT. The position of the dip in the spectra is well predicted by both models (with difference $\sim 1 - 3$ keV higher). The overall modeled flux profile follows the data relatively well except at the dip where the data shows about 2 orders of magnitude lower flux than the models. In all the cases when the data was taken Polar was far from the equatorial plane.

Figure (5-21) shows the spin averaged He^+ flux at only three different times, L, and MLT because data is unavailable or is very little during the selected storm period. At L=5.8, MLT=21.37 the data flux profile is $\sim 1 - 3$ orders of magnitude smaller than the modeled flux. RAM-ND gives about ten times higher flux values than RAM at energies < 200 keV. At L=4.53, MLT=21.54 the RAM flux has a dip around 100 keV and RAM-ND around 65 keV, which is closer to the dip in the data (~ 50 keV). In the range $\sim 15 - 100$ keV RAM-ND has lower flux values which is closer to the measured one in the $\sim 15 - 50$ keV energy range than the RAM flux values. At L=6.5 and MLT=9.57 (bottom plot) both models give similar fluxes (RAM-ND flux being slightly lower) which are about ten times higher than the observed one.

Figure (5-22) shows the spin averaged O^+ flux at three different times, L, and MLT. The data from Polar are combined for O^+ and O^{++} ions. Again there are fewer plots because of missing data. At L=5.8, MLT=21.37 the modeled flux does not cover the data very well. Although the RAM-ND flux is slightly closer to the measured values, still it is about two orders of magnitude higher than the measurements. At L=4.53, MLT=21.54 both models describe relatively well the data around energies $\sim 15 - 50$ keV where the RAM-ND flux profile is lower than the RAM flux and closer to the data. At energies > 50 keV both models predict a sharp drop in the flux, while the slope in the data is very small. Finally, the modeled fluxes at L=6.5, MLT=9.57 show good comparison with the data. Again the RAM-ND flux shows slightly better agreement with the measured flux within the $\sim 10-100$ keV energy range.

The plots for the spin averaged ion flux show that changing the magnetic field model is not enough in order to have a good prediction of the ring current behavior. The large discrepancy at lower L-shells (lower energies) is probably due to the use of a Volland-Stern electric field [e.g., Kistler and Larson, 2000; Jordanova et al., 2001c; Angelopoulos et al., 2002]. The statistical study by Angelopoulos et al. [2002] of different electric field models in the near-Earth magnetosphere showed that the Volland-Stern model correctly describes the minimum in the flux profile in terms of L-shell dependence, but the energy of the dip differs than the energy of the minimum given by satellite measurements. Particles of energies $10-20$ keV travel to low L-shells at dusk because under a steady electric field those energies correspond to open trajectories and are constantly replenished with particles from the tail (nightside boundary conditions in RAM-ND). Lower energies correspond to $\mathbf{E} \times \mathbf{B}$-drift dominated closed trajectories and higher energies correspond to gradient-curvature drift dominated closed trajectories, which are both inaccessible by ions from the tail. Particles residing longer in such closed trajectories are subject to losses (e.g, charge exchange) which results in ion flux depletion at those energies. The Volland-Stern model does not allow low energy particle populations to be replenished enough by ions coming from the nightside. This allows the low energy flux to deplete and form a deep and broad minimum in the energy spectra at low L-shells [Angelopoulos et al., 2002]. The poor spatial and temporal resolution of this electric field model also contributes to the difference in the ion fluxes [Jordanova et al., 2001c]. The difference in the fluxes at larger L-shells could be due to the fact that Polar was not near the equatorial plane when the measurements were taken. The closest it gets to the equator is at MLAT around $-27°$. RAM and RAM-ND calculate the equatorial ion flux including all pitch angles outside the loss cone. Most of the ring current particles mirror close to the equator. When Polar is far from the equator it does not measure equatorially mirroring particles, thus missing a large part of the ring current particle population. This results in smaller measured fluxes than the modeled ones.

5.5 Total Ring Current Energy

The total ring current energy during the studied period is presented in Figure (5-23) and the total number particles is presented in Figure (5-24) for the three different ion species (H^+, He^+, O^+). RAM-ND gives smaller total energy for H^+ ions than RAM which is consistent with recent results for the same storm period from Ganushkina et al. [2006] who used an empirical magnetic field model and from Jordanova et al. [2006] who used a self-consistently calculated magnetic field model. The total energy profile shows an increase during the *Dst* (SYM-H) decrease. The peak energy for RAM (dipole field) is about two times higher than the RAM-ND total energy. This is similar to the same ratio of about 1.6 – 1.7 obtained by Ganushkina et al. [2006]. The difference is due to the fact that they used a dipole field for the Earth's main field, whereas the RAM-ND model used the more realistic IGRF model field to represent the main field of the Earth (Volland-Stern convection electric field was used in both cases). Hamilton et al. [1988] (and later Daglis [1997]) showed that the O^+ contribution to the ring current was concurrent with the *Dst* profile during moderate to large geomagnetic storms (AMPTE, CRRES missions). A comparison between Figure (5-23) and Figure (5-1) for hours 45 – 60 shows that for RAM-ND the total O^+ contribution concurres well with the almost constant (on average) SYM-H (*Dst*) profile which shows the consistency of the RAM-ND computation with the observations. On the other hand, the RAM total energy for oxygen ions decreases more steeply during the same period.

Figure (5-24) shows that protons dominate the ring current with a considerable contribution from oxygen ions ($\sim 40-45\%$). The calculations by the RAM-ND model confirm the recent results suggested by several other models [Ganushkina et al., 2006; Milillo et al., 2006], showing a constant and slightly increasing proton flux after the main phase of the storm (minimum *Dst*). The total number of He^+ ions is about $4-5\%$ of the total ring current particle population for both models and is consistent with previous satellite observations (see Table 2.1). The total number of O^+ ions for RAM-ND stays relatively constant during hours $45-60$ of the recovery phase (slowly increasing until hour ~ 48). This result suggests that the various ionospheric sources remain active for several hours during stormtime and thus providing a greater ionosperic outflow of oxygen ions. The reduced charge exchange losses lead to the accumulation of energetic O^+ (see Figure 5-16) when a non-dipole field is used in our computations. These ions would otherwise be removed rather quickly from the ring current particle population [Daglis and Axford, 1996].

5.6 Dst Index Calculation

The calculated *Dst* index is presented in Figure (5-25). The measured *Dst* is plotted in red, *Dst* given by RAM and RAM-ND (dipole approximation) are in green and blue respectively, and *Dst* for RAM-ND is in purple. The last two plots with the notation "VS2" show the *Dst* computed by RAM-ND (dipole approximation) and RAM-ND with the index A in Equation (3.7) multiplied by two. The RAM-ND predicted change in the *Dst* index is around two times smaller than the one predicted by RAM. The RAM/RAM-ND model calculates the contribution to the *Dst* index only of the ring current neglecting the contribution from other current systems, hence the difference with the measured total *Dst* [e.g., Jordanova et al., 2003a,b]. In order to calculate the *Dst* we use Dressler-Parker-Sckopke relation given by Equation (3.37). This is an approximate calculation because

Equation (3.37) is for a dipole field and, as it has been shown in the previous sections, the magnetic field and the total ring current energy differs significantly for the T04s field. In general, the RAM-ND model yields much smaller *Dst* perturbation. The model does not reproduce well the *Dst* shape during the recovery phase which is possibly an error due to the approximated formula.

The small change in the *Dst* index (compared to the measured one) given by RAM-ND is because of several reasons. In general, the *Dst* is formed by all current systems in the magnetosphere: induced Earth currents, magnetopause currents, ring current, tail currents, and field-aligned currents. Only the tail current is considered to contribute 25 – 50% of the *Dst* perturbation [e.g., Alexeev et al., 1996; Ohtani et al., 2001; Liemohn, 2003]. Our calculation includes only contribution from the ring current which in the case of T04s field has smaller total energy than the one for the dipole field configuration. In addition, we used in this first simulation a *Kp*-dependent Volland-Stern convection electric field model. Ring current injection is larger, penetrating to lower L-shells, and the *Dst* index is significantly better reproduced when a higher spatial and temporal resolution electric field model is used [Jordanova et al., 2003b, 2006]. The two "VS2" plots in Figure (5-25) are given as an illustration of how much the change in the electric field can infulence the prediction of the *Dst*. Measurements using CRRES data imply that the actual electric field may be quite different from what the Volland-Stern model predicts [Wygant et al., 1998]. Kistler and Larson [2000] have found that the changes in the electric field make a much more significant difference in the computations than the changes in the magnetic field which in the inner magnetosphere are relatively small. In addition, the stormtime asymmetric ring current can generate intense electric fields in the subauroral ionospheric region (low latitudes) and in the near-Earth magnetosphere [Ridley and Liemohn, 2002]. Ridley and Liemohn [2002] found that a relationship exists between the total potential difference of these electric fields and the stormtime ring current contribution to the *Dst* index. Such electric fields can actually become comparable or even stronger than the corrotation electric field in these regions and this could significantly slow down or reverse the eastward particle drift. Using a more realistic electric field will be considered in future extensions of this work. RAM-ND does not include the relative contribution of electrons to the stormtime total ring current energy content. Liu et al. [2005] show that electrons with energies of $1 - 50$ keV contribute the most to the stormtime electron energy content (e.g., at L = 4, $1 - 50$ keV electrons contribute 93% of all electrons in energy range of $1-400$ keV). The authors use the Explorer 45 data [e.g., Lyons and Williams, 1975, 1976; Lyons, 1976] to estimate that ring current electrons in may contribute $7.5 - 19\%$ as much energy content as ring current protons. The recent study of Jordanova and Miyoshi [2005] shows that the electron contribution to the ring current is highly variable and may contribute $\sim 2 - 10\%$ during a storm.

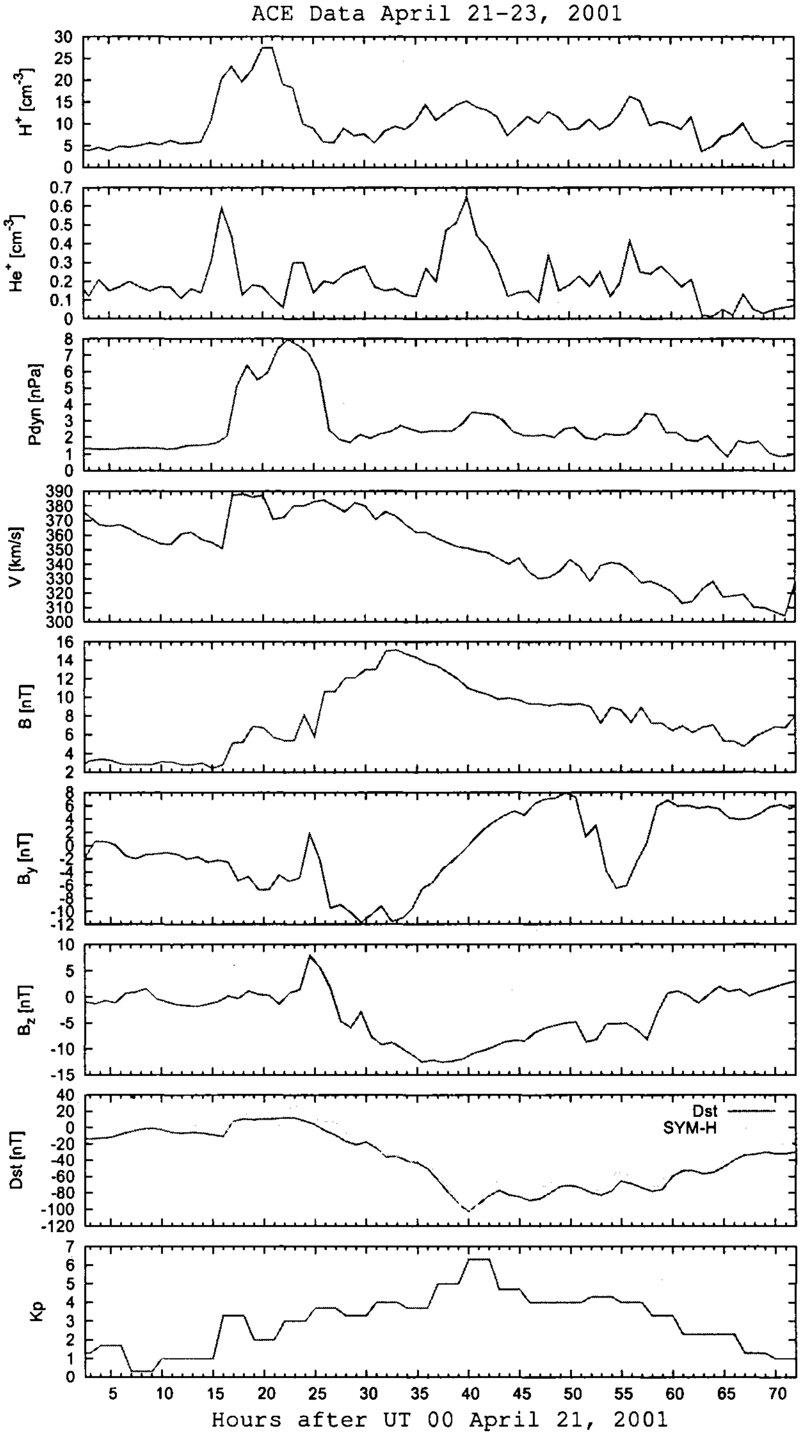

Figure 5-1: Interplanetary and magnetospheric data for the storm of April 21, 2001. From top: solar wind proton density, solar wind alpha particles density, solar wind dynamic pressure, solar wind velocity, magnetic field magnitude B, IMF B_y and B_z, Dst and SYM-H indices (courtesy to N. Tsyganenko, GSFC), Kp index.

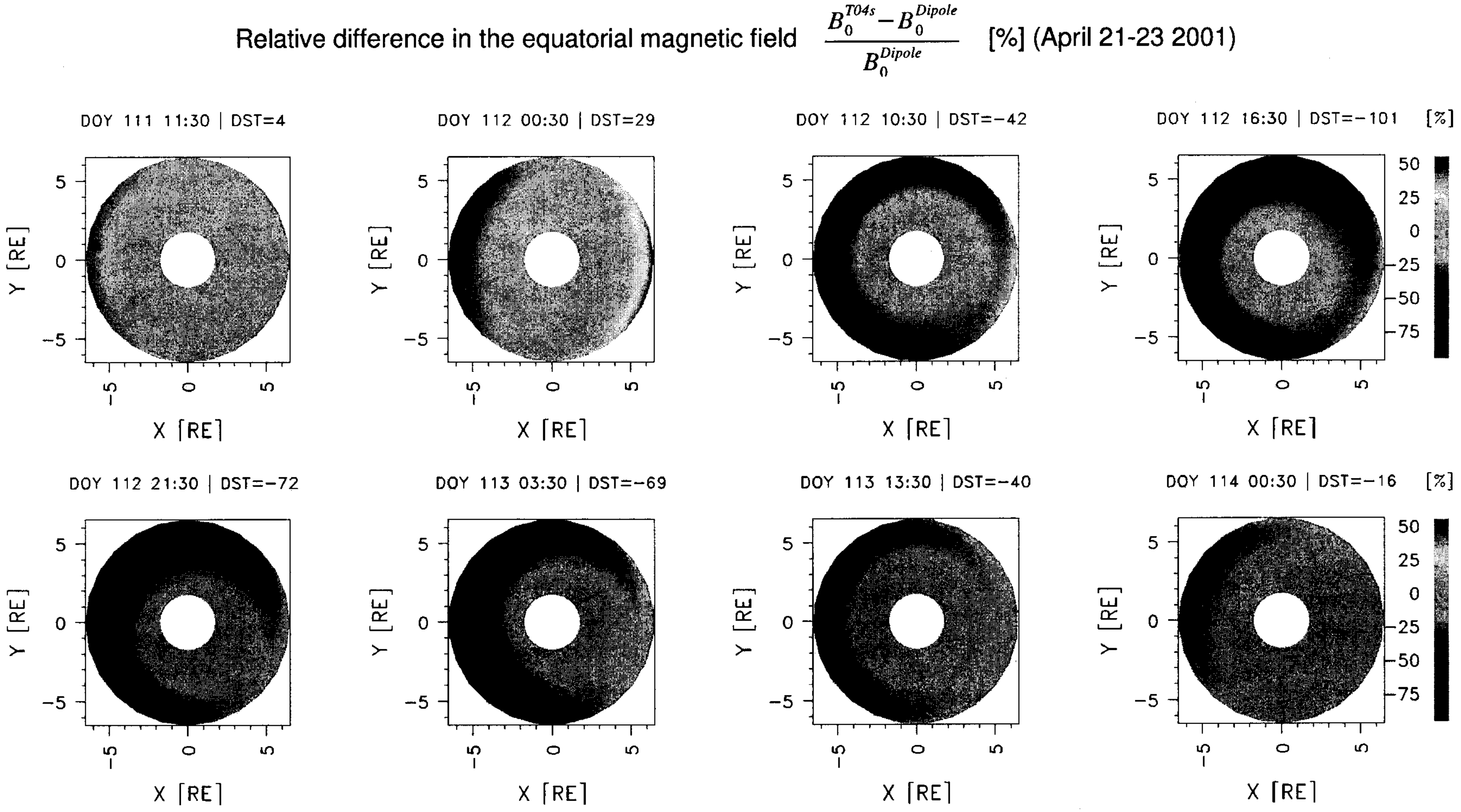

Relative difference in the equatorial magnetic field $\frac{B_0^{T04s} - B_0^{Dipole}}{B_0^{Dipole}}$ [%] (April 21-23 2001)

Figure 5-2: Relative difference in the equatorial magnetic field at eight different times. The Sun is on the right.

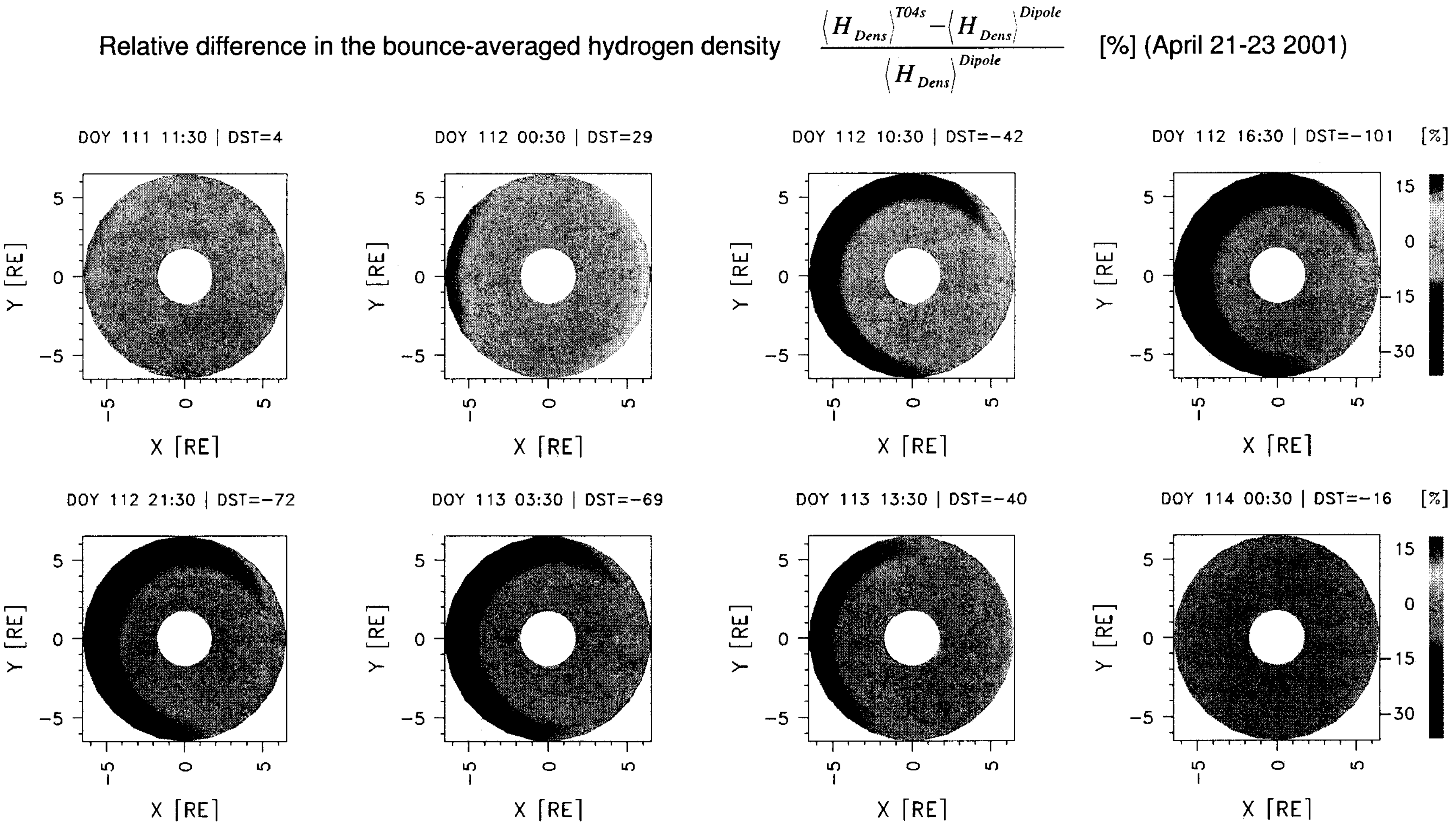

Figure 5-3: Relative difference in the bounce-averaged exospheric hydrogen density at eight different times. The Sun is on the right.

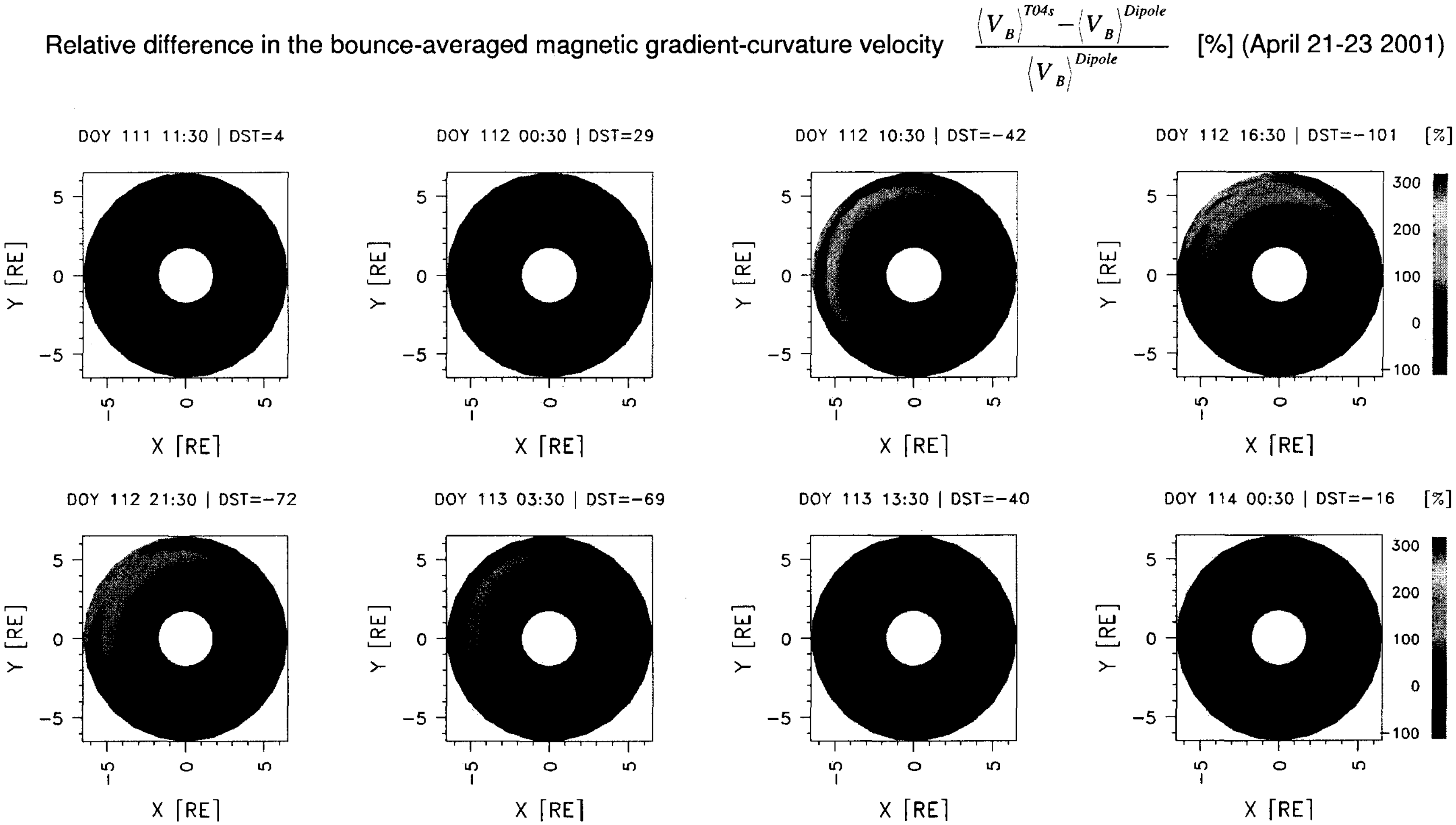

Figure 5-4: Relative difference in the bounce-averaged magnetic gradient-curvature velocities at eight different times. The Sun is on the right.

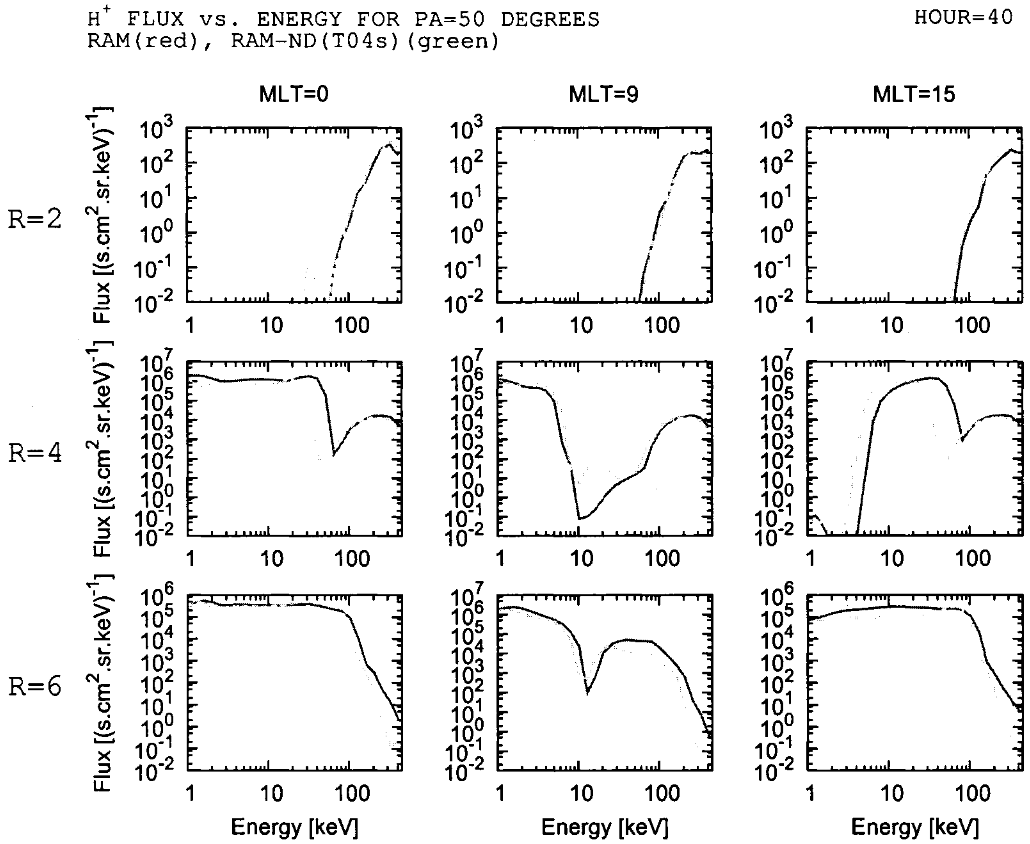

Figure 5-5: Trapped equatorial H^+ flux vs. energy at L=2, 4, 6 and MLT=0, 9, 15 for pitch angle 50° at hour 40 after UT 00 on April 21, 2001.

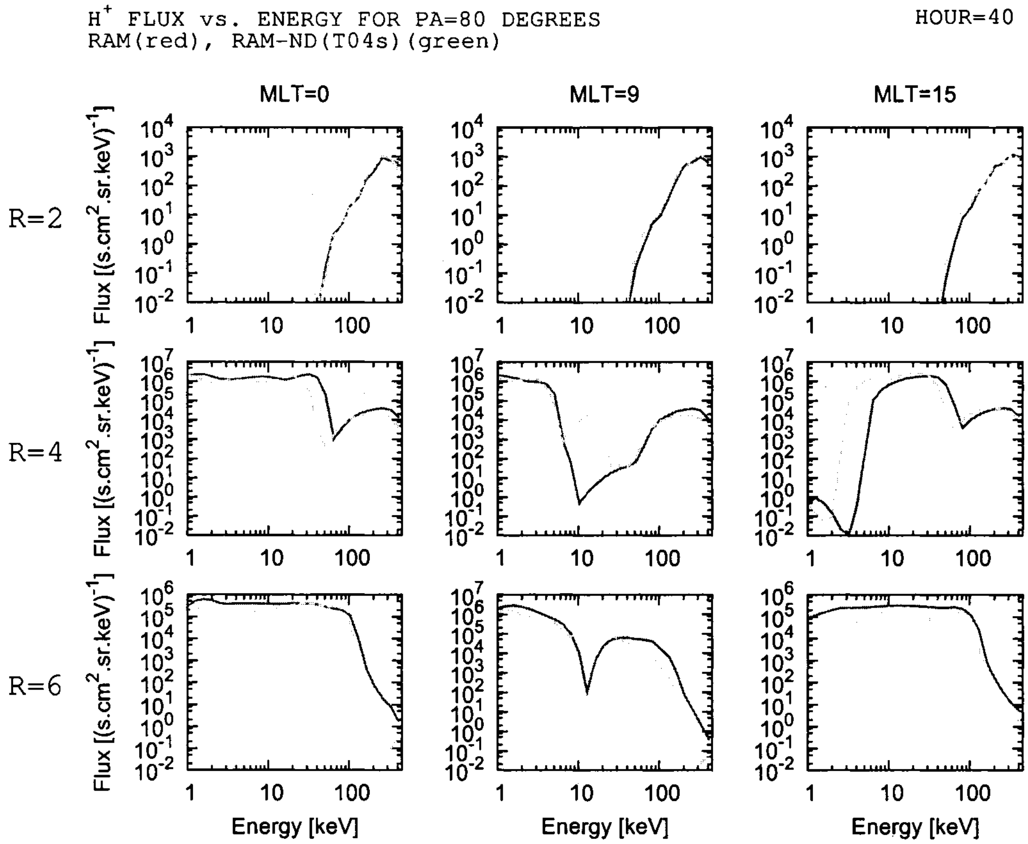

Figure 5-6: Trapped equatorial H^+ flux vs. energy at L=2, 4, 6 and MLT=0, 9, 15 for pitch angle 80° at hour 40 after UT 00 on April 21, 2001.

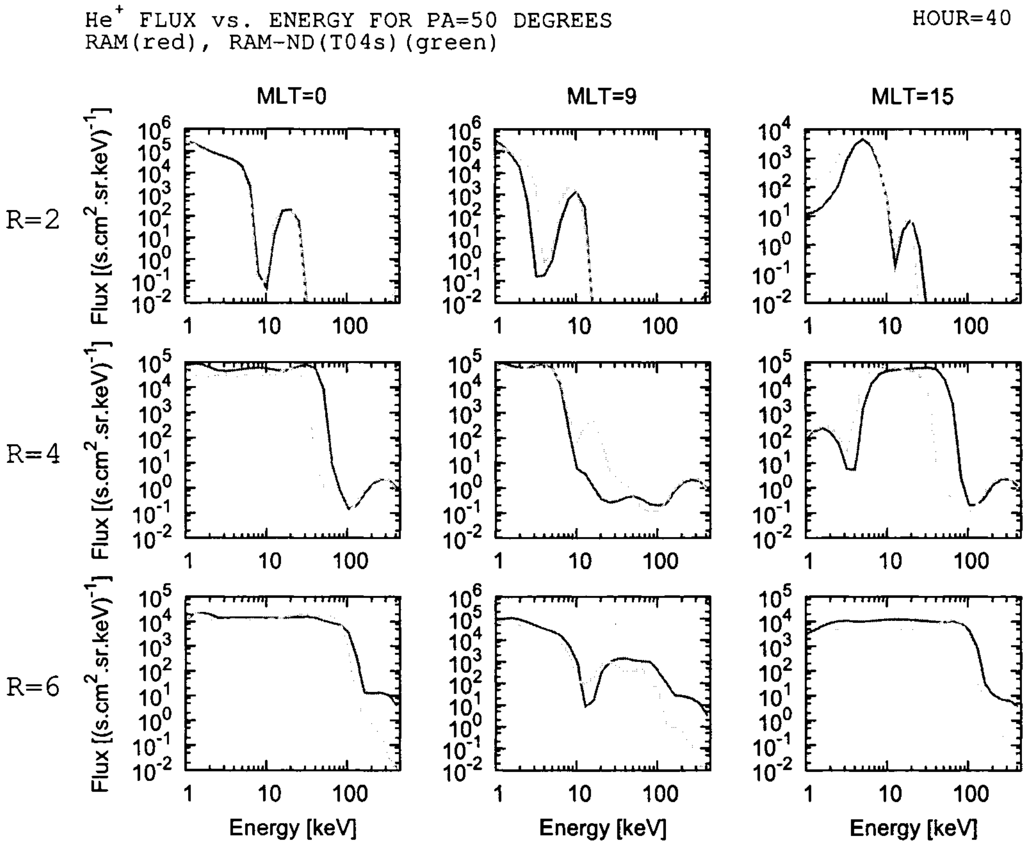

Figure 5-7: Trapped equatorial He$^+$ flux vs. energy at L=2, 4, 6 and MLT=0, 9, 15 for pitch angle 50° at hour 40 after UT 00 on April 21, 2001.

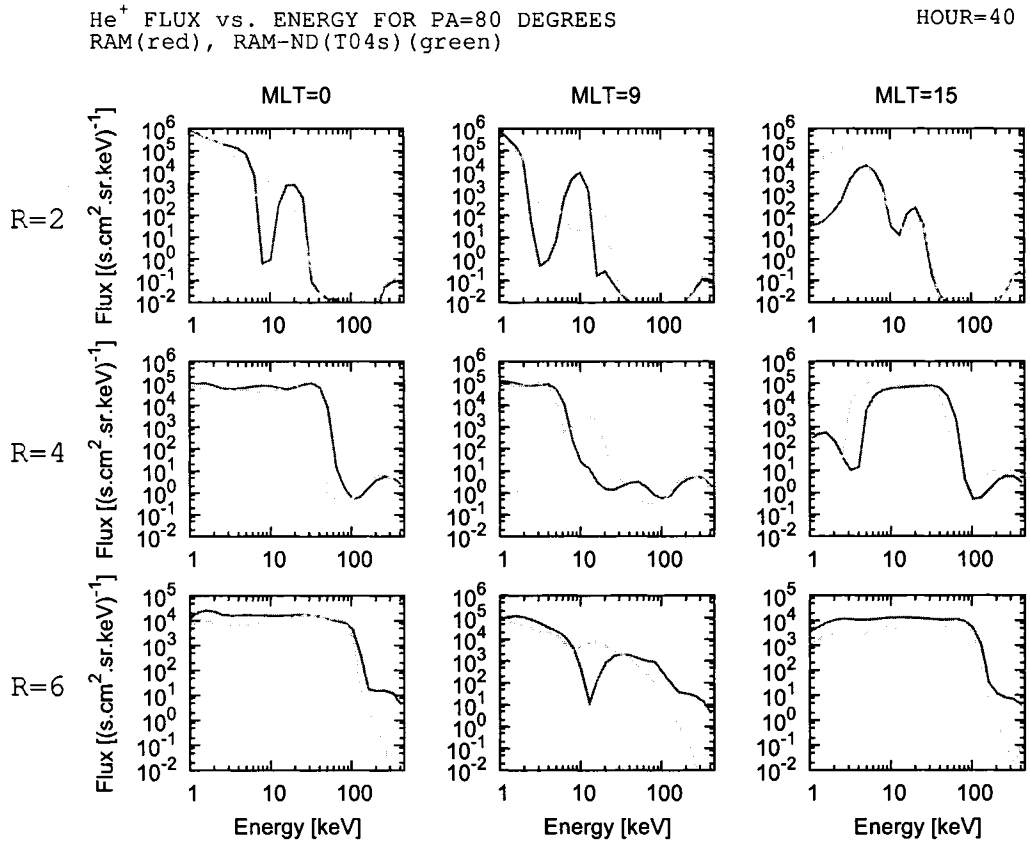

Figure 5-8: Trapped equatorial He$^+$ flux vs. energy at L=2, 4, 6 and MLT=0, 9, 15 for pitch angle 80° at hour 40 after UT 00 on April 21, 2001.

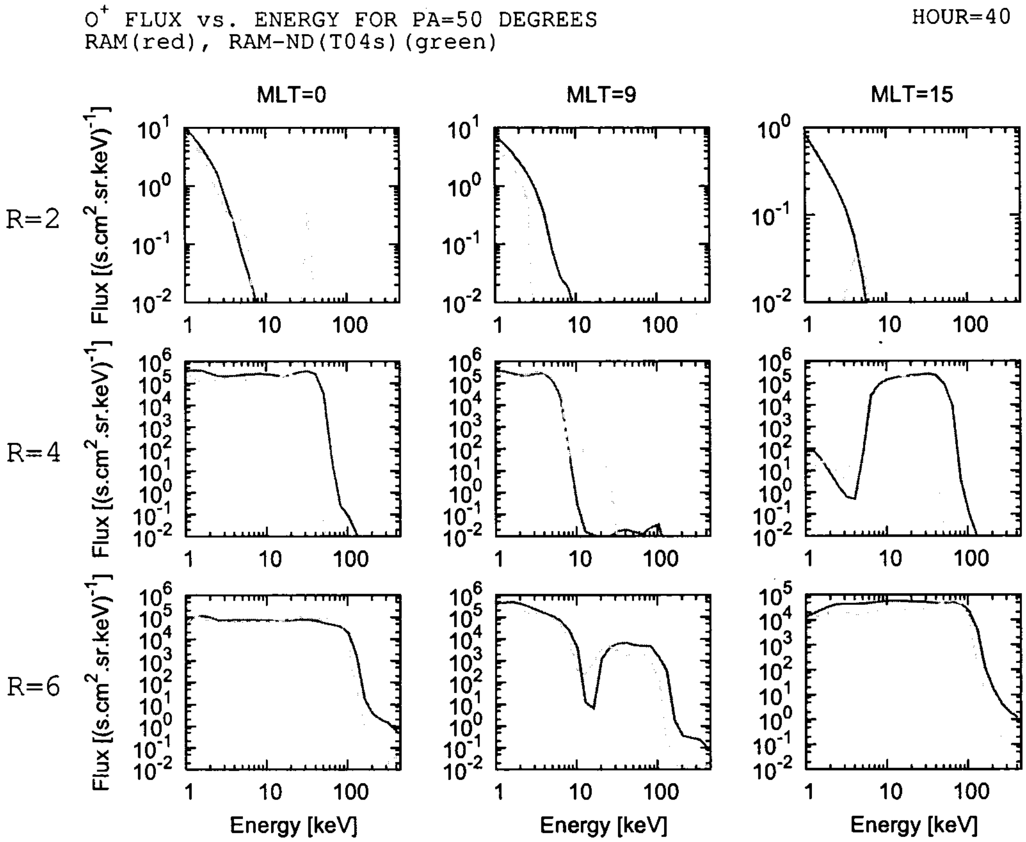

Figure 5-9: Trapped equatorial O^+ flux vs. energy at L=2, 4, 6 and MLT=0, 9, 15 for pitch angle 50° at hour 40 after UT 00 on April 21, 2001.

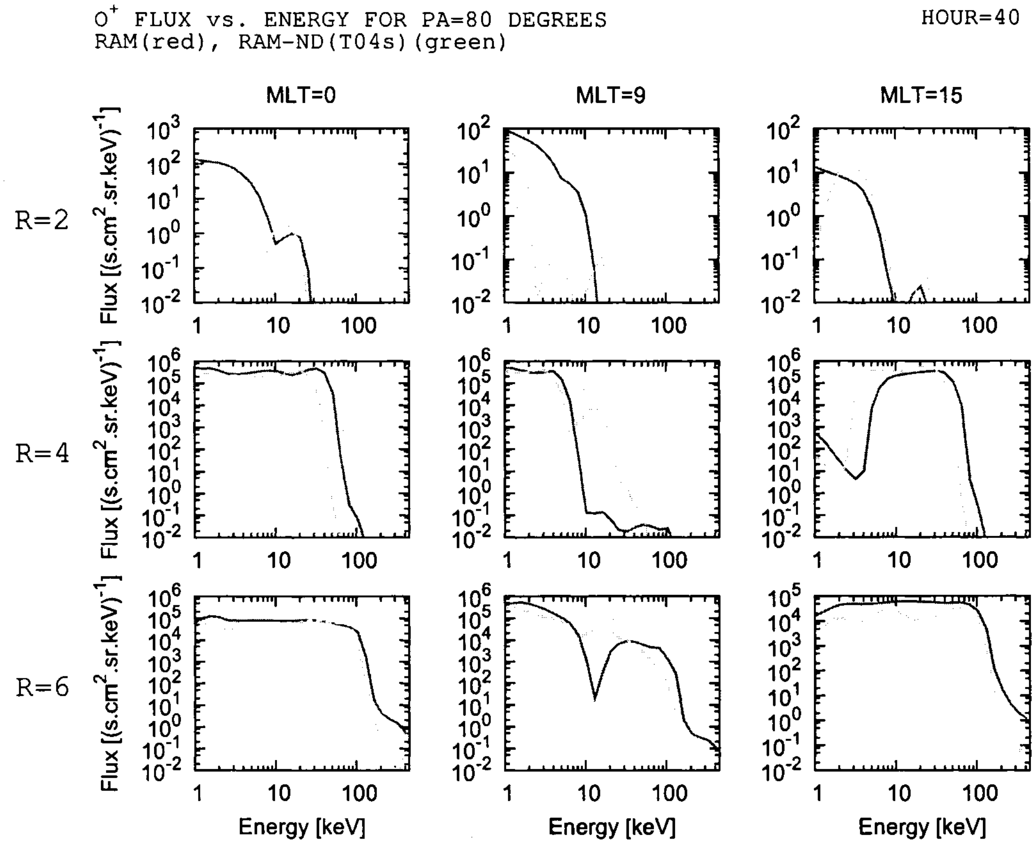

Figure 5-10: Trapped equatorial O^{+} flux vs. energy at L=2, 4, 6 and MLT=0, 9, 15 for pitch angle 80° at hour 40 after UT 00 on April 21, 2001.

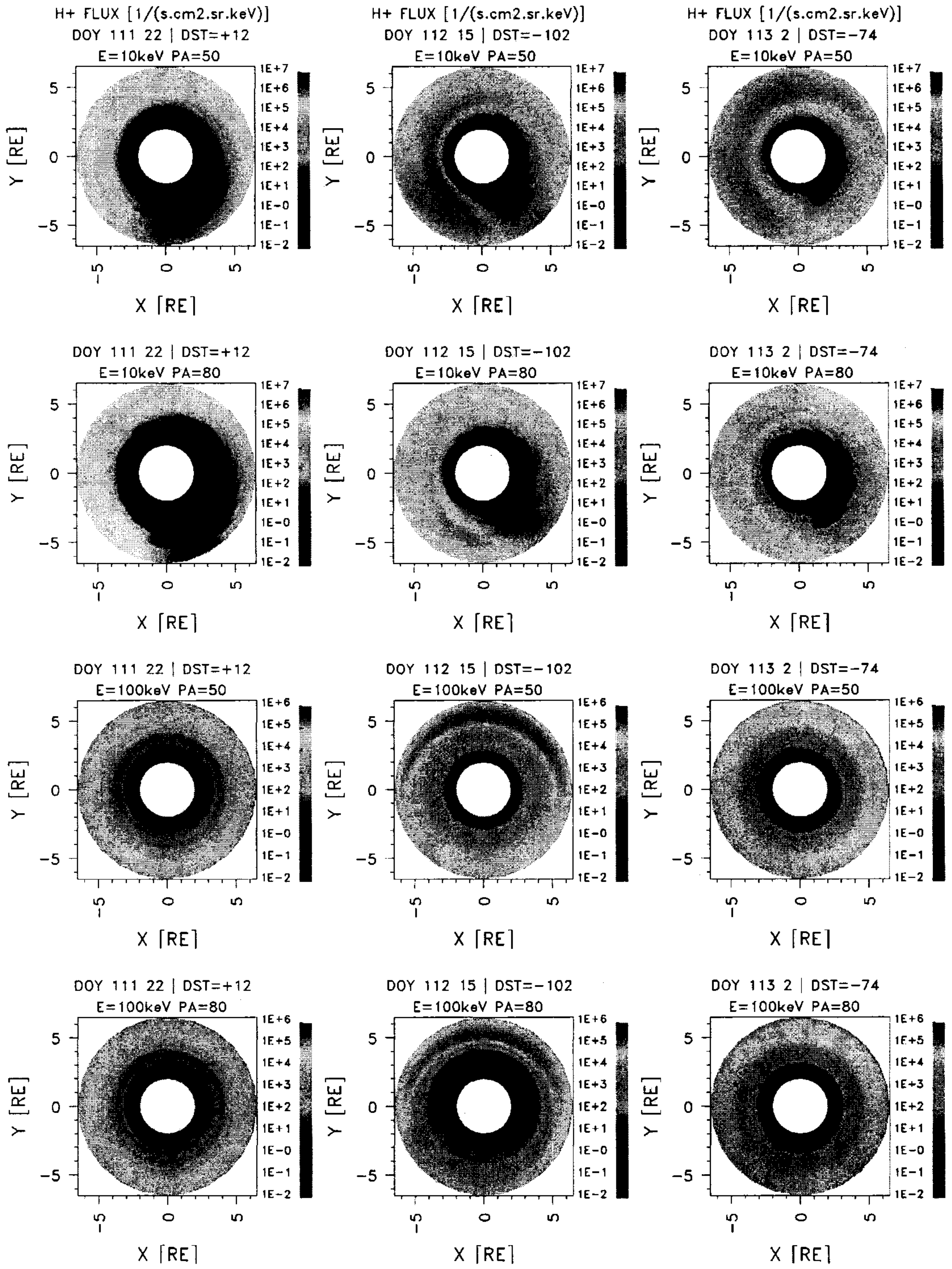
H+ FLUX [1/(s.cm2.sr.keV)] DOY 111 22 | DST=+12 E=10keV PA=50

H+ FLUX [1/(s.cm2.sr.keV)] DOY 112 15 | DST=-102 E=10keV PA=50

H+ FLUX [1/(s.cm2.sr.keV)] DOY 113 2 | DST=-74 E=10keV PA=50

DOY 111 22 | DST=+12 E=10keV PA=80

DOY 112 15 | DST=-102 E=10keV PA=80

DOY 113 2 | DST=-74 E=10keV PA=80

DOY 111 22 | DST=+12 E=100keV PA=50

DOY 112 15 | DST=-102 E=100keV PA=50

DOY 113 2 | DST=-74 E=100keV PA=50

DOY 111 22 | DST=+12 E=100keV PA=80

DOY 112 15 | DST=-102 E=100keV PA=80

DOY 113 2 | DST=-74 E=100keV PA=80

Figure 5-11: Equatorial H^+ flux for RAM model at three different times during the storm of April 21, 2001. Rows 1 and 2 show the flux for pitch angles 50° and 80° for energy of 10 keV. Rows 3 and 4 show the flux for pitch angles 50° and 80° for energy of 100 keV. The Sun is on the right.

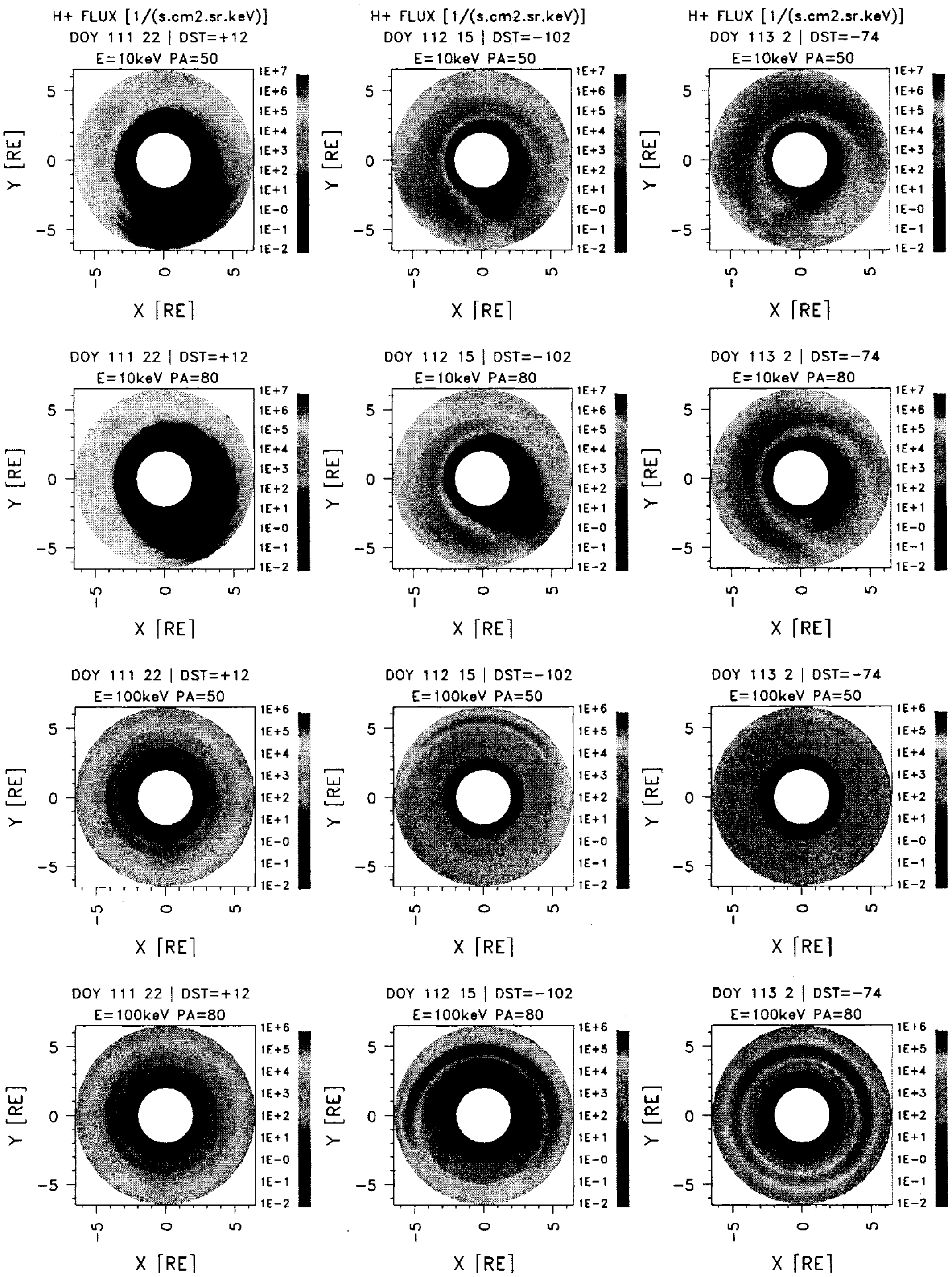

Figure 5-12: Equatorial H$^+$ flux for RAM-ND model at three different times during the storm of April 21, 2001. Rows 1 and 2 show the flux for pitch angles 50° and 80° for energy of 10 keV. Rows 3 and 4 show the flux for pitch angles 50° and 80° for energy of 100 keV. The Sun is on the right.

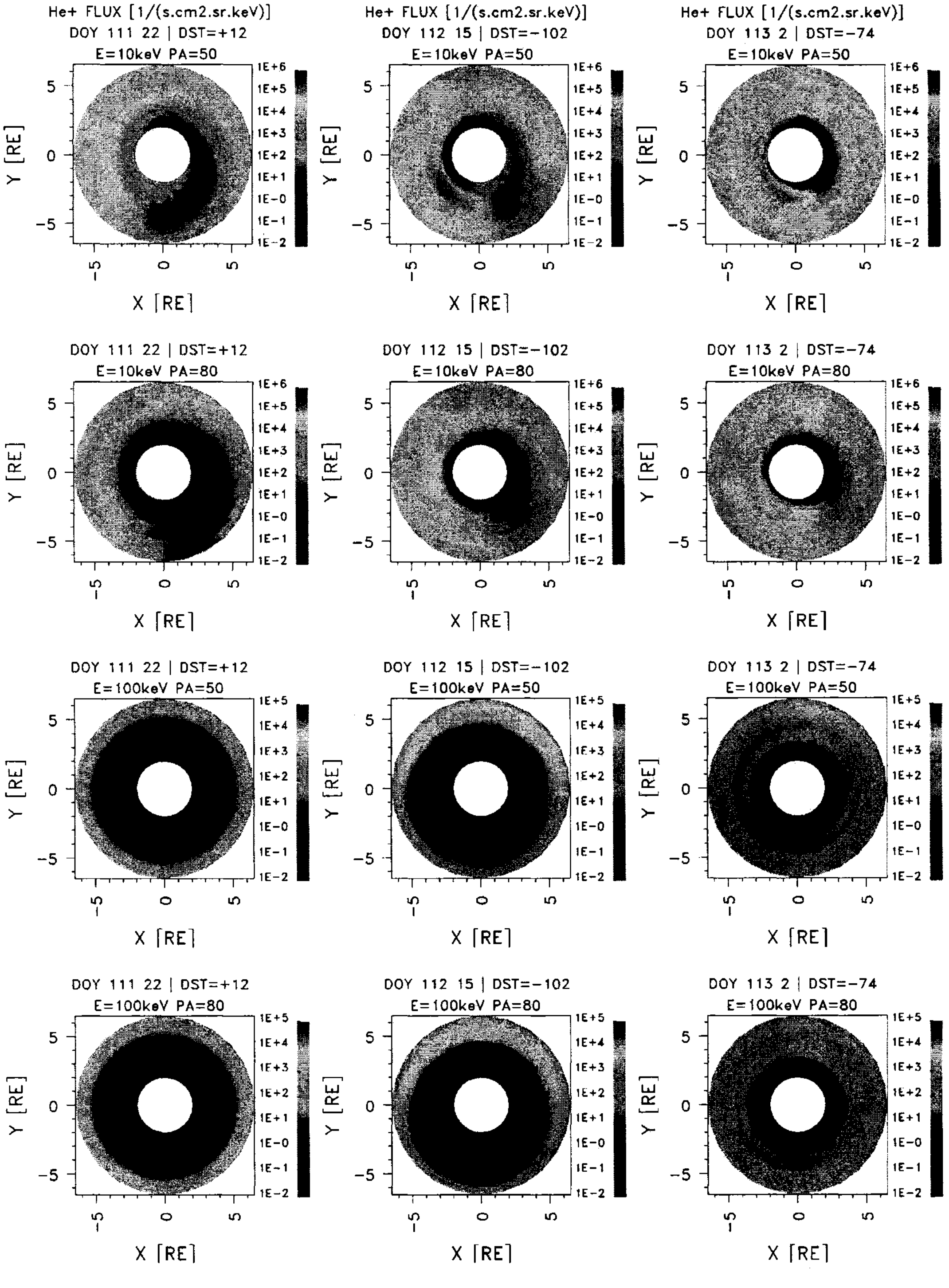

Figure 5-13: Equatorial He$^+$ flux for RAM model at three different times during the storm of April 21, 2001. Rows 1 and 2 show the flux for pitch angles 50° and 80° for energy of 10 keV. Rows 3 and 4 show the flux for pitch angles 50° and 80° for energy of 100 keV. The Sun is on the right.

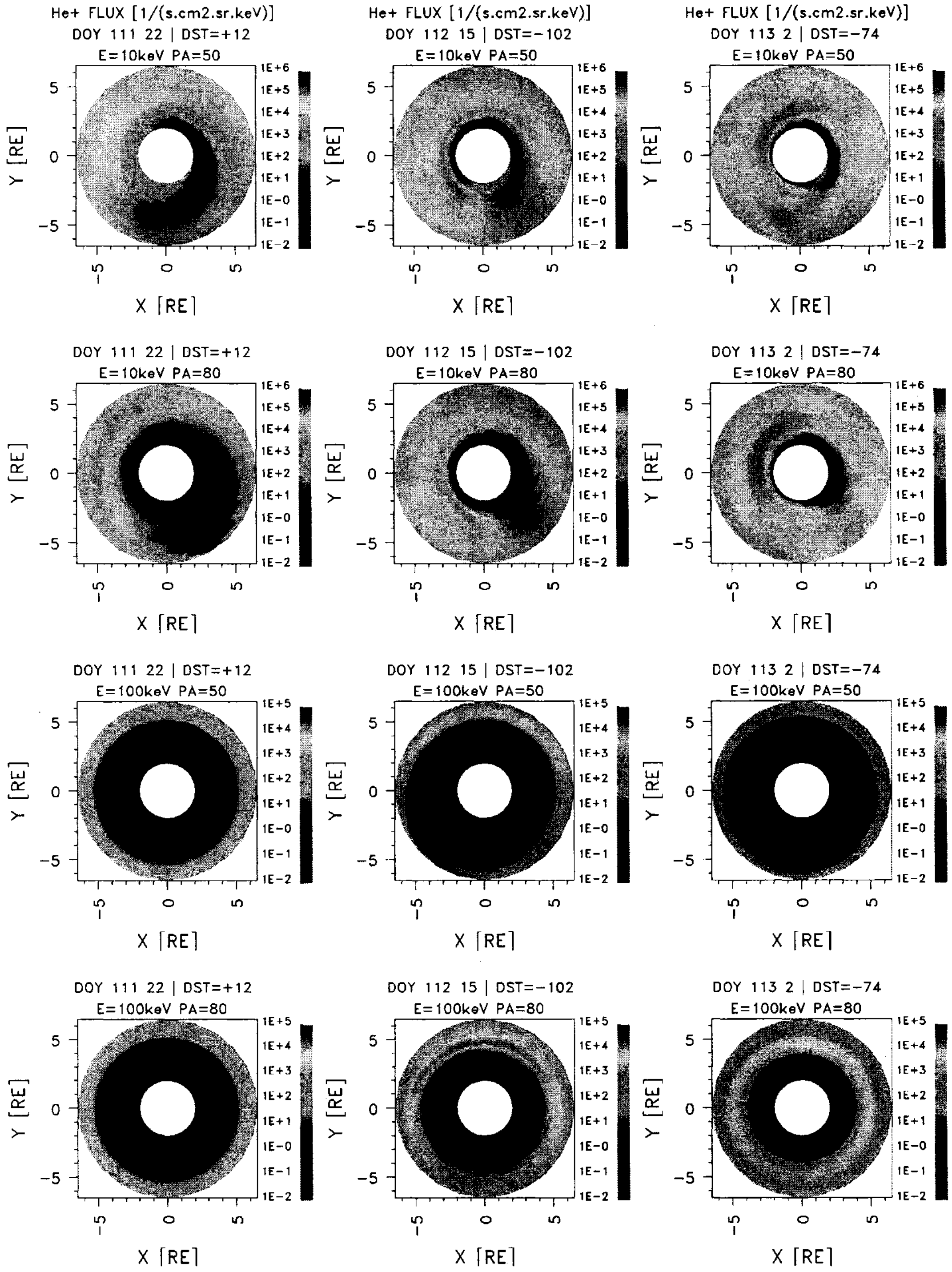

Figure 5-14: Equatorial He$^+$ flux for RAM-ND model at three different times during the storm of April 21, 2001. Rows 1 and 2 show the flux for pitch angles 50° and 80° for energy of 10 keV. Rows 3 and 4 show the flux for pitch angles 50° and 80° for energy of 100 keV. The Sun is on the right.

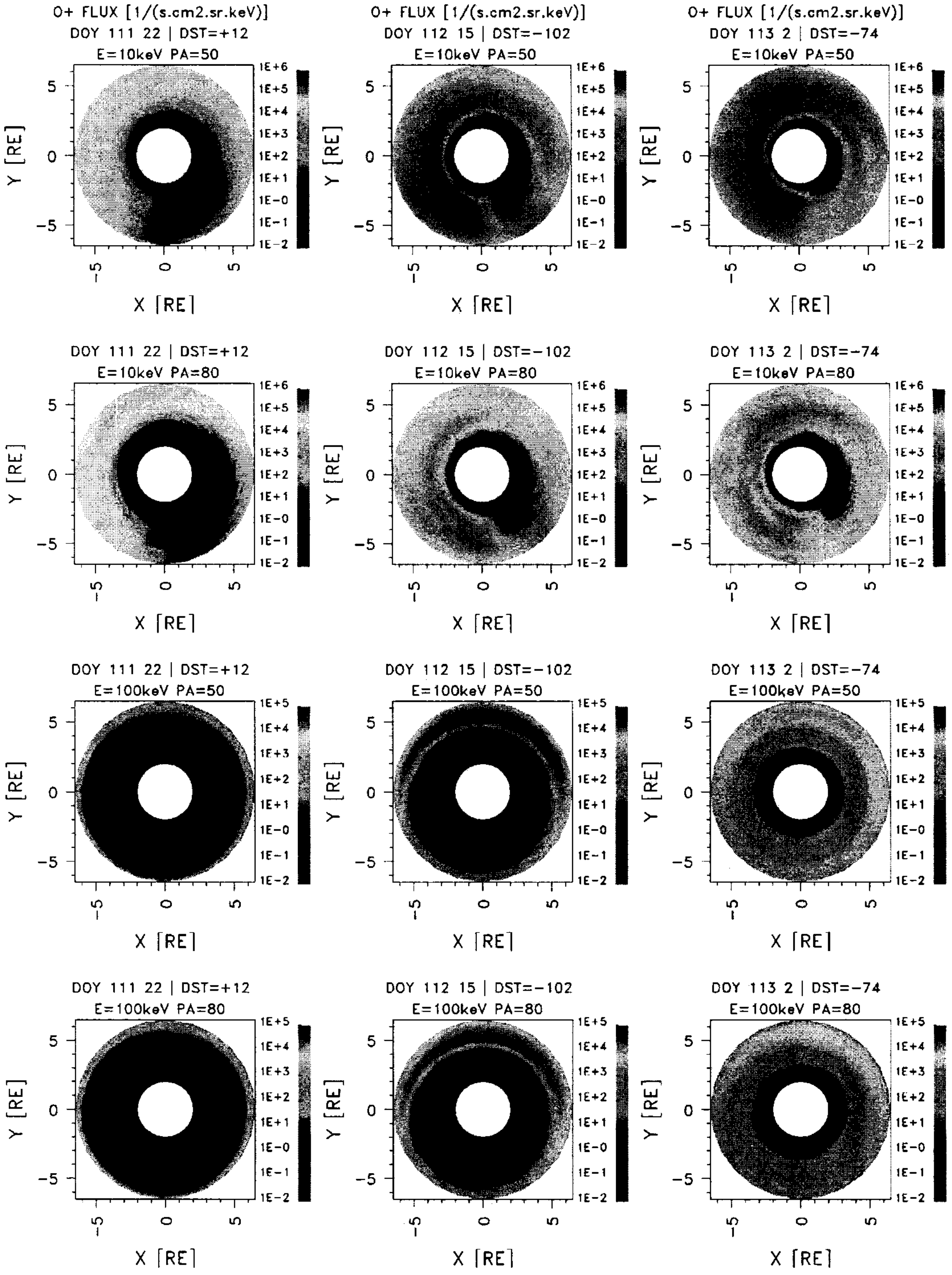

Figure 5-15: Equatorial O^+ flux for RAM model at three different times during the storm of April 21, 2001. Rows 1 and 2 show the flux for pitch angles 50° and 80° for energy of 10 keV. Rows 3 and 4 show the flux for pitch angles 50° and 80° for energy of 100 keV. The Sun is on the right.

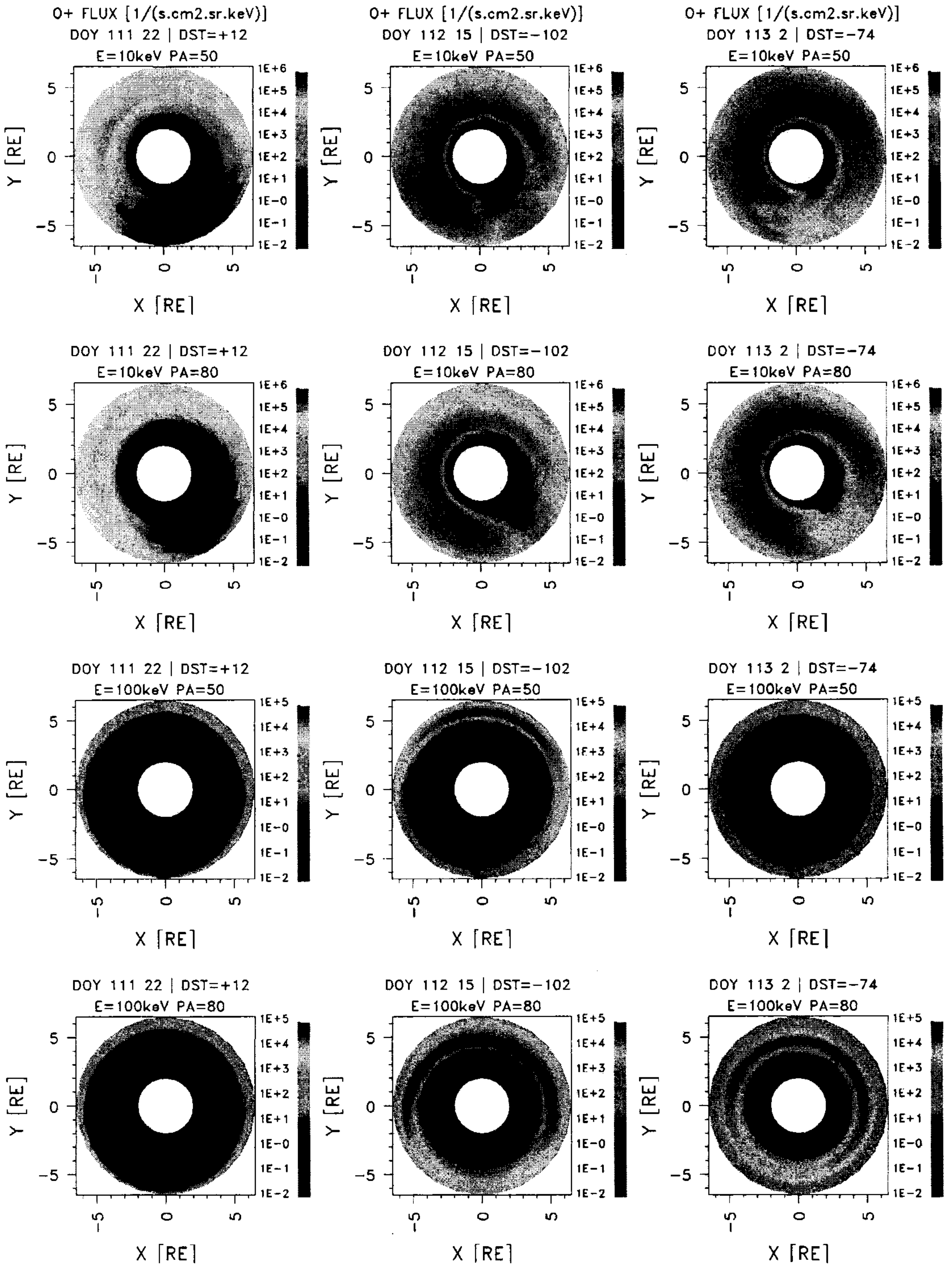

Figure 5-16: Equatorial O^+ flux for RAM-ND model at three different times during the storm of April 21, 2001. Rows 1 and 2 show the flux for pitch angles 50° and 80° for energy of 10 keV. Rows 3 and 4 show the flux for pitch angles 50° and 80° for energy of 100 keV. The Sun is on the right.

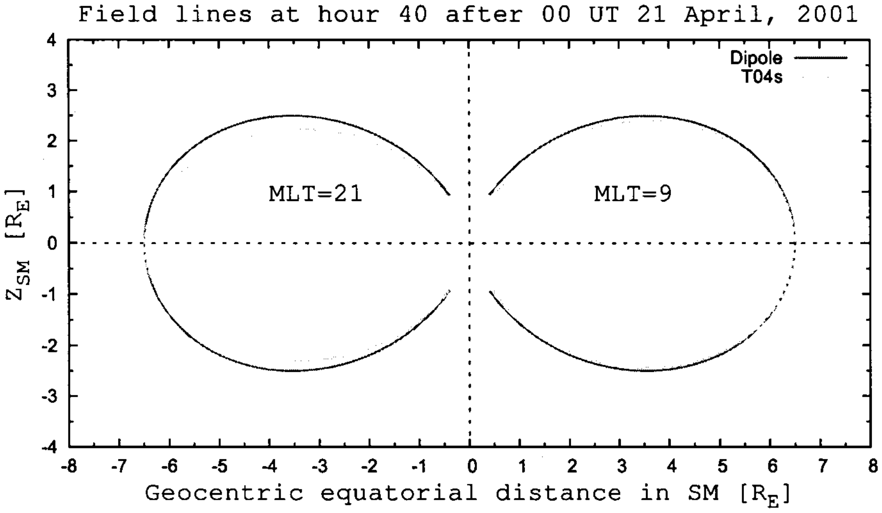

Figure 5-17: Field line shape comparison between a dipole field and the T04s model. The field lines are ploted for MLT=9 and MLT=21 at hour 40 (*Dst* minimum) after 00 UT April 21, 2001. The minus sign on the x-axis denotes that the field line is in the midnight side of the coordinate system.

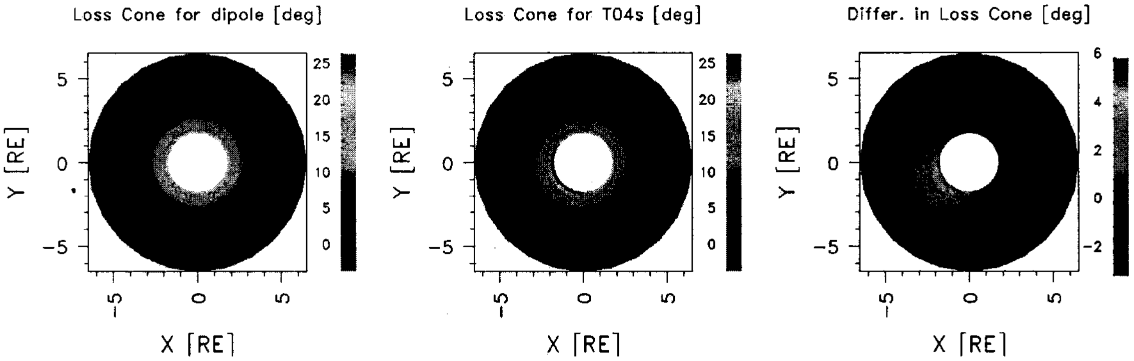

Figure 5-18: Loss cone values [degrees] comparison between a dipole field and the T04s model at hour 40 (*Dst* minimum) after 00 UT April 21, 2001 with regard to MLT and geocentric radial distance. The first plot shows the loss cone values for a dipole field approximation, the second plot shows the respective values for the T04s field, and the third plot shows the difference in the loss cones between the T04s field and the dipole. The Sun is on the right.

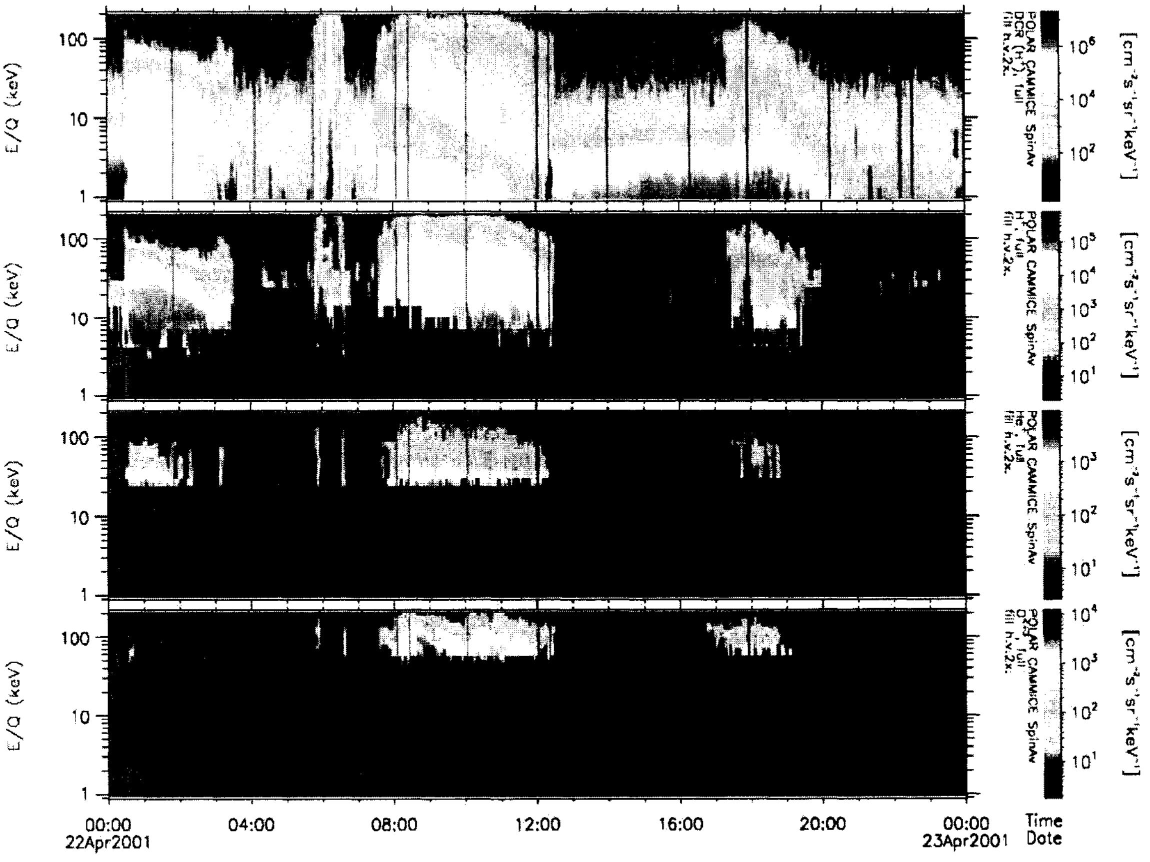

Figure 5-19: Energy spectra of the spin averaged ion flux measured by Polar/CAMMICE during the storm period of April 22, 2001. The top plot shows the double coincidence response (DCR) H^+ flux, followed by the plots for H^+, He^+, and $O^{<+3}$ ion fluxes respectively (courtesy to R. Friedel, LANL).

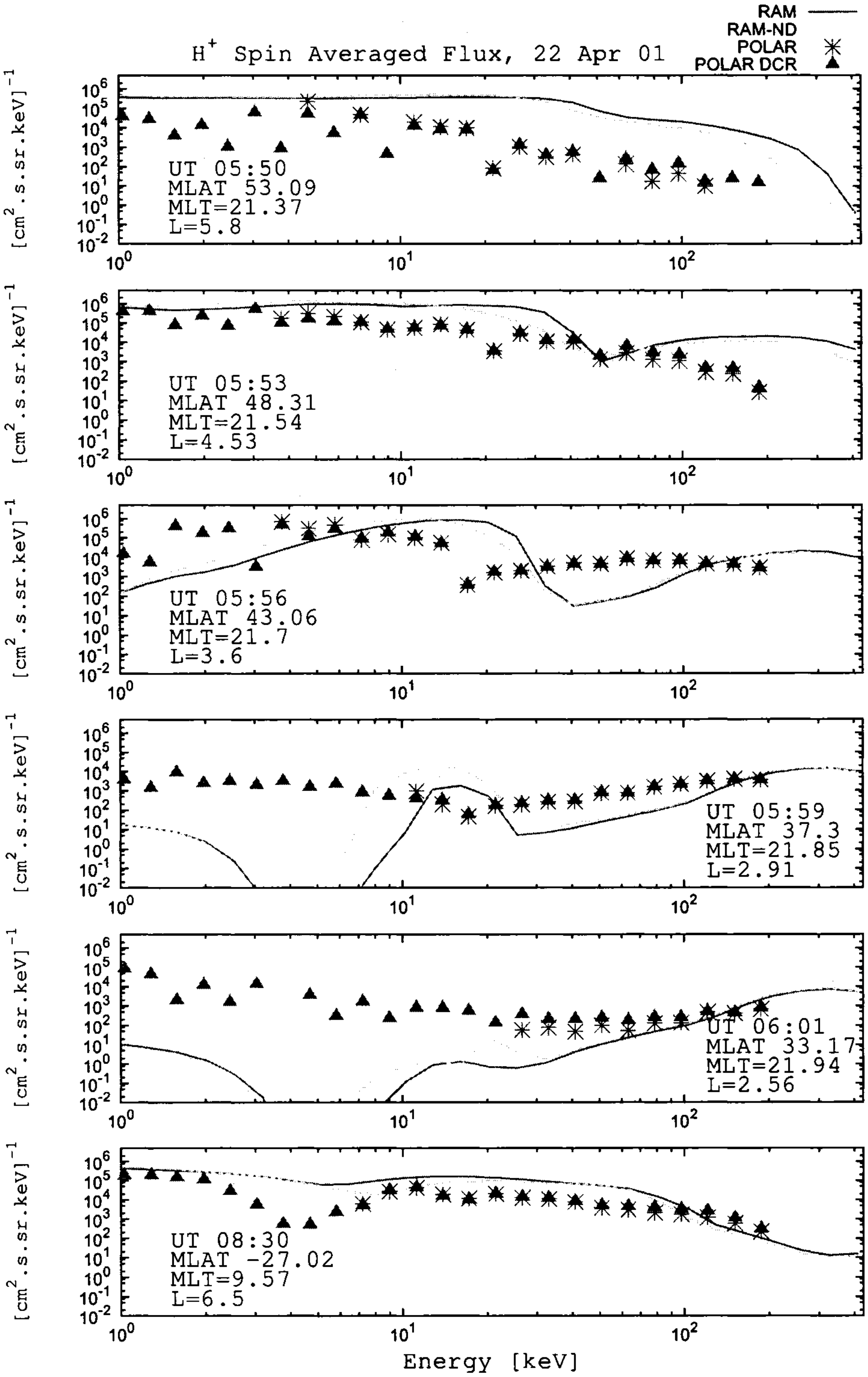

Figure 5-20: Energy spectra of the spin averaged H$^+$ flux at six different times, L-value, and MLT during the storm period of April 22, 2001. The flux given by RAM is in red, the flux given by RAM-ND in green, the Polar/CAMMICE H$^+$ flux data is plotted with stars, and the Polar/CAMMICE DCR H$^+$ flux is presented with triangles.

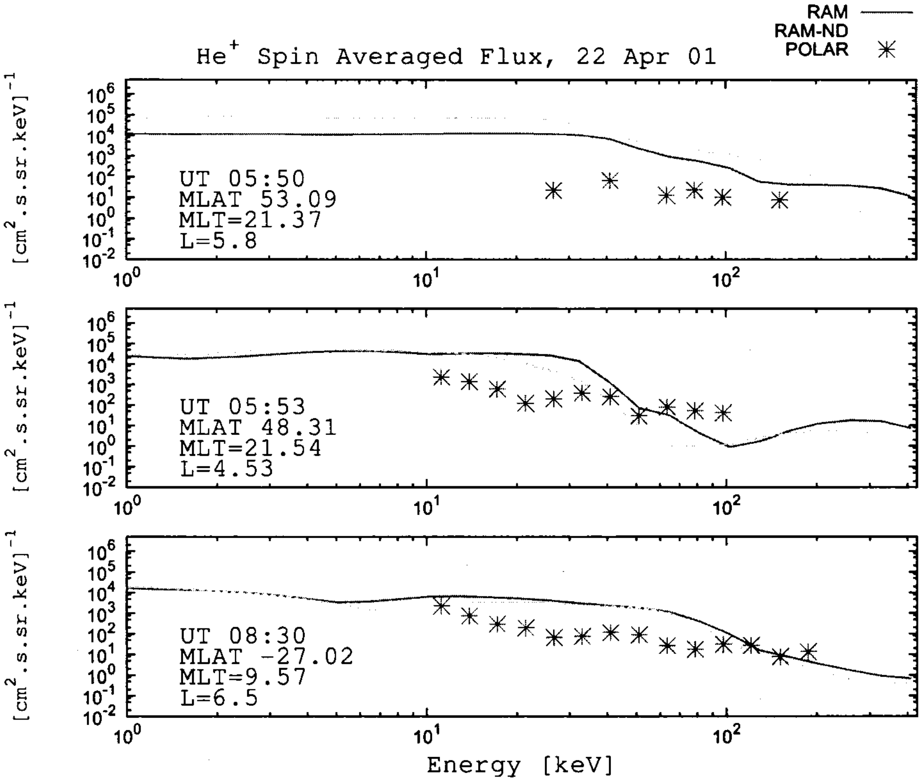

Figure 5-21: Energy spectra of the spin averaged He$^+$ flux at three different times, L-value, and MLT during the storm period of April 22, 2001. The flux given by RAM is in red, the flux given by RAM-ND in green, and the Polar/CAMMICE He$^+$ flux data is plotted with stars.

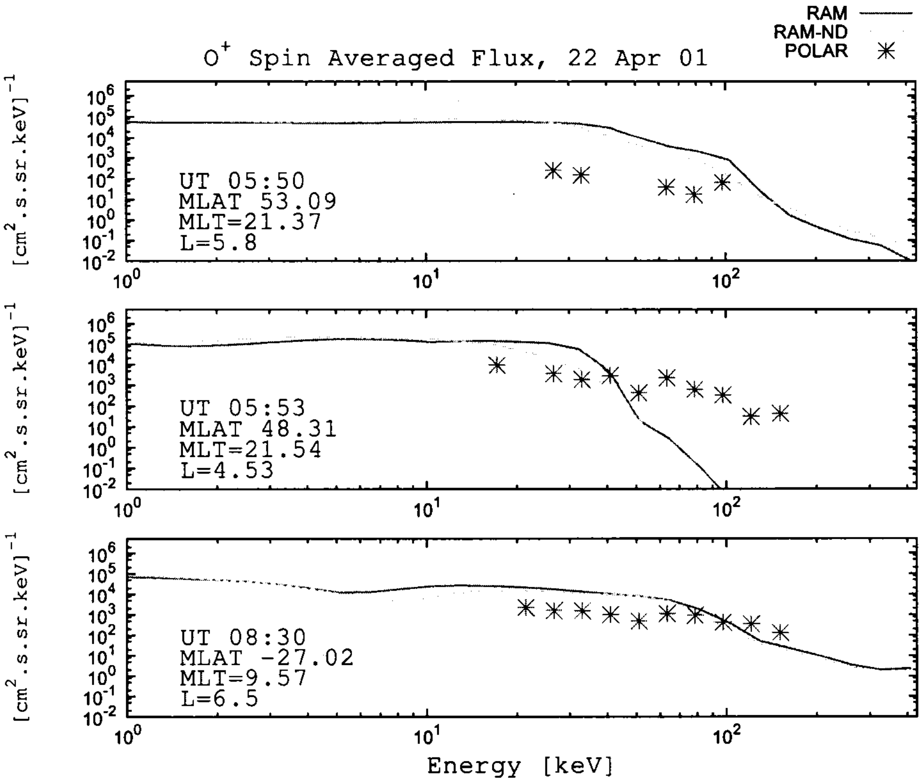

Figure 5-22: Energy spectra of the spin averaged O^+ (O^{++}) flux at three different times, L-value, and MLT during the storm period of April 22, 2001. The O^+ flux given by RAM is in red, the O^+ flux given by RAM-ND in green, and the Polar/CAMMICE $O^{<+3}$ flux data is plotted with stars.

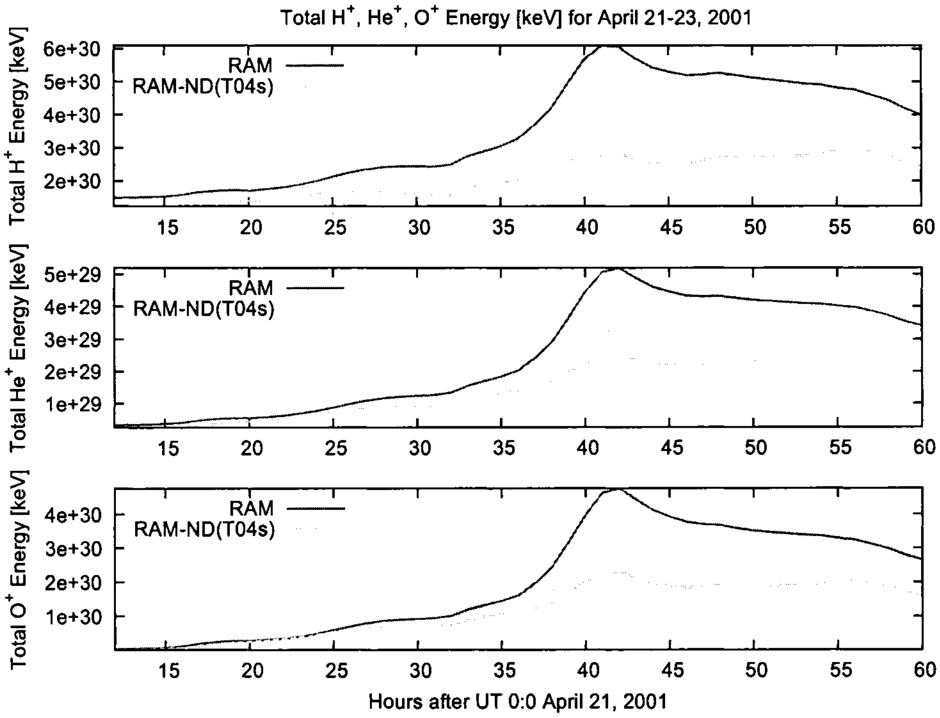

Figure 5-23: Total ring current energy for H$^+$, He$^+$, and O$^+$ ions during the storm period of April 21-23, 2001.

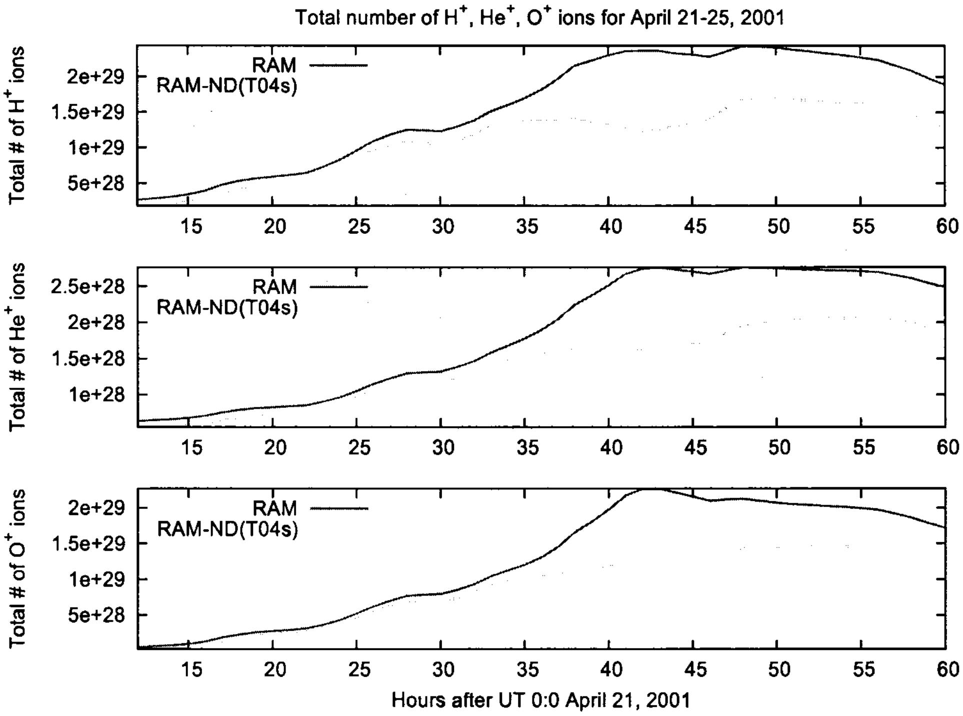

Figure 5-24: Total ring current number of particles for H^+, He^+, and O^+ ions during the storm period of April 21-23, 2001.

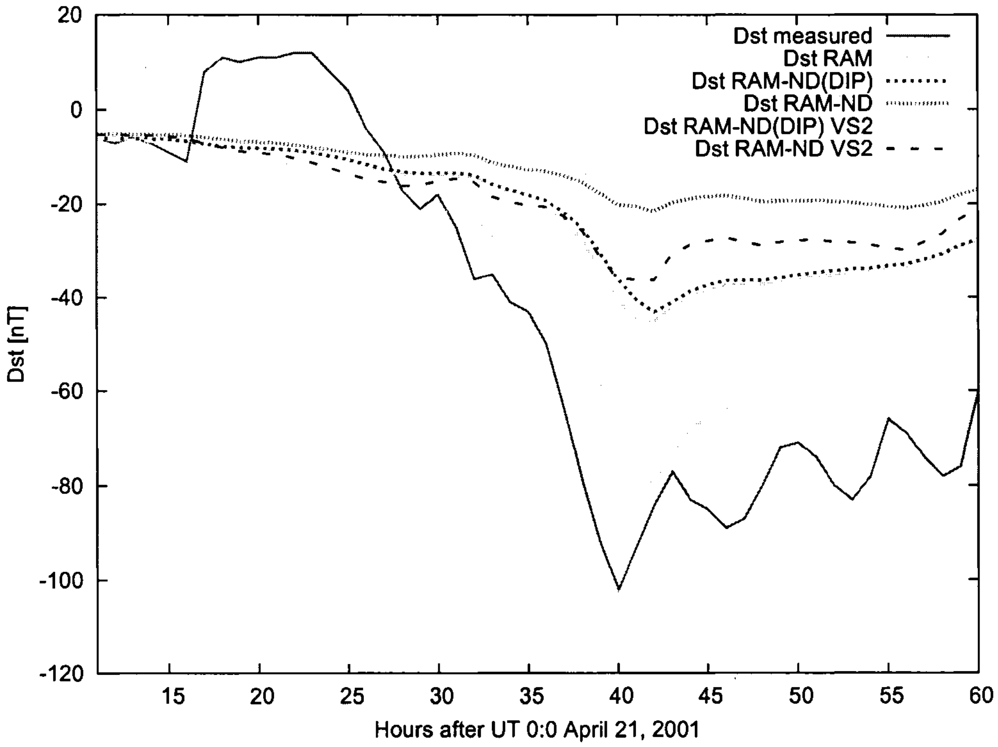

Figure 5-25: *Dst* index [nT] during the storm period of April 21-23, 2001. The measured *Dst* is in red, *Dst* for RAM and RAM-ND (dipole approximation) are in green and blue, and *Dst* for RAM-ND is in purple. The two plots with index "VS2" show the modeled *Dst* when using two times larger Volland-Stern convection field: RAM-ND VS2 (dipole approximation) is in light blue and RAM-ND VS2 is the dashed black line.

CHAPTER 6

CONCLUSIONS

An improved kinetic model (RAM-ND) of the terrestrial ring current was developed for a stormtime geomagnetic field. The recent empirical stormtime magnetic field model T04s [Tsyganenko and Sitnov, 2005] was used to describe the external field of the Earth and the IGRF model field was used to represent the main field of the Earth. A time-dependent Volland-Stern potential was used to describe the convection electric field. The processes considered in this study were particle drifts, losses due to charge exchange with geocoronal hydrogen and atmospheric losses. The moderate storm of 21-23 April 2001 was simulated and the differences between the existing RAM model and the updated RAM-ND model were studied. Solar wind plasma and interplanetary magnetic field data obtained by the Advanced Composition Explorer (ACE) satellite were used to drive the T04s model. Energetic particle observations from the Los Alamos National Laboratory (LANL) satellites at geosynchronous orbit were used as boundary conditions.

A tracing and bounce-averaging numerical technique was developed for the field line tracing and computation of the respective bounce-averaged quantities in an arbitrary time-dependent geomagnetic field. The bounce-averaged exospheric hydrogen densities $\langle H_{Dens} \rangle$ and bounce averaged magnetic gradient-curvature drift velocities $\langle \mathbf{V}_B \rangle$ were calculated for various configurations of the Earth's magnetic field.

We found that the calculated $\langle H_{Dens} \rangle$ using the T04s model was smaller at dusk-midnight than the bounce-averaged density calculated for dipole field and $\langle H_{Dens} \rangle$ was bigger towards the dawn-noon side. For a moderate-to-large storm this difference reached around -30% at dusk-midnight and it was around +5% at the noon side and close to Earth. The bounce-averaged magnetic gradient-curvature drift velocities for the T04s field were bigger at dusk-midnight than those for dipole field and they became smaller towards the dawn-noon side. Even for quiet time the difference was significant - between 20% on the nightside and -20% on the dayside. During storm time it was $\sim$ 200% and reached more than 250% in isolated regions on the midnight-dusk side and it was around -10% to -20% on the dayside. It was found that $\langle H_{Dens} \rangle$ and $\langle \mathbf{V}_B \rangle$ strongly depended on the geomagnetic field configuration, namely the shape and the location of the field lines, the position of the mirror points and the magnitude of the magnetic field. It was found that the contribution of $\langle \mathbf{V}_R \rangle$ is small compared to $\langle \mathbf{V}_B \rangle$, being $\sim$ 5% and was not included in the RAM-ND simulations. To estimate our numerical error in the bounce-averaging technique, we computed $\langle H_{Dens} \rangle$ and $\langle \mathbf{V}_{GC} \rangle$ for a dipole magnetic field and then we compared them with the analytically calculated respective values for a dipole configuration and the numerical error was found to be around 2%.

To study the effects of a time-dependent non-dipole magnetic field in the RAM-ND model, the time evolution of the trapped equatorial flux was calculated for the major ring current ion species (H^+, He^+, and O^+) in the $\sim 1 - 400$ keV energy range for various pitch angles at different magnetic local times and geocentric radial distances. All particles are considered to have an adiabatic behavior, i.e. there is no violation of the frozen-in condition for the plasma ions due to magnetic mirror instabilities accounting for finite ion gyroradius radius effects. The loss cone (concerning losses in the atmosphere) in RAM-ND was approximated with the loss cone for a dipole field due to the small difference (the largest being $\sim 5^\circ$ in an isolated region at ~ 2 R_E) between them during a moderate storm.

It was found that close to Earth (~ 2 R_E) the low energy H^+ flux calculated with the RAM-ND model is similar to the flux given by RAM due to the dipolar nature of the T04s field at low altitudes. The relatively small difference in the bounce-averaged hydrogen densities and magnetic gradient-curvature drifts at low latitudes suggest that the charge exchange rate around L=2 is similar for both dipole and non-dipole field configuration at the peak of the storm (minimum *Dst*). At larger L-shells the difference in the azimuthal drifts and the bounce-averaged exospheric hydrogen leads to greater fluxes and a shift of the stagnation dip towards lower energy around the prenoon side in the mid-energy range for RAM-ND. The high energy proton flux was generally higher for RAM-ND at large L-shells after the storm main phase due to the lower charge exchange rate and very high azimuthal drifts. In general, both RAM-ND and RAM models showed similar low energy proton distributions with a slight increase in the equatorial flux after the storm main phase for RAM-ND. The RAM-ND distribution indicated stronger dominance of the high energy component during the storm recovery phase and showed a slight increase in the total ring current energy and number of H^+ during the recovery phase. The RAM-ND ring current H^+ calculations are consistent with recent calculations [Jordanova et al., 2006; Ganushkina et al., 2006; Milillo et al., 2006]. The total ring current energy was reduced by $\sim 30\%$ when the RAM-ND model was used.

Both RAM-ND and RAM models gave similar pitch angle and energy distribution of the equatorial He^+ fluxes before the development of the storm main phase. During the main and recovery phases of the storm, however, the RAM-ND flux developed much stronger pitch angle anisotropy than the RAM at high energies. The bulk of the high energy flux component was located closer to Earth for RAM-ND for large pitch angles and formed a steady symmetrical profile during the recovery phase at around L=4. The calculations for the total energy and particle number for both models showed that the contribution of He^+ during the main phase is about 4% of the total ring current energy which was consistent with previous ring current measurements [Daglis et al., 1993].

The low energy O^+ flux had similar values for both RAM and RAM-ND models throughout the storm. As before, RAM-ND gave slightly higher flux during and after the storm main phase. Large differences in the flux were observed at both low and high energies during and after the Dst minimum. Despite the relatively large charge exchange cross-sections for oxygen ions, the total number of O^+ for RAM-ND continued to increase after minimum Dst until hour ~ 48 which was an indication that the different ionospheric sources remained active for several hours during stormtime. This lead to the accumulation of energetic O^+ due to the smaller charge exchange losses of oxygen ions for the case of T04s stormtime field.

The energy spectra of the spin averaged ion flux measured by the Polar/CAMMICE-MICS instrument were compared with the calculated spin averaged flux for the three major ring current ion species few hours before the Dst reached minimum. Due to the scarcity of the data available it was not possible to perform a thorough study at multiple L-shells, MLTs, and different times. The spin averaged flux profile dependence on the L-shell value for H^+ was studied at midnight-dusk. At the prenoon side data was not available and the flux only at the boundary (L=6.5) was compared. It was found that for H^+ at midnight-dusk both RAM-ND and RAM fluxes described the data beyond 3 R_E reasonably well with the RAM-ND model performing slightly better than RAM within the mid-energy range. It was shown that the minima in the calculated spin averaged flux profiles moved towards smaller energies when the L-value decreased which was also observed in the data. Close to Earth, however, at low energies the measured flux did not have a well expressed minimum, while the modeled fluxes for both models had deep and broad minima. In general, the position of the dip in the modeled fluxes was found to be at higher energies than the dip in the data flux. The position of the minima in the RAM-ND flux was found to be located closer to the dip in the measured flux in most of the cases. At the midnight-dusk side there were only two available data sets for both He^+ and O^+ ions which were at around 4.5 and 5.8 R_E. The modeled fluxes were $1-3$ orders of magnitude higher than the measured ones in the mid-to-high energy range for both ion species. The RAM-ND spin averaged flux had values closer to the measured ones for O^+ at both locations and for He^+ at $\sim$ 4.5 R_E, but was about 10 times higher than the RAM flux for He^+ at 5.8 R_E. On the prenoon side at L=6.5 both RAM and RAM-ND predicted relatively well the measured fluxes for all the three ion species. In general, the fluxes were higher than the measured ones but RAM-ND gave closer values to the measured ones. The differences between the modeled and the measured spin averaged fluxes suggested that incorporating a realistic magnetospheric model into the model was not enough in order to describe well the behavior of the ring current. Due to the fact that the spacecraft was far from the equator at all times it measured only particles with small pitch angles mirroring away from the equatorial plane. Most of the ring current particle population consists of equatorially mirroring particles. This was a possible explanation of the fact why Polar measured smaller fluxes than the modeled ones. It was suggested [e.g., Kistler and Larson, 2000; Angelopoulos et al., 2002; Jordanova et al., 2006] that the role of the electric field model is very important for ion flux calculations in the near-Earth magnetosphere. Due to the nature of the Volland-Stern electric field model used in this study, low energy particle populations on close to Earth trajectories could not be replenished enough by ions coming from the nightside boundary. This resulted in flux depletion at low energies at low L-shells and thus the deep and broad minima were formed in the modeled fluxes. The shift of the dip in the modeled flux profiles towards higher energies was also considered to be due to the Volland-Stern model [Angelopoulos et al., 2002].

An approximate result for the stormtime *Dst* index was presented in this work. The

Dressler-Parker-Sckopke relation for a dipole magnetic field was used to calculate the perturbation to the Dst due to the ring current for a moderate geomagnetic storm. It was found that RAM-ND produces a twice smaller change in the Dst than RAM due to the difference in the total ring current energy. Despite the realistic geomagnetic field (T04s) used in RAM-ND, the result is possibly an underestimation of the stormtime ring current Dst for various reasons. Satellite data imply that the actual electric field may be quite different from what the Volland-Stern model predicts. Recent studies suggested that the changes in the electric field would make a much more significant difference in the simulations than the changes in the magnetic field [Kistler and Larson, 2000]. More realistic electric field models give better agreement with Dst [e.g., Jordanova et al., 2003b]. The large difference between the T04s magnetic field and the dipole field is one major drawback of using the DPS relation in the present version of RAM-ND. A more thorough computation for a general case magnetic field must be considered in future calculations. The contribution of the electron ring current was also not included, which during Dst minimum could contribute up to $\sim$ 19% [e.g., Liu et al., 2005]. In order to obtain a realistic stormtime ring current Dst, all of the above effects must be considered in future simulations.

This study has shown that the use of a time-dependent non-dipole magnetic field gives more realistic description of the stormtime geomagnetic conditions in the near-Earth magnetosphere. Previous versions of the RAM model (dipole field) performed well when the geomagnetic disturbances were of small to moderate intensity. The comparison with the new RAM-ND model showed that for larger storms the implementation of the T04s model would give a more realistic results for the ring current ion flux and total energy in future computations. Future work on the RAM-ND model would focus on the implementation of the various ion flux precipitating processes, a more realistic near-Earth electric field, and the extension of the model to consider relativistic effects.

APPENDICES

APPENDIX A

PARTICLE DRIFTS FOR GENERAL CASE MAGNETIC FIELD

Magnetic Gradient-Curvature Drift

The instant magnetic gradient-curvature drift velocity of the guiding center at point S can be written as Rossi and Olbert [1970]:

$$\mathbf{V}_S = \frac{mV^2}{2qB}\left\{\sin^2\alpha\frac{\mathbf{B}\times\nabla B}{B^2} + 2\cos^2\alpha\frac{\mathbf{B}\times[(\mathbf{B}\cdot\nabla)\mathbf{B}]}{B^3}\right\} \tag{A.1}$$

where V is the particle velocity, and α is the pitch angle at the given point.

$$\begin{aligned} 2\left[(\mathbf{B}\cdot\nabla)\mathbf{B}\right] &= \nabla\times(\mathbf{B}\times\mathbf{B}) + \nabla(\mathbf{B}\cdot\mathbf{B}) - \mathbf{B}(\nabla\cdot\mathbf{B}) + \mathbf{B}(\nabla\cdot\mathbf{B}) \\ &\quad -\mathbf{B}\times(\nabla\times\mathbf{B})_\perp - \mathbf{B}\times(\nabla\times\mathbf{B})_\perp \\ &= \nabla\left(B^2\right) - 2\mathbf{B}\times(\nabla\times\mathbf{B})_\perp \end{aligned} \tag{A.2}$$

Then follows that:

$$\begin{aligned} \frac{\mathbf{B}}{B^2}\times[(\mathbf{B}\cdot\nabla)\mathbf{B}] &= \frac{\mathbf{B}}{B^2}\times\frac{1}{2}\left[\nabla\left(B^2\right) - 2\mathbf{B}\times(\nabla\times\mathbf{B})_\perp\right] \\ &= \frac{\mathbf{B}}{B^2}\times\frac{1}{2}\left[2B\nabla B - 2\mathbf{B}\times(\nabla\times\mathbf{B})_\perp\right] \\ &= \frac{\mathbf{B}\times\nabla B}{B} - \frac{\mathbf{B}\times\left[\mathbf{B}\times(\nabla\times\mathbf{B})_\perp\right]}{B^2} \end{aligned} \tag{A.3}$$

$$\mathbf{B}\times\left[\mathbf{B}\times(\nabla\times\mathbf{B})_\perp\right] = \left[\mathbf{B}\cdot(\nabla\times\mathbf{B})_\perp\right]\mathbf{B} - (\mathbf{B}\cdot\mathbf{B})(\nabla\times\mathbf{B})_\perp \tag{A.4}$$

But $\mathbf{B}\cdot(\nabla\times\mathbf{B})_\perp = 0$. This yields:

$$\mathbf{B}\times\left[\mathbf{B}\times(\nabla\times\mathbf{B})_\perp\right] = -B^2(\nabla\times\mathbf{B})_\perp \tag{A.5}$$

Then:

$$\frac{\mathbf{B}}{B^2}\times[(\mathbf{B}\cdot\nabla)\mathbf{B}] = \frac{\mathbf{B}\times\nabla B}{B} + (\nabla\times\mathbf{B})_\perp \tag{A.6}$$

Finally we replace Equation (A.6) in Equaiton (A.1) and using that $\sin^2\alpha = B/B_m$, for the magnetic gradient-curvature drift we get [Shukhtina, 1993]:

$$\mathbf{V}_S = \frac{mV^2}{qB^2}\left\{\left(1-\frac{1}{2}\frac{B}{B_m}\right)\frac{\mathbf{B}\times\nabla B}{B} + \left(1-\frac{B}{B_m}\right)(\nabla\times\mathbf{B})_\perp\right\} \tag{A.7}$$

where:

$$\mathbf{V}_B = \frac{mV^2}{qB^2}\left(1 - \frac{1}{2}\frac{B}{B_m}\right)\frac{(\mathbf{B}\times\nabla B)}{B} \tag{A.8}$$

is the part related to the gradient and curvature of the magentic field, and:

$$\mathbf{V}_R = \frac{mV^2}{qB^2}\left(1 - \frac{B}{B_m}\right)(\nabla\times\mathbf{B})_\perp \tag{A.9}$$

is the part due to currents related with the curl of the magnetic field.

Radial and Azimuthal Drifts

Equatorial electric field:

$$\mathbf{E}_0 = \left[-\left(\frac{C}{R_0^2} + \gamma A R_0^{\gamma-1}\sin\varphi\right), 0, -AR_0^{\gamma-1}\cos\varphi\right] \tag{A.10}$$

Magnetic field of Earth:

$$\mathrm{B}_0 = (B_{0r}, B_{0\theta}, B_{0\varphi}) \tag{A.11}$$

The bounce-averaged drift velocity of the guiding center is given as:

$$\langle\mathbf{V}_D\rangle = \frac{\mathbf{E}_0\times\mathbf{B}_0}{B_0^2} \tag{A.12}$$

The cross product of the electric and the magentic field is:

$$\begin{aligned}
\mathbf{E}_0\times\mathbf{B}_0 &= \begin{vmatrix} \hat{r} & \hat{\theta} & \hat{\varphi} \\ E_{0r} & E_{0\theta} & E_{0\varphi} \\ B_{0r} & B_{0\theta} & B_{0\varphi} \end{vmatrix} \\
&= (E_{0\theta}B_{0\varphi} - B_{0\theta}E_{0\varphi})\hat{r} + (E_{0\varphi}B_{0r} - E_{0r}B_{0\varphi})\hat{\theta} + (E_{0r}B_{0\theta} - B_{0r}E_{0\theta})\hat{\varphi} \\
&= -B_{0\theta}E_{0\varphi}\hat{r} + (E_{0\varphi}B_{0r} - E_{0r}B_{0\varphi})\hat{\theta} + E_{0r}B_{0\theta}\hat{\varphi} \qquad \text{(A.13)}
\end{aligned}$$

Then the three velocity components are:

$$\begin{aligned}
\langle V_D\rangle_{\hat{r}} &= -\frac{B_{0\theta}E_{0\varphi}}{B_0^2} = AR_0^{\gamma-1}\cos\varphi\frac{B_{0\theta}}{B_0^2} \qquad \text{(A.14)} \\
\langle V_D\rangle_{\hat{\theta}} &= \frac{E_{0\varphi}B_{0r} - E_{0r}B_{0\varphi}}{B_0^2} \\
&= \frac{1}{B_0^2}\left[-AR_0^{\gamma-1}\cos\varphi B_{0r} + \left(\frac{C}{R_0^2} + \gamma AR_0^{\gamma-1}\sin\varphi\right)B_{0\varphi}\right] \qquad \text{(A.15)} \\
\langle V_D\rangle_{\hat{\varphi}} &= \frac{B_{0\theta}E_{0r}}{B_0^2} = -\left(\frac{C}{R_0^2} + \gamma AR_0^{\gamma-1}\sin\varphi\right)\frac{B_{0\theta}}{B_0^2} \qquad \text{(A.16)}
\end{aligned}$$

The radial drift:

$$\left\langle\frac{dR_0}{dt}\right\rangle = \langle V_D\rangle_{\hat{r}} = AR_0^{\gamma-1}\cos\varphi\frac{B_{0\theta}}{B_0^2} \tag{A.17}$$

The azimuthal drift:

$$\left\langle \frac{d\varphi}{dt} \right\rangle = \frac{\langle V_D \rangle_{\hat{\varphi}} + \langle V_S \rangle_{\hat{\varphi}}}{R_0} = -\left(\frac{C}{R_0^2} + \gamma A R_0^{\gamma-1} \sin\varphi \right) \frac{B_{0\theta}}{B_0^2} \frac{1}{R_0} + \frac{\langle V_S \rangle}{R_0} \tag{A.18}$$

$\langle V_S \rangle_{\hat{\varphi}}$ is the $\hat{\varphi}$ component of the bounce-averaged value:

$$\langle \mathbf{V}_S \rangle = \frac{1}{S_b} \int_{s'}^{s''} V_S \frac{ds}{\sqrt{1 - \dfrac{B(s)}{B_m}}} = \langle \mathbf{V}_B \rangle + \langle \mathbf{V}_R \rangle \tag{A.19}$$

where S_b is given by:

$$S_b = \int_{s'}^{s''} \frac{ds}{\sqrt{1 - \dfrac{B(s)}{B_m}}} \tag{A.20}$$

Here V_S is the magnetic gradient-curvature drift velocity given by Equation (A.7).

APPENDIX B

FREQUENTLY USED ABBREVIATIONS

AMPTE	Active Magnetospheric Particle Tracer Explorers
CAMMICE	Charge and Mass Magnetospheric Ion Composition Measurement
CCE	Charge Composition Explorer
CHEM	Charge-Energy-Mass Spectrometer
CME	Coronal Mass Ejection
CRRES	Combined Release and Radiation Effects Satellite
EMIC	Electromagnetic Ion Cyclotron
ENA	Energetic Neutral Atoms
GEOS	Geodynamic Experimental Ocean Satellite
IMF	Interplanetary Magnetic Field
MICS	Magnetospheric Ion Composition Spectrometer
MLT	Magnetic Local Time
RAM	Ring current-Atmosphere interaction Model
RAM-ND	Ring current-Atmosphere interaction Model with Non-Dipole magnetic field
SAR	Stable Auroral Red
UT	Universal Time

BIBLIOGRAPHY

Aggson, T. L. and Heppner, J. P. [1977], 'Observations of large transient magnetospheric electric elds', *J. Geophys. Res.* **82**, 5155–5164.

Akasofu, S. [1981], 'Energy coupling between the solar wind and the magnetosphere', *Space Sci. Rev.* **28**, 121.

Akasofu, S., Chapman, S. and Venkatesan, D. [1963], 'The main phase of great magnetic storms', *J. Geophys. Res.* **68**, 3345–3350.

Alexeev, I. I., Belenkaya, E. S., Kalegaev, V. V., Feldstein, Y. I. and Grafe, A. [1996], 'Magnetic storms and magnetotail currents', *J. Geophys. Res.* **101**, 7737–7748.

Anderson, B. J., Erlandson, R. E. and Zanetti, L. J. [1992], 'A statistical study of Pc 1-2 magnetic pulsations in the equatorial magnetosphere. I - Equatorial occurrence distributions. II - Wave properties', *J. Geophys. Res.* **97**, 3075–3101.

Anderson, B. J. and Fuselier, S. A. [1994], 'Response of thermal ions to electromagnetic ion cyclotron waves', *J. Geophys. Res.* **99**, 19413.

Angelopoulos, V., Temerin, M., Roth, I., Mozer, F. S., Weimer, D. and Hairston, M. R. [2002], 'Testing global storm-time electric field models using particle spectra on multiple spacecraft', *J. Geophys. Res.* **107**, 21.

Ashour-Abdalla, M., Berchem, J. P., Büchner, J. and Zelenyi, L. M. [1993], 'Shaping of the magnetotail from the mantle: Global and local structuring', *J. Geophys. Res.* **98**, 5651–5676.

Ashour-Abdalla, M., Zelenyi, L. M., Bosqued, J. M. and Kovrazhkin, R. A. [1992], 'Precipitation of fast ion beams from the plasma sheet boundary layer', *Geophys. Res. Lett.* **19**, 617–620.

Balsiger, H., Eberhardt, P., Geiss, J. and Young, D. T. [1980], 'Magnetic storm injection of 0.9- to 16-keV/e solar and terrestrial ions into the high-altitude magnetosphere', *J. Geophys. Res.* **85**, 1645–1662.

Barnet, C. [1990], *Collisions of H, H_2, He and Li atoms and ions with atoms and molecules*, Vol. I, Tech. Rep. ORNL-6086/VI, Oak Ridge Nat. Lab., Oak Ridge, Tenn.

Baumjohann, W. [1993], 'The near-Earth plasma sheet: An AMPTE/ IRM perspective', *Space Sci. Rev.* **64**, 141–163.

Belian, R. D., Gisler, G. R., Cayton, T. and Christensen, R. [1992], 'High-Z energetic particles at geosynchronous orbit during the great solar proton event series of October 1989', *J. Geophys. Res.* **97**, 16897.

Borovsky, J., Thomsen, M., and McComas, D. [1997], 'The superdense plasma sheet: Plasmaspheric origin, solar wind origin, or ionospheric origin?', *J. Geophys. Res.* **102**, 22089.

Büchner, J. and Zeleny, L. M. [1986], 'Deterministic chaos in the dynamics of charged particles near a magnetic field reversal', *Phys. Lett. A* **118**, 395–399.

Büchner, J. and Zelenyi, L. M. [1989], 'Regular and chaotic charged particle motion in magnetotaillike field reversals. I - Basic theory of trapped motion', *J. Geophys. Res.* **94**, 11821–11842.

Burton, R., McPherron, R. and Russell, C. [1975], 'An empirical relationship between interplanetary conditions and Dst', *J. Geophys. Res.* **80**, 4204.

Carovillano, R. L. and Siscoe, G. L. [1973], 'Energy and momentum theorems in magnetospheric processes', *Rev. Geophys.* **11**, 289–353.

Chamberlain, J. [1963], 'Planetary coronae and atmospheric evaporation', *Planet. Space Sci.* **11**, 901–960.

Chen, M., Lyons, L. and Shultz, M. [1994], 'Simulations of phase space distributions of storm time proton ring current', *J. Geophys. Res.* **99**, 5745–5759.

Christon, S., Desai, M., Eastman, T., Gloeckler, G., Kokubun, S., Lui, A., McEntire, R., Roelof, E. and Williams, D. [2000], 'Low-charge-state heavy ions upstream of Earths bow shock and sunward ux of ionosphere O^+, N^+, and O^+ ions: Geotail observations', *Geophys. Res. Lett.* **27**, 2433.

Christon, S., Gloeckler, G., Williams, D., McEntire, R. and Lui, A. T. [1996], 'The downtail distance variation of energetic ions in Earths magnetotail region: Geotail measurements at X > $-208R_E$', *J. Geomagn. Geoelectr.* **48**, 615–627.

Christon, S., Hamilton, D., Gloeckler, G., Eastman, T. and Ipavich, F. [1994], 'High charge state carbon and oxygen ions in Earths equatorial quasi-trapping region', *J. Geophys. Res.* **99**, 13465–13488.

Chung, T. J. [2002], *Computational Fluid Dynamics*, Cambridge University Press.

Cladis, J. and Francis, W. [1992], 'Distribution in magnetotail of O+ ions from cusp/cleft ionosphere: A possible substorm trigger', *J. Geophys. Res.* **97**, 123–130.

Cole, K. [1965], 'Stable auroral red arcs, sinks for energy of Dst main phase', *J. Geophys. Res.* **70**, 1689.

Cornwall, J. [1977], 'On the role of charge exchange in generating unstable waves in the ring current', *J. Geophys. Res.* **82**, 1188–1196.

Cornwall, J., Coroniti, V. and Thorne, R. [1970], 'Turbulent loss of ring current protons', *J. Geophys. Res.* **75**, 4699–4709.

Craven, J., Frank, L. and Ackerson, K. [1982], 'Global observations of a SAR arc', *Geophys. Res. Lett.* **9**, 961.

Daglis, I. [1997], *The role of magnetosphere-ionosphere coupling in magnetic storm dynamics, in Magnetic Storms*, Vol. 98, AGU, Washington, D.C., pp. 107–116.

Daglis, I. A., Thorne, R. M., Baumjohann, W. and Orsini, S. [1999b], 'The terrestrial ring current: Origin, formation, and decay', *Rev. Geophys.* **37**, 407–438.

Daglis, I. and Axford, W. I. [1996], 'Fast ionospheric response to enhanced activity in geospace: Ion feeding of the inner magnetotail', *J. Geophys. Res.* **101**, 5047–5065.

Daglis, I., Axford, W., Livi, S., Wilken, B., Grande, M. and S0raas, F. [1996], 'Auroral ionospheric ion feeding of the inner plasma sheet during substorms', *J. Geomagn. Geoelectr.* **48**, 729–739.

Daglis, I., Kasotakis, G., Sarris, E., Kamide, Y., Livi, S. and Wilken, B. [1999a], 'Variations of the ion composition during an intense magnetic storm and their consequences', *Phys. Chem. Earth* **24**, 229–232.

Daglis, I., Sarris, E. and Wilken, B. [1993], 'AMPTE/CCE CHEM observations of the ion population at geosynchronous altitudes', *Ann. Geophys.* **11**, 685–696.

de Michelis, P., Daglis, I. and Consolini, G. [1997a], 'Average terrestrial ring current derived from AMPTE/CCE-CHEM measurements', *J. Geophys. Res.* **102**, 14103.

de Michelis, P. and Orsini, S. [1997b], 'Energetic neutral atoms propagating toward the Earth: Analysis of the reduction rate due to ionospheric and atmospheric interactions', *J. Geophys. Res.* **102**, 185–194.

Delcourt, D., Moore, T. and Sauvaud, J.-A. [1991], 'Gyro-phase effects near the storm-time boundary of energetic plasma', *Geophys. Res. Lett.* **18**, 1485–1488.

Delcourt, D., Sauvaud, J.-A. and Pedersen, A. [1990], 'Dynamics of single-particle orbits during substorm expansion phase', *J. Geophys. Res.* **95**, 20853–20865.

Dessler, A. and Parker, E. [1959], 'Hydromagnetic theory of geomagnetic storms', *J. Geophys. Res.* **64**, 2239–2252.

Dungey, J. [1961], 'Interplanetary magnetic field and the auroral zones', *Phys. Rev. Lett.* **6**, 47–48.

Ebihara, Y. and Ejiri, M. [1998], 'Modeling of solar wind control of the ring current buildup: a case study of the magnetic storms in April 1997', *Geophys. Res. Lett.* **25**, 3751.

Ejiri, M. [1978], 'Trajectory traces of charged particles in the magnetosphere', *J. Geophys. Res.* **83**(A10), 4798.

Erlandson, R. E. and Ukhorskiy, A. J. [2001], 'Observations of electromagnetic ion cyclotron waves during geomagnetic storms: Wave occurrence and pitch angle scattering', *J. Geophys. Res.* **106**(A3), 3883–3896.

Flannery, B. P., Teukolsky, S. A. and Vetterling, W. T. [1992], *Numerical Recipes in FORTRAN: The Art of Scientific Computing*, Cambridge University Press.

Fok, M.-C., Kozyra, J. U., Nagy, A. F. and Cravens, T. E. [1991], 'Lifetime of ring current particles due to Coulomb collisions in the plasmasphere', *J. Geophys. Res.* **96**, 7861–7867.

Fok, M.-C., Kozyra, J. U., Nagy, A. F., Rasmussen, C. E. and Khazanov, G. V. [1993], 'Decay of equatorial ring current ions and associated aeronomical consequences', *J. Geophys. Res.* **98**, 19381.

Fok, M.-C., Moore, T. and Greenspan, M. [1996], 'Ring current development during storm main phase', *J. Geophys. Res.* **101**, 15311–15322.

Fok, M.-C., Moore, T., Kozyra, J., Ho, G., and Hamilton, D. [1995], 'Three-dimensional ring current decay model', *J. Geophys. Res.* **100**, 9619–9632.

Frank, L. [1970], 'Direct detection of asymmetric increases of extraterrestrial ring current proton intensities in the outer radiation zone', *J. Geophys. Res.* **75**, 1263.

Frank, L. A. [1967], 'On the extraterrestrial ring current during geomagnetic storms', *J. Geophys. Res.* **72**, 3753–3767.

Fu, S., Wilken, B., Zong, Z. and Pu, Z. [2001], 'Ion composition variations in the inner magnetosphere: Individual and collective storm effects in 1991', *J. Geophys. Res.* **106**, 29683.

Ganushkina, N. Y., Pulkkinen, T. I., Milillo, A. and Liemohn, M. [2006], 'Evolution of the proton ring current energy distribution during 21-25 April 2001 storm', *Journal of Geophysical Research (Space Physics)* **111**, 11.

Gloeckler, G. and Hamilton, D. C. [1987], 'AMPTE ion composition results', *Phys. Scr.* **T18**, 73–84.

Gloeckler, G. and Hsieh, K. C. [1979], 'Time-of-flight technique identification at energies from 2 to 400 keV/nucleon', *Nucl. Instr. and Meth.* **165**, 537–544.

Gloeckler, G., Ipavich, F. M., Hamilton, D. C., Lundgren, R. A., Studemann, W., Wilken, B., Kremser, G., Hovestadt, D., Gliem, F. and Rieck, W. [1985], 'The charge-energy-mass spectrometer for 0.3-300 keV/e ions on the AMPTE/CCE', *IEEE Transactions on Geoscience and Remote Sensing* **23**, 234–240.

Gonzalez, W. D., Joselyn, J. A., Kamide, Y., Kroehl, H. W., Rostoker, G., Tsurutani, B. T. and Vasyliunas, V. M. [1994], 'What is a geomagnetic storm?', *J. Geophys. Res.* **99**, 5771–5792.

Gosling, J. T., McComas, D. J., Phillips, J. L., and Bame, S. J. [1991], 'Geomagnetic activity associated with Earth passage of interplanetary shock disturbances and coronal mass ejections', *J. Geophys. Res.* **96**, 7831.

Grafe, A. [1999], 'Are our ideas about Dst correct?', *Ann. Geophys.* **17**, 1–10.

Hamilton, D. C., Gloeckler, G., Ipavich, F., Stüdemann, W., Wilken, B. and Kremser, G. [1988], 'Ring current development during the great geomagnetic storm of February 1986', *J. Geophys. Res.* **93**, 14343–14355.

Henderson, M., Reeves, G., Spence, H., Sheldon, R., Jorgensen, A., Blake, J. and Fennell, J. [1997], 'First energetic neutral atom images from Polar', *Geophys. Res. Lett.* **24**, 1167.

Hesse, M., Smith, M. F., Herrero, F. A., Ghielmetti, A. G., Shelley, E. G., Wurz, P., Bochsler, P. A., Gallagher, D. L., Moore, T. E. and Stephen, T. S. [1993], 'Imaging ion outflow in the high-latitude magnetosphere using low-energy neutral atoms', *Optical Engineering* **32**, 3153–3160.

Hirahara, M., Mukai, T., Terasawa, T., Machida, S., Saito, Y., Yamamoto, T. and Kokubun, S. [1996], 'Cold dense ion flows with multiple components observed in the distant tail lobe by Geotail', *J. Geophys. Res.* **1001**, 7769–7784.

Hodges, R. R. J. [1994], 'Monte Carlo simulation of the terrestrial hydrogen exosphere', *J. Geophys. Res.* **99**, 23229.

Horne, R. and Thorne, R. [1997], 'Wave heating of He^+ by electromagnetic ion-cyclotron waves in the outer magnetosphere: Heating near the $H^+ - He^+$ bi-ion resonance frequency', *J. Geophys. Res.* **102**, 1145711471.

Horwitz, J. [1982], 'The ionosphere as a source for magnetospheric ions', *Rev. Geophys.* **20**, 929–952.

Horwitz, J., Pollock, C., Moore, T., Peterson, W., Burch, J., Winningham, J., Craven, J., Frank, L. and Persoon, A. [1992], 'The polar cap environment of outflowing O^+', *J. Geophys. Res.* **97**, 8361–8379.

Hultqvist, B., Lundin, R., Stasiewicz, K., Block, L., Lundqvist, P.-A., Gustafson, G., Kaskinen, H., Bahnsen, A., Potemra, T. and Zanetti, L. [1988], 'Simultaneous observations of upward moving field-aligned electrons and ions on auroral zone field lines', *J. Geophys. Res.* **93**, 9765–9776.

Jordanova, V. K. [1995], Kinetic Model of the Terrestrial Ring Current, PhD thesis, University of Michigan.

Jordanova, V. K., Boonsiriseth, A., Thorne, R. M. and Dotan, Y. [2003b], 'Ring current asymmetry from global simulations using a high-resolution electric field model', *Journal of Geophysical Research (Space Physics)* **108**, 15.

Jordanova, V. K., Farrugia, C. J., Janoo, L., Quinn, J. M., Torbert, R. B., Ogilvie, K. W., Lepping, R. P., Steinberg, J. T., McComas, D. J. and Belian, R. D. [1998], 'October 1995 magnetic cloud and accompanying storm activity: Ring current evolution', *J. Geophys. Res.* **103**(A1), 79–92.

Jordanova, V. K., Farrugia, C. J., Thorne, R. M., Khazanov, G. V., Reeves, G. D. and Thomsen, M. F. [2001a], 'Modeling ring current proton precipitation by electromagnetic ion cyclotron waves the May 14-16, 1997, storm', *J. Geophys. Res.* **106**(A1), 7–22.

Jordanova, V. K., Kistler, L. M., Farrugia, C. J. and Torbert, R. B. [2001c], 'Effects of inner magnetospheric convection on ring current dynamics: March 10-12, 1998', *J. Geophys. Res.* **106**, 29705–29720.

Jordanova, V. K., Kistler, L. M., Kozyra, J. U., Khazanov, G. V. and Nagy, A. F. [1996a], 'Collisional losses of ring current ions', *J. Geophys. Res.* **101**, 111–126.

Jordanova, V. K., Kistler, L. M., Thomsen, M. F. and Mouikis, C. G. [2003a], 'Effects of plasma sheet variability on the fast initial ring current decay', *Geophys. Res. Lett.* **30**, 44–1.

Jordanova, V. K., Kozyra, J., Khazanov, V., Nagy, A., Ramussen, C. and Fok, M. C. [1994], 'A bounce-averaged kinetic model of the ring current ion population', *Geophys. Res. Lett.* **21**, 2785–2788.

Jordanova, V. K., Kozyra, J. U. and Nagy, A. F. [1996b], 'Effects on heavy ions on the quasi-linear diffusion coefficients from resonant interactions with electromagnetic ion cyclotron waves', *J. Geophys. Res.* **101**(A9), 19771–19778.

Jordanova, V. K., Kozyra, J. U., Nagy, A. F. and Khazanov, G. V. [1997], 'Kinetic model of the ring current-atmosphere interactions', *J. Geophys. Res.* **102**, 14279–14292.

Jordanova, V. K. and Miyoshi, Y. [2005], 'Relativistic model of ring current and radiation belt ions and electrons: Initial results', *Geophys. Res. Lett.* **32**, 14104.

Jordanova, V. K., Miyoshi, Y. S., Zaharia, S., Thomsen, M. F., Reeves, G. D., Evans, D. S., Mouikis, C. G. and Fennell, J. F. [2006], 'Kinetic simulations of ring current evolution during the Geospace Environment Modeling challenge events', *J. Geophys. Res.* **111**, 11.

Jordanova, V. K., Thorne, R. M., Farrugia, C. J., Dotan, Y., Fennell, J. F., Thomsen, M. F., Reeves, G. D. and McComas, D. J. [2001b], 'Ring Current Dynamics during the 13-18 July 2000 Storm Period', *Sol. Phys.* **204**, 361–375.

Jordanova, V. K., Torbert, R. B., Thorne, R. M., Collin, H. L., Roeder, J. L. and Foster, J. C. [1999], 'Ring current activity during the early Bz¡0 phase of the January 1997 magnetic cloud', *J. Geophys. Res.* **104**, 24895.

Jorgensen, A., Henderson, M., Roelof, E., Reeves, G. and Spence, H. [2001], 'Charge exchange contribution to the decay of the ring current, measured by energetic neutral atoms (ENAs)', *J. Geophys. Res.* **106**, 1931.

Kamide, Y. [1992], 'Is substorm occurrence a necessary condition for a magnetic storm?', *J. Geomagn. Geoelectr.* **44**, 109–117.

Kamide, Y., Baumjohann, W., Daglis, I. A., Gonzalez, W. D., Grande, M., Joselyn, J. A., McPherron, R. L., Phillips, J. L., Reeves, E. G. D., Rostoker, G., Sharma, A. S., Singer, H. J., Tsurutani, B. T. and Vasyliunas, V. M. [1998b], 'Current understanding of magnetic storms: Storm-substorm relationships', *J. Geophys. Res.* **103**, 17705–17728.

Kamide, Y., Yokoyama, N., Gonzalez, W., Tsurutani, B., Daglis, I., Brekke, A. and Masuda, S. [1998a], 'Two-step development of geomagnetic storms', *J. Geophys. Res.* **103**, 6917–6921.

Kaufmann, R. [1987], 'Substorm currents: Growth phase and onset', *J. Geophys. Res.* **92**, 7471–7486.

Kaye, S., Johnson, R., Sharp, R. and Shelley, E. [1981], 'Observations of transient H1 and O1 bursts in the equatorial magnetosphere', *J. Geophys. Res.* **86**, 1335–1344.

Kintner, P., Vago, J., Chesney, S., Arnoldy, R., Lynch, K., Pollock, C. and Moore, T. [1992], 'Localized lower hybrid acceleration of ionospheric plasma', *Phys. Rev. Lett.* **68**, 2448–2451.

Kistler, L. M., Ipavich, F. M., Hamilton, D. C., Gloeckler, G., Wilken, B., Kremser, G. and Stüdemann, W. [1989], 'Energy spectra of the major ion species in the ring current during geomagnetic storms', *J. Geophys. Res.* **94**, 3579–3599.

Kistler, L. M. and Larson, D. J. [2000], 'Testing electric and magnetic field models of the storm-time inner magnetosphere', *J. Geophys. Res.* **105**, 25221–25232.

Kistler, L. M., Möbius, E., Klecker, B., Gloeckler, G., Ipavich, F. and Hamilton, D. [1990], 'Spatial variations in the suprathremal ion distribution during substorms in the plasma sheet', *J. Geophys. Res.* **95**, 18871–18885.

Kozlovsky, A. and Lyatsky, W. [1999], 'Finite Larmor radius convection instability in the near-Earth plasma sheet', *J. Geophys. Res.* **104**, 2443–2450.

Kozyra, J., Cravens, T., Nagy, A., Fontheim, E. and Ong, R. [1984], 'Effects of energetic heavy ions on electromagnetic ion cyclotron wave generation in the plasmapause region', *J. Geophys. Res.* **89**, 2217–2233.

Kozyra, J., Liemohn, M., Clauer, C., Ridley, A., Thomsen, M., Borovsky, J., Roeder, J. and Jordanova, V. [2002], 'Two-step Dst development and ring current composition changes during the 46 June 1991 magnetic storm', *J. Geophys. Res.* **107**, 1224.

Kozyra, J., Nagy, A. and Slater, D. [1997], 'The high altitude energy source for stable auroral red (SAR) arcs', *Rev. Geophys.* **35**, 155.

Kozyra, J., Shelley, E., Comfort, R., Brace, L., Cravens, T. and Nagy, A. [1987], 'The role of ring current O^+ in the formation of Stable Auroral Red Arcs', *J. Geophys. Res.* **92**, 7487.

Kozyra, J. U., Borovsky, J. E., Chen, M. W., Fok, M.-C. and Jordanova, V. K. [1998], Plasma Sheet Preconditioning, Enhanced Convection and Ring Current Development, *in* S. Kokubun and Y. Kamide, eds, 'ASSL Vol. 238: Substorms-4', p. 755.

Krimigis, S., Gloeckler, G., McEntire, R., Potemra, T., Scarf, F. and Shelley, E. G. [1985], 'Magnetic storm of September 4, 1984: A synthesis of ring current spectra and energy densities measured with AMPTE/CCE', *Geophys. Res. Lett.* **12**, 329–332.

Lanzerotti, L. [2003], NATO Advanced Research Workshop (ESPRIT).
URL: *http://sat2.space.noa.gr/~daglis/sessions.html*

Li, W., Raeder, J., Dorelli, J., Øieroset, M. and Phan, T. D. [2005], 'Plasma sheet formation during long period of northward IMF', *Geophys. Res. Lett.* **32**, 12.

Liemohn, M., Kozyra, J., Jordanova, V., Khazanov, G., Thomsen, M. and Cayton, T. [1999], 'Analysis of early phase ring current recovery mechanisms during geomagnetic storms', *Geophys. Res. Lett.* **25**, 2845.

Liemohn, M., Kozyra, J., Richards, P., Khazanov, G., Buonsanto, M. and Jordanova, V. [2000], 'Ring current heating of the thermal electrons at solar maximum', *J. Geophys. Res.* **105**, 27767.

Liemohn, M., Kozyra, J., Thomsen, M., Roeder, J., Lu, G., Borovsky, J. and Cayton, T. [2001a], 'Dominant role of the asymmetric ring current in producing the stormtime Dst', *J. Geophys. Res.* **106**, 10883.

Liemohn, M. W. [2003], 'Yet another caveat to using the Dessler-Parker-Sckopke relation', *Journal of Geophysical Research (Space Physics)* **108**, 18.

Liu, S., Chen, M. W., Roeder, J. L., Lyons, L. R. and Schulz, M. [2005], 'Relative contribution of electrons to the stormtime total ring current energy content', *Geophys. Res. Lett.* **32**, 3110.

Lu, G., Reiff, P., Moore, T. and Heelis, R. [1992], 'Upflowing ionospheric ions in the auroral region', *J. Geophys. Res.* **97**, 16855–16863.

Lui, A. and Hamilton, D. [1992], 'Radial profiles of quiet time magnetospheric parameters', *J. Geophys. Res.* **97**, 19325–19332.

Lui, A., McEntire, R. and Krimigis, S. [1987], 'Evolution of the ring current during two geomagnetic storms', *J. Geophys. Res.* **92**, 7459–7470.

Lui, A., Williams, D., Roelof, E., McEntire, R. and Mitchell, D. [1996], 'First composition measurements of energetic neutral atoms', *Geophys. Res. Lett.* **23**, 2641–2644.

Lundin, R. and Eliasson, L. [1991], 'Auroral energization processes', *Ann. Geophys.* **9**, 202–223.

Lundin, R., Eliasson, L., Haerendel, G., Boehm, M. and Holback, B. [1994], 'Large-scale auroral plasma density cavities observed by Freja', *Geophys. Res. Lett.* **21**, 1903–1906.

Lyons, L. R. [1973], 'Comments on pitch angle diffusion in the radiation belts', *J. Geophys. Res.* **78**, 6793.

Lyons, L. R. [1976], Explorer 45 observations of the proton ring current, *in* 'Magnetospheric Particles and Fields', pp. 137–148.

Lyons, L. R. and Williams, D. J. [1975], 'The storm and poststorm evolution of energetic /35-560 keV/ radiation belt electron distributions', *J. Geophys. Res.* **80**, 3985–3994.

Lyons, L. R. and Williams, D. J. [1976], 'Storm-associated variations of equatorially mirroring ring current protons, 1-800 keV, at constant first adiabatic invariant', *J. Geophys. Res.* **81**, 216–220.

Lyons, L. and Thorne, R. M. [1972], 'Parasitic pitch angle diffusion of radiation belt particles by ion cyclotron waves', *J. Geophys. Res.* **77**, 5608–5616.

Maynard, N. C. and Chen, A. J. [1975], 'Isolated cold plasma regions - Observations and their relation to possible production mechanisms', *J. Geophys. Res.* **80**, 1009–1013.

McComas, D. J., Bame, S. J., Barker, P., Feldman, W. C., Phillips, J. L., Riley, P. and Griffee, J. W. [1998], 'Solar Wind Electron Proton Alpha Monitor (SWEPAM) for the Advanced Composition Explorer', *Space Sci. Rev.* **86**, 563–612.

McComas, D. J., Bame, S. J., Barraclough, B. L., Donart, J. R., Elphic, R. C., Gosling, J. T., Moldwin, M. B., Moore, K. R. and Thomsen, M. F. [1993], 'Magnetospheric plasma analyzer - Initial three-spacecraft observations from geosynchronous orbit', *J. Geophys. Res.* **98**, 13453.

McIlwain, C. E. [1966], 'Magnetic Coordinates', *Space Sci. Rev.* **5**, 585–598.

McPherron, R. [1972], 'Substorm related changes in the geomagnetic tail: The growth phase', *Planet. Space Sci.* **20**, 1521–1539.

Milillo, A., Orsini, S., Massetti, S. and Mura, A. [2006], 'Geomagnetic activity dependence of the inner magnetospheric proton distribution: An empirical approach for the 21-25 April 2001 storm', *J. Geophys. Res.* **111**, 11.

Mitchell, D., Hsieh, K., Curtis, C., Hamilton, D., Voss, H., Roelof, E. and Brandt, P. C. [2001], 'Imaging two geomagnetic storms in energetic neutral atoms', *Geophys. Res. Lett.* **28**, 1151.

Möbius, E., Scholer, M., Klecker, B., Hovestadt, D. and Gloeckler, G. [1987], *Acceleration of ions of ionospheric origin in the plasma sheet during substorm activity*, Magnetotail Physics, pp. 231–234.

Moore, T. [1984], 'Superthermal ionospheric outflows', *Rev. Geophys.* **22**, 264–274.

Moore, T., Arnoldy, R., Feynman, J. and Hardy, D. [1981], 'Propagating substorm injection fronts', *J. Geophys. Res.* **86**, 6713–6726.

Moore, T. and Delcourt, D. [1995], 'The geopause', *Rev. Geophys.* **33**, 175.

Murphy, C. H., Wang, C. S. and Kim, J. S. [1975], 'Inductive electric field of a time-dependent ring current', *Planet. Space Sci.* **23**, 1205–1209.

Nishida, A. [1994], 'The GEOTAIL mission', *Geophys. Res. Lett.* **21**, 2871–2873.

Noël, S. [1997], 'A Monte Carlo model of the ring current decay', *Adv. Space Res.* **20**(3), 335–338.

Nose, M., Ohtani, S., Takahashi, K., Lui, A., McEntire, R., Williams, D., Christon, S. and Yumoto, K. [2001], 'Ion composition of the near-Earth plasma sheet in storm and quiet intervals: Geotail/EPIC measurements', *J. Geophys. Res.* **106**, 8391.

Ohtani, S., Nosé, M., Rostoker, G., Singer, H., Lui, A. T. Y. and Nakamura, M. [2001], 'Storm-substorm relationship: Contribution of the tail current to Dst', *J. Geophys. Res.* **106**, 21199–21210.

Øieroset, M., Phan, T. D., Lin, R. P. and Sonnerup, B. U. Ö. [2000], 'Walén and variance analyses of high-speed flows observed by Wind in the midtail plasma sheet: Evidence for reconnection', *J. Geophys. Res.* **105**, 25247–25264.

Orsini, S., Daglis, I., Candidi, M., Hsieh, K., Livi, S. and Wilken, B. [1994], 'Model calculation of energetic neutral atoms precipitation at low altitudes', *J. Geophys. Res.* **99**, 13489–13498.

Østgaard, N., Mende, S. B., Frey, H. U., Gladstone, G. R. and Lauche, H. [2003], 'Neutral hydrogen density profiles derived from geocoronal imaging', *J. Geophys. Res.* **108**(A7), 18–1.

OBrien, T. and McPherron, R. [2000], 'An empirical phase space analysis of ring current dynamics: solar wind control of injection and decay', *J. Geophys. Res.* **105**, 7707.

Parker, E. [1957], 'Newtonian development of the dynamical properties of the ionised gases at low density', *Phys. Rev.* **107**, 924–933.

Parks, G. K. [2004], *Physics of space plasmas : an introduction*, Physics of space plasmas : an introduction / George K Parks. Boulder, Colo. : Westview Press, Advanced Book Program, c2004.

Peterson, W., Shelley, E., Boardsen, S., Gurnett, D., Ledley, B. G., Sugiura, M., Moore, T. and Waite, J. [1988], 'Transverse ion energization and low-frequency plasma waves in the mid-altitude auroral zone: A case study', *J. Geophys. Res.* **93**, 11405–11428.

Phaneuf, R., Janev, R. and Pindzola, M. [1987], *Collisions of carbon and oxygen ions with electrons, H, H_2 and He*, Vol. V, Tech. Rep. ORNL-6090/V5, Oak Ridge Nat. Lab., Oak Ridge, Tenn.

Pilipp, W. and Morfill, G. [1978], 'The formation of the plasma sheet resulting from plasma mantle dynamics', *J. Geophys. Res.* **83**, 5670–5678.

Pollock, C., Asamura, K., Balkey, M., Burch, J., Funsten, H., Grande, M., Gruntman, M., Jahn, J.-M., Lampton, M., Liemohn, M., McComas, D., Mukai, T., Ritzau, S., Schattenburg, M., E.Scime, Skoug, R., Valek, P. and West, M. [2001], 'Initial Medium Energy Neutral Atom (MENA) images of Earths magnetosphere during substorms and storm-time', *Geophys. Res. Lett.* **28**, 1147.

Posner, A., Schwadron, N., Zurbuchen, T., Kozyra, J., Liemohn, M. and Gloeckler, G. [2002], 'Association of low-charge-state heavy ions far upstream of the Earths bow shock with space weather', *Geophys. Res. Lett.* **29**(7), 1099.

Rairden, R. L., Frank, L. A. and Craven, J. D. [1986], 'Geocoronal imaging with Dynamics Explorer', *J. Geophys. Res.* **91**, 13613.

Rees, M. and Roble, R. [1975], 'Observations and theory of the formation of stable auroral red arcs', *J. Geophys. Res.* **13**, 201.

Reeves, G. and Spence, H. [2001], 'Charge exchange contribution to the decay of the ring current measured by energetic neutral atoms (ENAs)', *J. Geophys. Res.* **106**, 1931.

Reiff, P., Spiro, R., and Hill, T. [1981], 'Dependence of polar cap potential drop of interplanetary parameters', *J. Geophys. Res.* **86**, 7639.

Ridley, A. J. and Liemohn, M. W. [2002], 'A model-derived storm time asymmetric ring current driven electric field description', *J. Geophys. Res.* **107**, 2.

Roederer, J. [1970], *Dynamics of Geomagnetically Trapped Particles*, Heidelberg-New York.

Roelof, E. [1987], 'Energetic neutral atom image of storm-time ring current', *Geophys. Res. Lett.* **14**, 652.

Rossi, B. and Olbert, S. [1970], *Introduction to the physics of space.*, New York: McGraw-Hill.

Schulz, M. and Blake, J. [1990], 'Analytical estimates for gyration-, bounce, and drift-averaged atmospheric densities experienced by Geomagnetically trapped particles', *EOS Trans. AGU* **71**, 1556.

Sckopke, N. [1966], 'A general relation between the energy of trapped particles and the disturbance field over the Earth', *J. Geophys. Res.* **71**, 3125–3130.

Shapiro, V., Soloviev, G. and Bingham, J. D. R. [1995], 'Lower hybrid dissipative cavitons and ion heating in the auroral ionosphere', *Phys. Plasmas* **2**, 516–526.

Sheldon, R. and Hamilton, D. [1993], 'Ion transport and loss in the Earths quiet ring current, 1, Data and standard model', *J. Geophys. Res.* **98**, 13491–13508.

Shelley, E., Johnson, R. and Sharp, R. [1972], 'Satellite observations of energetic heavy ions during a geomagnetic storm', *J. Geophys. Res.* **77**, 6104–6110.

Shukhtina, M. A. [1993], 'On the calculation of the magnetic drift velocity of particles with arbitrary pitch angles', *Planet. Space Sci.* **41**(4), 327–331.

Smith, P. and Bewtra, N. [1978], 'Charge exchange lifetimes for ring current ions', *Space Sci. Rev.* **22**, 301–318.

Smith, P., Bewtra, N. and Hoffman, R. [1981], 'Inference of the ring current ion composition by means of charge exchange decay', *J. Geophys. Res.* **86**, 3470–3480.

Smith, S. W., L'Heureux, J., Ness, N. F., Acuña, M. H., Burlaga, L. F. and Scheifele, J. [1998], 'The ACE Magnetic Fields Experiment', *Space Sci. Rev.* **86**, 613.

Speiser, T. [1965a], 'Particle trajectories in a model current sheet, based on the open model of the magnetosphere, with applications to auroral particles', *J. Geophys. Res.* **70**, 1717–1728.

Speiser, T. [1965b], 'Particle trajectories in model current sheets, 1, Analytical solutions', *J. Geophys. Res.* **70**, 4219–4226.

Speiser, T. W. [1965], 'Particle Trajectories in Model Current Sheets, 1, Analytical Solutions', *J. Geophys. Res.* **70**, 4219.

Spjeldvik, W. and Fritz, T. [1978], 'Theory of charge states of energetic oxygen ions in the Earths radiation belts', *J. Geophys. Res.* **83**, 1583–1594.

Stern, D. [1975], 'The motion of a proton in the equatorial magnetosphere', *J. Geophys. Res.* **80**, 595.

Strang, G. [1968], 'On the construction and comparison of difference schemes', *SIAM J. Num. Anal.* **5**(3), 506–517.

Strangeway, R. J., Ergun, R. E., Su, Y.-J., Carlson, C. W. and Elphic, R. C. [2005], 'Factors controlling ionospheric outflows as observed at intermediate altitudes', *J. Geophys. Res.* **110**, 3221.

Strangeway, R. and Johnson, R. [1983], 'Mass composition of substorm-related energetic ion dispersion events', *J. Geophys. Res.* **88**, 2057–2064.

Stuart, G. [1959], 'Satellite-measured radiation', *Phys. Rev. Lett.* **2**, 417–418.

Takahashi, S., Iyemori, T. and Takeda, M. [1990], 'A simulation of the storm-time ring current', *Planet. Space Sci.* **38**, 1133.

Terasawa, T., Fujimoto, M., Mukai, T., Shinohara, I., Saito, Y., Yamamoto, T., Machida, S., Kokubun, S., Lazarus, A. J., Steinberg, J. T. and Lepping, R. P. [1997], 'Solar wind control of density and temperature in the near-Earth plasma sheet: Wind/Geotail collaboration', *Geophys. Res. Lett.* **24**, 935–938.

Thelin, B., Aparicio, B. and Lundin, R. [1990], 'Observations of upflowing ionospheric ions in the mid-altitude cusp/cleft region with the Viking satellite', *J. Geophys. Res.* **95**, 5931–5939.

Thomsen, M., Borovsky, J., McComas, D. and Collier, M. [1998], 'Variability of the ring current source population', *Geophys. Res. Lett.* **25**, 3481.

Thorne, R. and Horne, R. [1994], 'Energy transfer between energetic ring current H^+ and O^+ by electromagnetic ion cyclotron waves', *J. Geophys. Res.* **99**, 1727517282.

Thorne, R. and Horne, R. [1997], 'Modulation of electromagnetic ion cyclotron instability due to interaction with ring current O^+ during magnetic storms', *J. Geophys. Res.* **102**, 14155–14163.

Tinsley, B. and Akasofu, S. [1982], 'A note on the lifetime of the ring current particles', *Planet. Space Sci.* **30**, 733–740.

Tsyganenko, N. A. [2002a], 'A model of the near magnetosphere with a dawn-dusk asymmetry 1. Mathematical structure', *J. Geophys. Res.* **107**(A8), 12–1.

Tsyganenko, N. A. [2002b], 'A model of the near magnetosphere with a dawn-dusk asymmetry 2. Parameterization and fitting to observations', *J. Geophys. Res.* **107**(A8), 10–1.

Tsyganenko, N. A., Singer, H. J. and Kasper, J. C. [2003], 'Storm-time distortion of the inner magnetosphere: How severe can it get?', *J. Geophys. Res.* **108**(A5), 18–1.

Tsyganenko, N. A. and Sitnov, M. I. [2005], 'Modeling the dynamics of the inner magnetosphere during strong geomagnetic storms', *J. Geophys. Res.* **110**(A9), 3208.

Vapirev, A. E. and Jordanova, V. K. [2007], 'Calculation of bounce-averaged velocities and hydrogen densities for a storm-time magnetic field', *Geophys. Res. Lett.* **34**, L10103.

Volland, H. [1973], 'A semiempirical model for large-scale magnetospheric electric fields', *J. Geophys. Res.* **78**, 171.

Wahlund, J.-E., Opgenoorth, H., Häggström, I., Winser, K. and Jones, G. [1992], 'EISCAT observations of topside ionospheric ion outflows during auroral activity: Revisited', *J. Geophys. Res.* **97**, 3019–3037.

Wentworth, R. [1963], 'Pitch angle diffusion in a magnetic mirror geometry', *Phys. Fluids* **6**, 431.

Wilken, B., Weiss, W., Hall, D., Grande, M., SØraas, F. and Fennell, J. [1992], 'Magnetospheric Ion Composition Spectrometer onboard the CRRES spacecraft', *J. Spacecr. Rockets* **29**, 585–591.

Williams, D. [1983], 'The Earths ring current: Causes, generation, and decay', *Space Sci. Rev.* **34**, 223–234.

Williams, D. [1987], 'Ring current and radiation belts', *Rev. Geophys.* **25**, 570–578.

Wygant, J., Rowland, D., Singer, H. J., Temerin, M., Mozer, F. and Hudson, M. K. [1998], 'Experimental evidence on the role of the large spatial scale electric field in creating the ring current', *J. Geophys. Res.* **103**, 29527–29544.

Yanenko, N. [1971], *The method of fractional steps: The solution of problems of mathematical physics in several variables*, Springer-Verlag, New York.

Yau, A., Shelley, E., Peterson, W. and Lenchyshyn, L. [1985], 'Energetic auroral and polar ion outflow at DE-1 altitudes: Magnitude, composition, magnetic activity dependence, and long-term variations', *J. Geophys. Res.* **90**, 84178432.

Yeh, H.-C. and Foster, J. [1990], 'Storm time ion outflow at midlatitude', *J. Geophys. Res.* **95**, 7881–7891.

Young, D., Balsiger, H., and Geiss, J. [1982], 'Correlations of magnetospheric ion composition with geomagnetic and solar activity', *J. Geophys. Res.* **87**, 9077.